Downloaded from orbit.dtu.dk on: Dec 20, 2017

Technical University of Denmark

On quantum amplifiers, quantum discrimination and adaptive phase estimation

Usuga Castaneda, Mario A.; Andersen, Ulrik Lund

Publication date:
2012

Document Version
Publisher's PDF, also known as Version of record

Link back to DTU Orbit

Citation (APA):
Castaneda, M. A. U., & Andersen, U. L. (2012). On quantum amplifiers, quantum discrimination and adaptive phase estimation.

DTU Library
Technical Information Center of Denmark

General rights
Copyright and moral rights for the publications made accessible in the public portal are retained by the authors and/or other copyright owners and it is a condition of accessing publications that users recognise and abide by the legal requirements associated with these rights.

- Users may download and print one copy of any publication from the public portal for the purpose of private study or research.
- You may not further distribute the material or use it for any profit-making activity or commercial gain
- You may freely distribute the URL identifying the publication in the public portal

If you believe that this document breaches copyright please contact us providing details, and we will remove access to the work immediately and investigate your claim.

On quantum amplifiers, quantum discrimination and adaptive phase estimation

Mario A. Usuga
Physics Department
Technical University of Denmark

A thesis submitted for the degree of
Doctor of Philosophy

February 2012

To Angela, Diana, Cristina, Mom and Dad
for their understanding and continuous support.

Acknowledgements

I want to thank the members of the QIV group at the Max Planck institute who made me feel welcome during my stay in Erlangen and specially to Professor Gerd Leuchs for allowing this fruitful experience to happen. Likewise, I thank the members of QUIN group at DTU who have accompanied me during the last 2 years.

I am specially grateful to my supervisor Ulrik L. Andersen for the freedom that he gave me in pursuing my research but also for his advice that kept me in the right track, and for his disposition and interest.

I also would like to thank my closest collaborators, Christian Mueller, Mikael Lassen, Lars Madsen, Bo Melholt Nielsen, Christoffer Wittmann, Christoph Marquardt, Radim Filip and Petr Marek.

During this time, I enjoyed and appreciated discussions about physics (and/or life in general) with Mikael Lassen, Alex Huck, Metin Sabuncu, Josef Fuerst, Jonas Schou Neergaard-Nielsen, Amine Laghaout, Ulrich Busk Hoff, Niels Israelsen Kristiansen, Mathieu Manceau, Adriano Berni and Miroslav Jezek (among others). And specially the long discussions during and after the experiments I had with Christian Mueller who had a remarkable participation in two of the experiments here presented.

I finally want to thank my family and friends who always supported me and made this walk easier to follow.

Contents

List of Figures

List of Tables

List of Symbols and Notation

$\hat{A}$	Operator corresponding to the quantity A
$\hat{A}^\dagger$	Hermitian conjugate of the operator $\hat{A}$
$\langle\hat{A}\rangle$	Expectation value for operator $\hat{A}$
$\Delta\hat{A}$	Uncertainty in operator $\hat{A}$
$\Delta^2\hat{A}$	Variance of operator $\hat{A}$
$\tilde{A}$	Estimate of quantity A
V^H	Holevo variance
$\hat{a}$	Field annihilation operator
$\hat{a}^\dagger$	Field creation operator
$\hat{\rho}$	Density Operator
$\hat{n}$	Number operator
$\hat{\mathbb{F}}$	Noise operator
$\hat{F}(\theta)$	Phase POVM
$\hat{S}(r)$	Squeezing operator
$\hat{D}(\alpha)$	Displacement operator
$\hat{X}$	Quadrature operator
$\hat{P}$	Quadrature operator
$\hat{X}_\theta$	In-phase Quadrature operator
$\hat{X}_{\theta+\pi/2}$	Out-of-phase Quadrature operator
$\mathbf{I}_{[0,t)}$	Photocurrent record up to time t
$\Phi_{[0,t)}$	Local oscillator phase up to time t
i	Photocurrent
η	Quantum Efficiency
N_{th}	Mean number of thermal photons
α	Coherent state complex amplitude
r	Squeezing parameter
$\mathcal{P}$	Probability, probability distribution
$\hat{\Pi}_n^K(\alpha)$	POVM element in Kennedy receiver $n = \{0, 1\}$

$\hat{\Pi}_n^{OD}(\beta)$	POVM element in Optimal Displacement receiver $n = \{0, 1\}$
P_{succ}^{Kn}	Success probability in Kennedy receiver for staten, $n = \{0, 1\}$

List of Abbreviations

ABS	Asymmetric Beam Splitter
AC	Alternating Current
ADC	Analog to Digital Converter
APD	Avalanche Photo diode
AM	Amplitude Modulation
BCH	Baker-Campbell-Hausdorff
BS	Beam Splitter
BPF	Band Pass Filter
BPSK	Binary Phase-Shift Key
BW	BandWidth
CV	Continuous Variable
CW	Continuous Wave
DAC	Digital to Analog Converter
DC	Direct Current
DSP	Digital Signal Processing
EOM	Electro Optical Modulator
FPGA	Field Programmable Gate Array
HD	Homodyne Detection
HPF	High Pass Filter
HVA	High voltage amplifier
HWP	Half Wave Plate
LO	Local Oscillator
LPF	Low Pass Filter
MSPS	Megasamples per second
PBS	Polarizing Beam Splitter
PDH	Pound-Drever-Hall
PID	Proportional Integral Derivative
PLL	Phase Locked Loop

PM	Phase Modulation
PNRD	Photon Number Resolving Detector
POVM	Positive Operator Valued Measure
PZT	Piezoelectric Transducer
QNL	Quantum Noise Limit
QPSK	Quadrature Phase-Shift Key
QSD	Quantum State Discrimination
QWP	Quarter Wave Plate
RBW	Resolution Bandwidth
RF	Radio Frequency
SA	Spectrum Analizer
SDE	Stochastic Differential Equation
SME	Stochastic Master Equation
SNR	Signal to Noise Ratio
SSE	Stochastic Schroedinger Equation
VBW	Video Bandwidth
VHDL	VHSIC Hardware Description Language
VHSIC	Very-High-Speed Integrated Circuits.
WGM	Wave Guide Modulator

Chapter 1

Introduction

1.1 Overview

This thesis presents the work done during a one year research visit to the Max Planck institute for the science of light in Erlangen, Germany led by Professor Gerd Leuchs and in the Quantum information group (QUIN) at the Physics department in the Technical University of Denmark (DTU) in Lyngby, Denmark under the supervision of Professor Ulrik L. Andersen.
The results presented belong to the fields of Quantum communication, Quantum metrology and Quantum Information.
The thesis is divided in self contained chapters that give a detailed description of the theory and experimental realizations. Extensive theory is given with the intention of giving the context, present the state of art and facilitate the presentation and interpretation of results.

1.2 Thesis structure

The thesis is divided as follows:

Chapter 2: It is devoted to a review of the main concepts in the **theory of quantum optics**. It defines among other things, phase space components (field quadratures, Wigner functions, etc), Gaussian states, generalized preparation of quantum states through the density operator and generalized measurement using POVMs.

Chapter 3: Discusses the subject of **Quantum amplifiers**. It gives arguments to show why perfect amplification is prohibited by quantum mechanics, and presents mainly two classes of amplifiers: phase insensitive linear amplifier (deterministic) and

probabilistic amplifier. A new proposal to achieve noiseless quantum amplification is presented and the experimental results are given.

Chapter 4 Gives an excursion trough the classical and quantum characteristics of phase and its impact in metrology. Evidences the problems in defining a phase observable, and discusses the difference between measurement and estimation. Avances in the experimental realization of **adaptive phase estimation** are presented.

Chapter 5 Quantum state discrimination. The notion of quantum hypothesis testing and basic binary receivers are given and used later to explain a new type of receiver that doubles the data rate with respect to binary receivers rate and lowers the error probability compared to standard by using a QPSK alphabet.

Chapter 2

Basic Quantum Optics

Contents

This chapter presents a review of the basic ingredients of the theory of quantum optics that are used in the subsequent chapters. We will mainly focus on the phase space picture in quantum optics which gives a simple description of quantum states and due to its importance, is recurrently used throughout this thesis. This phase space description requires the definition of quadrature operators and Wigner functions which have an experimental counterpart that we can access through a measurement technique called homodyne detection. We later present the family of Gaussian states which plays a major role in the continuous variable quantum information, and show their most relevant features. Another useful representation of quantum states is the density matrix, that gives us the most general type of quantum states and enables a quick calculation of statistical information. We also describe quantum measurements in their most general form, which is in the formalism of positive operator-valued measures (POVM). We finally define the phase probability distribution and Holevo variance.

2.1 EM Quantization

In analogy to the classical description of light [69], a quantized electric field operator can be defined as [68]:

$$\hat{E}(r,t) = i\sum_k \left(\frac{\hbar\omega_k}{2\epsilon_0 V}\right)^{1/2} \left[\hat{a}_k \mathbf{u}_k(r) e^{-i\omega_k t} + h.c.\right] \tag{2.1}$$

where the annihilation $\hat{a}_k$ and creation operators $\hat{a}_k^\dagger$ are related to the classical (complex) amplitudes α and α^* respectively. Expression (2.1) represents the quantized electric field, composed of different modes (labeled by k) each of which has a different frequency ω_k and spatial mode[1] $\mathbf{u}_k(r)$. Quantization of the electromagnetic field is accomplished by choosing $\hat{a}_k$ and $\hat{a}_k^\dagger$ to be mutually adjoint operators. Since photons are bosons, the appropriate commutation relations for these operators are:

$$[\hat{a}_k, \hat{a}_{k'}] = [\hat{a}_k^\dagger, \hat{a}_{k'}^\dagger] = 0, \quad [\hat{a}_k, \hat{a}_{k'}^\dagger] = \delta_{kk'} \tag{2.2}$$

Within the scope of this thesis, it will be sufficient to consider only a single mode of the field. We can therefore drop the index k and rewrite the electric field as[2]

$$\hat{E}(r,t) = i\left(\frac{\hbar\omega}{2\epsilon_0 V}\right)^{1/2} \mathbf{u}(r)\left(\hat{a}e^{-i\omega t} + \hat{a}^\dagger e^{i\omega t}\right). \tag{2.3}$$

2.1.1 Heisenberg uncertainty

The Heisenberg uncertainty principle states that if any two observables $\hat{A}$, $\hat{B}$ satisfy[3]

$$\left[\hat{A}, \hat{B}\right] = \hat{C}, \tag{2.4}$$

then the product of its uncertainties is bounded:

$$\Delta\hat{A}\Delta\hat{B} \geq \frac{1}{2}|\langle\hat{C}\rangle| \tag{2.5}$$

and we use the following definition for the uncertainty of an operator $\hat{O}$:

$$\Delta\hat{O} = \sqrt{\langle\hat{O}^2\rangle - \langle\hat{O}\rangle^2} \tag{2.6}$$

In short, the Heisenberg uncertainty principle implies that whenever we find a commutator of the form (2.4) with $\hat{C} \neq 0$, it will be impossible to obtain simultaneous knowledge about the non-commuting observables $\hat{A}, \hat{B}$ with absolute precision.

[1] The mode function $\mathbf{u}_k$ can also contain polarization information.
[2] In the remainder of the thesis $\hbar$ will be set to 1 for convenience.
[3] $\hat{C}$ is frequently just a complex constant times the identity $\mathbb{1}$.

2.2 Quadrature operators

The creation and annihilation operators are not Hermitian and are thus not observables. However, they can be combined in the following way to create the so-called quadrature operators, which are in fact Hermitian:

$$\hat{X} \equiv \frac{1}{2}\left(\hat{a} + \hat{a}^\dagger\right) \tag{2.7}$$

$$\hat{P} \equiv \frac{1}{2i}\left(\hat{a} - \hat{a}^\dagger\right). \tag{2.8}$$

Arbitrary quadrature operator

We can generalize the previous definition to account for rotated quadratures $\hat{X}_\Phi$,

$$\hat{X}_\Phi = \frac{1}{2}\left(\hat{a}e^{-i\Phi} + \hat{a}^\dagger e^{i\Phi}\right) = \hat{X}\cos(\Phi) + \hat{P}\sin(\Phi) \tag{2.9}$$

Quadrature operators obey the following commutation relations[4]:

$$\left[\hat{X}, \hat{P}\right] = \frac{i}{2} = \left[\hat{X}_\Phi, \hat{X}_{\Phi+\pi/2}\right] \tag{2.10}$$

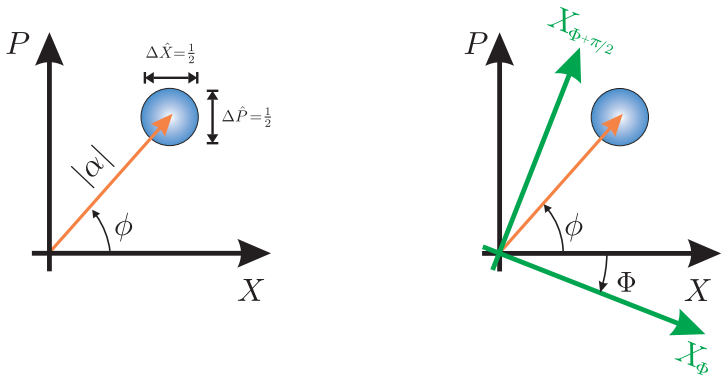

Figure 2.1: Quadratures in phase space. **Left:** A coherent state is shown in phase space, where quadratures $\hat{X}$ and $\hat{P}$ serve as coordinates, the uncertainty in the quadratures due to the quantum noise of the state is indicated. **Right:** (green) Rotated quadratures, the positive sense of rotation has been indicated for ϕ and Φ. This makes the equivalence between rotating the state and rotating the quadrature by the same amount.

[4]The definition 2.9 implies that $\hat{P}_\Phi = \hat{X}_{\Phi+\pi/2}$.

Normalization

It is possible to define the already mentioned quadrature operators in different ways by using another normalization factor, which is important as this has consequences in quantities like the quadrature variance or the lenght in phase space. One can write the expression for an arbitrary normalization factor γ as:

$$\hat{X}_{\Phi,\gamma} = \frac{\hat{a}e^{-i\Phi} + \hat{a}^\dagger e^{i\Phi}}{\gamma} \tag{2.11}$$

$$\hat{X}_{\Phi+\pi/2,\gamma} = \frac{\hat{a}e^{-i\Phi} - \hat{a}^\dagger e^{i\Phi}}{i\gamma} \tag{2.12}$$

In the quantum optics community there are three main conventions for γ: 1, $\sqrt{2}$ and 2. The advantages of each of them are analyzed below. Table 2.1 summarizes the main results for these cases and serves as a reference. In particular it shows the mean value and variance of the quadrature evaluated with a coherent state $||\alpha|\rangle$.

Table 2.1: Normalization of Quadrature Operators.

Norm.	$\boldsymbol{\gamma = 1}$	$\boldsymbol{\gamma = \sqrt{2}}$	$\boldsymbol{\gamma = 2}$
Expression	$\hat{X}_\Phi = \hat{a}e^{-i\Phi} + \hat{a}^\dagger e^{i\Phi}$	$\hat{X}_\Phi = \frac{1}{\sqrt{2}}(\hat{a}e^{-i\Phi} + \hat{a}^\dagger e^{i\Phi})$	$\hat{X}_\Phi = \frac{1}{2}(\hat{a}e^{-i\Phi} + \hat{a}^\dagger e^{i\Phi})$
Commutator	$\left[\hat{X}_\Phi, \hat{X}_{\Phi+\pi/2}\right] = 2i$	$\left[\hat{X}_\Phi, \hat{X}_{\Phi+\pi/2}\right] = i$	$\left[\hat{X}_\Phi, \hat{X}_{\Phi+\pi/2}\right] = i/2$
Mean value	$\left\|\left\langle \hat{X}_\Phi \right\rangle\right\| = 2\|\alpha\|$	$\left\|\left\langle \hat{X}_\Phi \right\rangle\right\| = 2\sqrt{2}\|\alpha\|$	$\left\|\left\langle \hat{X}_\Phi \right\rangle\right\| = \|\alpha\|$
Variance	$\Delta^2\hat{X}_\Phi = 1$	$\Delta^2\hat{X}_\Phi = \frac{1}{2}$	$\Delta^2\hat{X}_\Phi = \frac{1}{4}$
Inverse relation	$\hat{a} = \frac{e^{i\Phi}}{2}(\hat{X}_\Phi + \hat{P}_\Phi)$	$\hat{a} = \frac{\sqrt{2}e^{i\Phi}}{2}(\hat{X}_\Phi + \hat{P}_\Phi)$	$\hat{a} = e^{i\Phi}(\hat{X}_\Phi + \hat{P}_\Phi)$

- $\gamma = 1$

This case has the particularity that the variance of the vacuum fluctuations is $\Delta^2\hat{X} = 1$. It sets the shot noise level (SNL), and therefore refers all the variances to 1. Any $\Delta^2\hat{X} < 1$ will represent squeezing and $\Delta^2\hat{X} > 1$, excess noise.

- $\gamma = \sqrt{2}$

In this case, direct and inverse relations have the same factor γ.

- $\gamma = 2$

This normalization is useful as it allows an accurate phase space representation. For instance, the last column in table 2.1 shows $|\langle \hat{X}_\Phi \rangle| = |\alpha|$, which implies that we can directly treat the amplitude of a coherent state as its length in phase space, as depicted in Fig.2.1. This is in fact the normalization that we will use in this thesis.

2.3 Homodyne detection

Homodyne detection (HD) is an experimental technique that allows us to have direct access to the field quadratures. We will show that in fact, one can access an arbitrary quadrature $\hat{X}_\Phi$ of an input state by controlling the phase Φ of a local oscillator (LO).

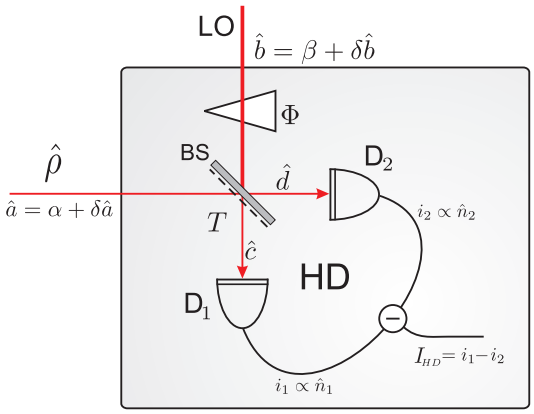

Figure 2.2: Homodyne detection (HD): The interference of an input state $\hat{\rho}$ with a local oscillator on a BS is recorded by photodetectors. The difference signal gives information about the quadrature $\hat{X}_\Phi$ as explained in the text.

If we interfere the input state $\hat{\rho}$ with a local oscillator on a beam splitter (BS) with transmittance T as in Fig.2.2 , we get:

$$\hat{c} = \sqrt{1-T}\hat{a} + \sqrt{T}\hat{b}e^{i\Phi} \tag{2.13}$$

$$\hat{d} = \sqrt{T}\hat{a} - \sqrt{1-T}\hat{b}e^{i\Phi} \tag{2.14}$$

Let us analyze the case of balanced homodyne detection $T = 1/2 = R$.

For simplicity, let us write the field operators as an amplitude plus a noise term [58]: $\hat{a} = \alpha + \delta\hat{a}$. We know that the photocurrent is proportional to the photon number $\hat{n}$, so, for each detector we have:

$$\hat{n}_1 = \hat{c}^\dagger\hat{c} \approx \frac{1}{2}\left[|\alpha|^2 + |\beta|^2 + 2|\alpha||\beta|\cos(\Phi) + |\alpha|(\delta\hat{X}^a + \delta\hat{X}^{LO}_{(-\Phi)}) + |\beta|(\delta\hat{X}^{LO} + \delta\hat{X}^a_\Phi)\right] \tag{2.15}$$

$$\hat{n}_2 = \hat{d}^\dagger\hat{d} \approx \frac{1}{2}\left[|\alpha|^2 + |\beta|^2 - 2|\alpha||\beta|\cos(\Phi) + |\alpha|(\delta\hat{X}^a - \delta\hat{X}^{LO}_{(-\Phi)}) + |\beta|(\delta\hat{X}^{LO} - \delta\hat{X}^a_\Phi)\right] \tag{2.16}$$

given that $|\beta| \gg |\alpha|$, we can approximate the previous to:

$$\hat{n}_1 \approx \frac{1}{2}\left[|\beta|^2 + 2|\alpha||\beta|\cos(\Phi) + |\beta|(\delta\hat{X}_{LO} + \delta\hat{X}^a_\Phi)\right] \tag{2.17}$$

$$\hat{n}_2 \approx \frac{1}{2}\left[|\beta|^2 - 2|\alpha||\beta|\cos(\Phi) + |\beta|(\delta\hat{X}_{LO} - \delta\hat{X}^a_\Phi)\right] \tag{2.18}$$

and if we take the difference:

$$\hat{n}_- = 2|\alpha||\beta|\cos(\Phi) + |\beta|\delta\hat{X}^a_\Phi, \tag{2.19}$$

we find that the difference of the photon number recorded by detectors D_1, D_2 (proportional to the current) gives the value of the projection of the state $\hat{\rho}$ onto the quadrature $\hat{X}^a_\Phi$. This makes the balanced homodyne detection, a very powerful technique able to perform phase-sensitive measurements. Fig 2.3 (left) shows HD time traces for different Gaussian states, where the LO phase varies harmonically with time.

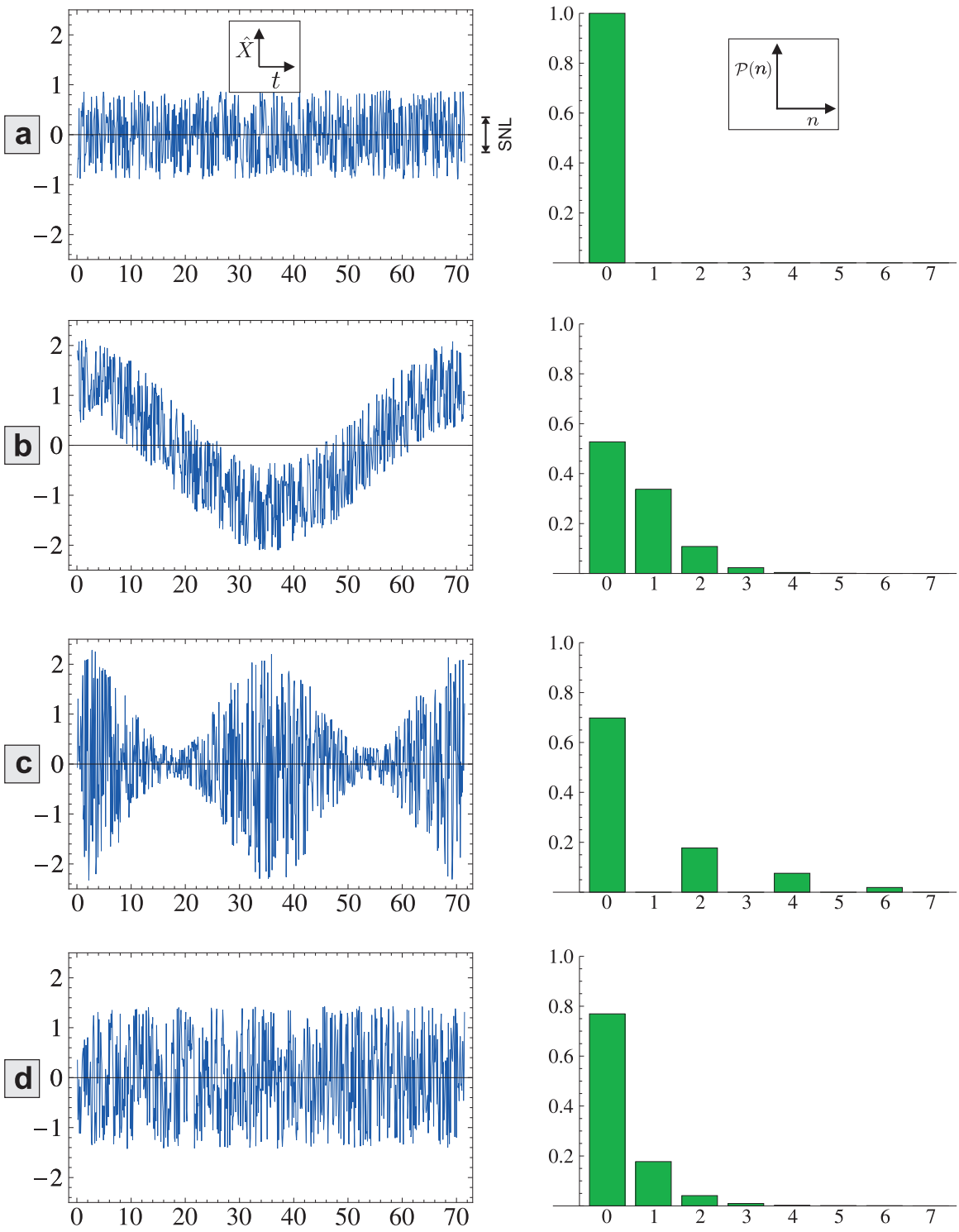

Figure 2.3: HD time traces (**left**) and Photon statistics (**right**) for different states: **a.** Vacuum **b.** Coherent **c.** Squeezed Vacuum **d.** Thermal state.

2.4 Density Operator (generalized preparation)

The state vector $|\psi\rangle$ represents the state of a quantum system when it is in a pure state. However, a pure state is rather a special case and we will need a more general definition of a quantum state as we will not only deal with pure states. The most general definition of a quantum state is given by the *density operator* [43], which for a pure state $|\psi\rangle$, is defined by the outer product:

$$\hat{\rho} \equiv |\psi\rangle\langle\psi|. \tag{2.20}$$

It is clear that in this case, the density operator contains the same information as the state vector (except for an overall phase). The density operator can represent coherent superpositions but its power lies in the fact that it can also represent incoherent superpositions. For example, let $\{|\psi_q\rangle\}$ be a set of states. Then the density operator

$$\hat{\rho} = \sum_q P_q |\psi_q\rangle\langle\psi_q| \tag{2.21}$$

expresses the fact that we do not know which of the states $|\psi_q\rangle$ the system is in, but we assign a weight P_q to the quantum state $|\psi_q\rangle$ in the mixture defined by $\hat{\rho}$. The weights obey

$$\sum_q P_q = 1 \tag{2.22}$$

for proper normalization of the density operator, and they can be interpreted as probabilities. The density operator can represent an ensemble of identical systems in possibly different states. A state of the form (2.20) is said to be a **pure state**. One that cannot be written in this form is said to be **mixed**.

2.4.1 The Density Matrix

The physical content of the density operator is more apparent when we compute the elements $\hat{\rho}_{qq'}$ of the density matrix with respect to a complete, orthonormal basis. The density matrix elements are given by

$$\hat{\rho}_{qq'} \equiv \langle q|\hat{\rho}|q'\rangle \tag{2.23}$$

To analyze these matrix elements, we will assume the simple form $\hat{\rho} = |\psi\rangle\langle\psi|$ of the density operator, though the arguments generalize easily to arbitrary density operators. The diagonal elements ρ_{qq} are referred to as populations, and give the measurement probability of the system in the state $|q\rangle$:

$$\hat{\rho}_{qq} = \langle q|\hat{\rho}|q\rangle = |\langle q|\psi\rangle|^2 \tag{2.24}$$

The off-diagonal elements $\rho_{qq'}$ (with $q \neq q'$) are referred to as coherences, since they give information about the relative phase of different components of the superposition. For example, if we write the state vector as a superposition with explicit phases,

$$|\psi\rangle = \sum_q |c_q| e^{i\theta_q} |q\rangle \tag{2.25}$$

then the coherences are

$$\rho_{qq'} = |c_q c_{q'}| e^{i(\theta_q - \theta_{q'})} \tag{2.26}$$

Notice that for a density operator not corresponding to a pure state, the coherences in general will be the sum of complex numbers corresponding to different states in the incoherent sum.

2.4.1.1 Expectation Values

The density matrix contains all the physically relevant information that we can possibly obtain and constitutes a general preparation of a quantum state. We can evaluate the statistical content of a certain state by using its density operator and an observable that describes the quantity of interest $\hat{A}$. The expectation value is given by:

$$\langle \hat{A} \rangle = \mathrm{Tr}[\hat{A}\hat{\rho}] \tag{2.27}$$

2.4.1.2 Purity

The purity, γ, of a quantum state is calculted with:

$$\gamma(\hat{\rho}) = \mathrm{Tr}[\hat{\rho}^2]. \tag{2.28}$$

its range is $1/d \leq \gamma(\hat{\rho}) \leq 1$, where d is the dimension of the associated Hilbert space. For pure states, we notice that

$$\hat{\rho}^2 = \hat{\rho}, \tag{2.29}$$

so we expect $\gamma_{pure} = 1$, while for mixed states we will have $\gamma_{mixed} < 1$.

2.4.1.3 Fidelity

Fidelity is a measure that evaluates how close two given states are. It represents a real value between 0 (orthogonal) and 1 (maximum fidelity). In the case that both states are pure, the definition is simply given as the inner product of these states:

$$F\left(|\psi_1\rangle\langle\psi_1|, |\psi_2\rangle\langle\psi_2|\right) = |\langle\psi_1|\psi_2\rangle|^2. \tag{2.30}$$

When one of them is impure, we can evaluate it as:

$$F\left(|\psi_1\rangle\langle\psi_1|, \hat{\rho}_2\right) = \langle\psi_1|\hat{\rho}_2|\psi_1\rangle \tag{2.31}$$

and the most general definition is:

$$F\left(\hat{\rho}_1, \hat{\rho}_2\right) = \left(\mathrm{Tr}\sqrt{\sqrt{\hat{\rho}_1}\hat{\rho}_2\sqrt{\hat{\rho}_1}}\right)^2. \tag{2.32}$$

Equation (2.32) is explicitly needed when both states are mixed, but can be used in the other cases as well.

2.5 Wigner, P and Q functions

It was already mentioned that any quantum state can be completely characterized by the density matrix $\hat{\rho}$, since all the statistical information can be extracted from it. It is possible and sometimes more convenient to give an alternative description of the state in terms of distribution functions [71] (in analogy to the classical probability distributions). In this section we present the most common quasiprobability distributions in quantum optics, which are representations equivalent to that of the density operator since they contain full information about the quantum states.

P function

The P function is often referred to as the *Glauber - Sudarshan P-representation* [73] and has the property that a point in phase space represents a single coherent state, so the P function of a coherent state $|\alpha_0\rangle$ is in fact a delta function: $P(\alpha) = \delta^2(\alpha - \alpha_0)$. The relation between the density matrix and the P function is:

$$\hat{\rho} = \int P\left(\beta\right)|\beta\rangle\langle\beta|\, d^2\beta. \tag{2.33}$$

When the P function is positive, it behaves as a classical distribution and in that case, we can interpret $\hat{\rho}$ in eq. (2.33) as a mixture of coherent states that follow the probability distribution $P\left(\beta\right)$.

Q function

The Q function is formed with the diagonal matrix elements of the density operator in the coherent state basis $\hat{\rho}_{\alpha\alpha}$:

$$Q(\alpha) = \frac{\langle\alpha|\,\hat{\rho}\,|\alpha\rangle}{\pi} \geq 0. \tag{2.34}$$

This is clearly a non-negative function since ρ is a positive operator. It is a bounded function:

$$Q(\alpha) < \frac{1}{\pi}, \tag{2.35}$$

and can be seen as a Gaussian convolution of the P function:

$$Q(\alpha) = \frac{1}{\pi} \int P(\beta)\, e^{-|\alpha-\beta|^2}\, d^2\beta \tag{2.36}$$

Wigner function

The Wigner function allows a direct visualization of a quantum state as a distribution over phase space. The shape of a state's Wigner function, allows to classify it as either Gaussian or non-Gaussian. In this thesis we will be mainly interested in Gaussian states for which the Wigner function proves to be an adequate tool. The definition of the Wigner function, $W(x,p)$ is [72]:

$$W(x,p) = \frac{1}{2\pi} \int_{-\infty}^{\infty} dy \left\langle x - \frac{y}{2} \right| \hat{\rho} \left| x + \frac{y}{2} \right\rangle e^{ipy} \tag{2.37}$$

The Wigner function is normalized:

$$\int_{-\infty}^{\infty} \int_{-\infty}^{\infty} dx\, dp\, W(x,p) = 1, \tag{2.38}$$

and its absolute value is bounded:

$$|W(x,p)| \leq \frac{1}{\pi}. \tag{2.39}$$

Marginal distributions

The Wigner function is real valued but could be negative. This is the reason why it is not considered as an actual probability distribution function but rather a quasiprobability distribution. We can, however, extract its marginals that are interpreted as actual probability distributions:

$$\mathcal{P}(x) = \int_{-\infty}^{\infty} dp\, W(x,p) \tag{2.40}$$

$$\mathcal{P}(p) = \int_{-\infty}^{\infty} dx\, W(x,p) \tag{2.41}$$

where $\mathcal{P}(x)$ and $\mathcal{P}(p)$ are probability distributions for $\hat{X}$ and $\hat{P}$ respectively. Furthermore, we can extract the marginal distributions along generalized quadratures (rotated by an angle Φ):

$$\mathcal{P}(x,\Phi) = \int_{-\infty}^{\infty} dp\, W(x\cos\Phi - p\sin\Phi, x\sin\Phi + p\cos\Phi) \tag{2.42}$$

Here $\mathcal{P}(x,\Phi)$ stands for the probability distribution for the arbitrary quadrature $\hat{X}_\Phi$.

Interestingly, the Wigner function is a Gaussian convolution of the P function:

$$W(\alpha) = \frac{2}{\pi}\int P(\beta)\, e^{-2|\alpha-\beta|^2}\, d^2\beta \tag{2.43}$$

Finally we observe that the Wigner function allows the calculation of operator moments on phase space by making use of the trace rule

$$\mathrm{Tr}[\hat{\rho}\hat{A}] = 2\pi\int_{-\infty}^{\infty} dxdp W_\rho(x,p) W_A(x,p) \tag{2.44}$$

with $W_\rho(x,p)$ being the Wigner function of $\hat{\rho}$ and $W_A(x,p)$:

$$W_A(x,p) = \frac{1}{2\pi}\int_{-\infty}^{\infty} dy \left\langle x-\frac{y}{2}\right| \hat{A} \left|x+\frac{y}{2}\right\rangle e^{ipy}. \tag{2.45}$$

2.6 Gaussian states

In many practical cases in the continuous variable (CV) regime, the shape of the Wigner function is Gaussian,

$$W(x,p) = \frac{1}{2\pi\Delta\hat{X}\Delta\hat{P}} \exp\left(-\frac{(x-\langle\hat{X}\rangle)^2}{2\Delta^2\hat{X}} - \frac{(p-\langle\hat{P}\rangle)^2}{2\Delta^2\hat{P}}\right), \tag{2.46}$$

and the corresponding quantum states are therefore called *Gaussian states* [47]. In this section we will analyze the most relevant cases, which are depicted in Fig. 2.4 (Wigner functions and density matrices) and in Fig 2.3 (HD time traces and photon number distributions).

2.6.1 Vacuum state

The ground state of the electromagnetic field is called the *vacuum state* $|0\rangle$. This state has the particularity of not containing photons: $\langle 0|\hat{n}|0\rangle = 0$, which in turn means that it is a *number state*, free of fluctuations in the Fock basis:

$$\Delta^2\hat{n} = \langle 0|\hat{n}^2|0\rangle - \langle 0|\hat{n}|0\rangle^2 = 0. \tag{2.47}$$

Interestingly, this state is at the same time (as we will see) a coherent state with no amplitude ($\langle\hat{X}\rangle = \langle\hat{P}\rangle$=0), and if one performs a quadrature measurement it will exhibit fluctuations (noise), in fact the variance of $\hat{X}$ and $\hat{P}$ quadratures for this state are found to be:

$$\Delta^2\hat{X} = \Delta^2\hat{P} = \frac{1}{4}. \tag{2.48}$$

Expression (2.48) implies that the vacuum state is a *minimum variance state* as it reaches the bound imposed by the Heisenberg uncertainty relations eq. (2.5). The vacuum noise is also referred to as *quantum noise* or *shot noise* and its variance constitutes a reference in quantum optics, known as the *quantum noise limit* (QNL).

2.6.2 Coherent state

The coherent state, first introduced by Glauber in [45] and [46], is the quantum mechanical state that most closely approximates the classical case, and can be defined as the eigenstate of the annihilation operator:

$$\hat{a}\,|\alpha\rangle = \alpha\,|\alpha\rangle \tag{2.49}$$

where the fact that $\hat{a}$ is not Hermitian allows the amplitude α to be complex.

The coherent state of light $|\alpha\rangle$ is a minimum uncertainty state, with equal uncertainties in any quadrature $\hat{X}_\Phi$. The quadrature variances are therefore identical to those of the vacuum state. Apart from vacuum, all coherent states contain photons and their mean number of photons is:

$$\langle\alpha|\hat{n}|\alpha\rangle = \langle\alpha|\hat{a}^\dagger\hat{a}|\alpha\rangle = |\alpha|^2. \tag{2.50}$$

Note that this result is independent of the normalization γ studied in sec. 2.2.They may also be expanded in terms of the number states $|n\rangle$ as

$$|\alpha\rangle = e^{-\frac{|\alpha|^2}{2}} \sum_{n=0}^{\infty} \frac{\alpha^n}{\sqrt{n!}}\,|n\rangle \tag{2.51}$$

Expression (2.51) can be used to calculate the probability of finding n photons in a coherent field, which turns out to be Poissonian:

$$\mathcal{P}(n) = |\langle n|\alpha\rangle|^2 = e^{-|\alpha|^2}\frac{|\alpha|^{2n}}{n!}. \tag{2.52}$$

2.6.2.1 The Displacement operator

Quantum states can be transformed by operators. An elementary transformation is the translation in phase space which is described by the unitary displacement operator:

$$\hat{D}(\alpha) = e^{\alpha\hat{a}^\dagger - \alpha^*\hat{a}} \tag{2.53}$$

its inverse amounts to an equal displacement in the opposite direction: $\hat{D}^{-1}(\alpha) = \hat{D}^{\dagger}(\alpha) = \hat{D}(-\alpha)$. An interesting feature of this operator is the fact that any coherent state can be created by displacing the vacuum state:

$$|\alpha\rangle = \hat{D}(\alpha)|0\rangle \tag{2.54}$$

2.6.3 Squeezed state

Squeezed states of light were discussed in the 1970s by Stoler [62] and Yuen [63]. The first experimental demonstration of squeezed light was carried out in 1985 by Slusher et al. [60] using four-wave mixing in a beam of Na-atoms inside an optical cavity, and by Wu et al. [61] using an optical parametric oscillator.

2.6.3.1 Squeezing operator

We could define the *squeezed vacuum* state as [48]:

$$|\zeta\rangle = \hat{S}(\zeta)\,|0\rangle \tag{2.55}$$

where the squeezing operator is

$$\hat{S}(\zeta) = \exp\left[\frac{1}{2}\zeta(\hat{a}^{\dagger})^2 - \frac{1}{2}\zeta^*(\hat{a})^2\right] \tag{2.56}$$

with $\zeta = re^{i\phi}$. The parameter $r \in [0, \infty)$ accounts for the degree of squeezing, while the phase factor ϕ defines the squeezing quadrature. The effect of the squeezing operator in eq. (2.55) is to reduce the variance of the vacuum along a specific quadrature. This implies that (to fulfill the Heisenberg uncertainty relation), the orthogonal quadrature has to increase its noise. The case of pure vacuum squeezed is still a minimum uncertainty state.

The number state expansion of the squeezed vacuum is given by:

$$\hat{S}(r)\,|0\rangle = \sum_{n=0}^{\infty} \left(\binom{2n}{n}\frac{1}{\cosh r}\right)^{\frac{1}{2}} \left(-\frac{1}{2}\tanh r\right)^{n} |2n\rangle \tag{2.57}$$

showing that the squeezed vacuum only contains an even number of photons. Squeezing and displacement can be combined[5] to produce the squeezed displaced state:

$$|\alpha, r\rangle = \hat{D}(\alpha)\hat{S}(r)\,|0\rangle \tag{2.58}$$

[5] They do not commute.

The mean photon number of such a state is given by:

$$\langle \hat{n} \rangle = |\alpha|^2 + \sinh^2(r) \tag{2.59}$$

Interestingly, we can conclude from the last equation that the squeezed vacuum state ($\alpha = 0$) contains photons.

2.6.4 Thermal state

The thermal state is a completely mixed state, with the following density matrix in the Fock basis:

$$\hat{\rho}_{\mathrm{Nth}} = \frac{1}{N_{\mathrm{th}} + 1} \sum_{n=0}^{\infty} \left(\frac{N_{\mathrm{th}}}{N_{\mathrm{th}} + 1} \right)^n |n\rangle\langle n| \tag{2.60}$$

where N_{th} is the mean number of thermal photons. $\hat{\rho}_{\mathrm{Nth}}$ contains only diagonal terms, so the state has no coherences and hence does not carry any phase information. This fact can also be seen from its Wigner function (in Fig. 2.4) and P function:

$$P(\beta) = \frac{e^{-|\beta|^2/N_{\mathrm{th}}}}{\pi N_{\mathrm{th}}} \tag{2.61}$$

which are Gaussian distributions centered in the origin of phase space, with no phase-dependent features.

2.7 POVMs (generalized measurements)

The idea of measurements in quantum theory is traditionally introduced as it was formulated by von Neumann [35]. Each physical property O is associated with an observable $\hat{O}$, where its eigenvalues are the possible results of a measurement of O. If the eigenvalues and eigenstates are, respectively, o_m and $|o_m\rangle$, we can write the operator $\hat{O}$ in the diagonal form:

$$\hat{O} = \sum_m o_m |o_m\rangle\langle o_m|. \tag{2.62}$$

If the system to be measured has been prepared in the state $|\psi\rangle$, then the probability that a measurement of O will give the result o_m is:

$$\mathcal{P}(o_m) = |\langle o_m|\psi\rangle|^2 \tag{2.63}$$

$$= \langle\psi|o_m\rangle\langle o_m|\psi\rangle \tag{2.64}$$

$$= \langle\psi|\hat{P}_m|\psi\rangle. \tag{2.65}$$

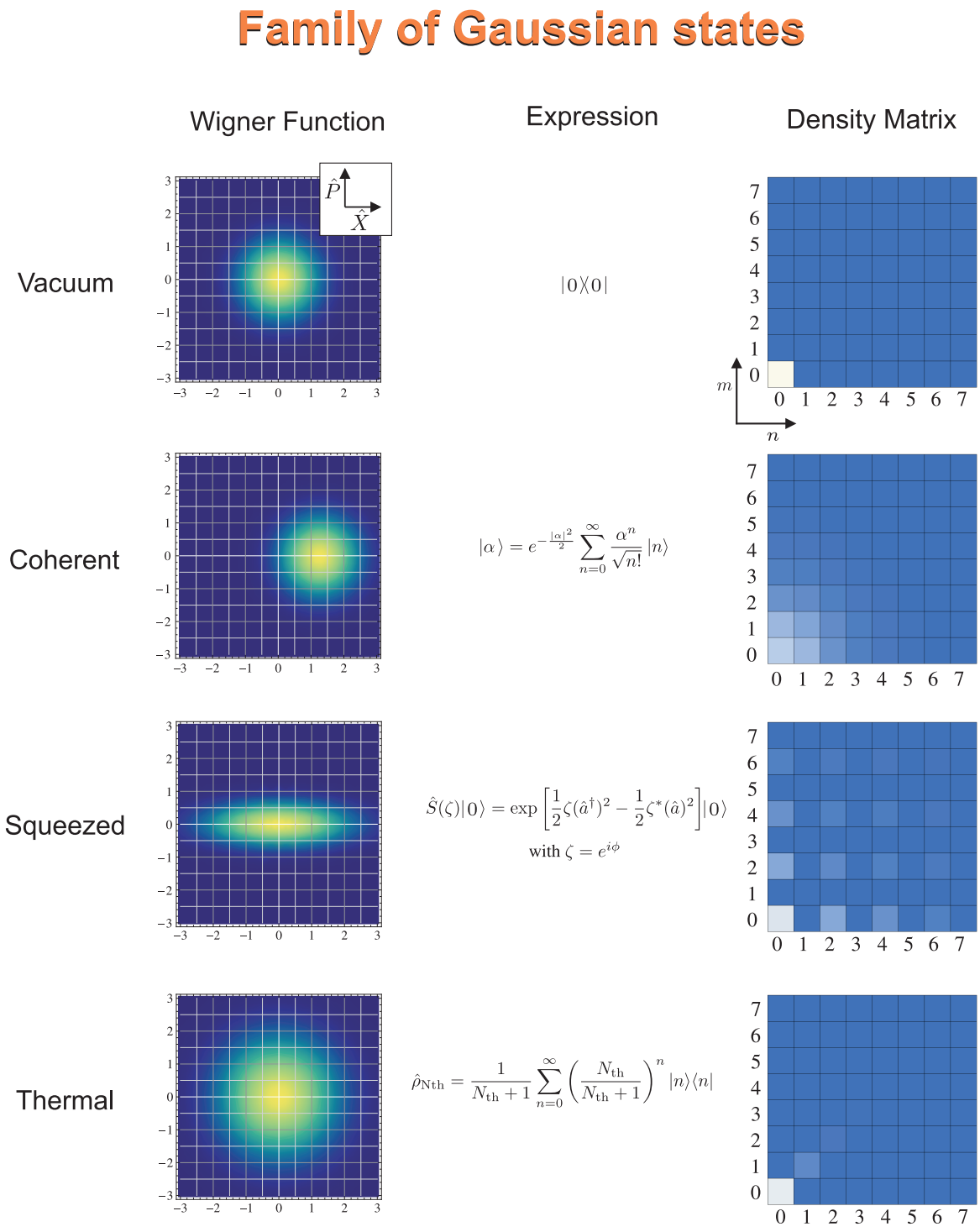

Figure 2.4: Familiy of Gaussian states. Their phase space picture, expression and density matrix' absolute values are shown.

This expression suggests that the probability $\mathcal{P}(o_m)$ can be seen as the expectation value of the operator $\hat{P}_m = |o_m\rangle\langle o_m|$. It turns out that such operators, P_m, are projectors since:

1. They are Hermitian: $\hat{P}_m^\dagger = |o_m\rangle\langle o_m| = \hat{P}_m$
2. They are positive operators $\langle\psi|\hat{P}_m|\psi\rangle \geq 0, \forall_{|\psi\rangle}$
3. They are complete $\sum_m \hat{P}_m = \mathbb{1}$
4. They are orthonormal $\hat{P}_m\hat{P}_n = \delta_{m,n}$

The kind of measurements that can be done with projectors $\hat{P}_m$ are often referred to as *von Neumann measurements*. They represent a kind of measurement where the system is projected onto one of the eigenstates of $\hat{O}_m$, and once the measurement is done, we end up with complete information about the respective observable. This projection is known as the *collapse of the wave function* and there is in principle no uncertainty as the measurement outcome is the corresponding eigenvalue.

There exist, in practice, other types of measurement were we only get part of the information about the given state, for example we can reduce the uncertainty regarding the observable of interest, without removing it completely. To account for this situations, we need to consider a larger class of measurements where we can describe measurements that extract only partial information.

POVMS are the most general type of measurements allowed by quatum mechanics, which include the traditional *projective* (or von Neumann) measurements. POVM stands for *Positive Operator Valued Measure*.

The theory of generalized measurements can be formulated simply by excluding the 4th requirement for projectors. So, we introduce a set of probability operators $\{\hat{\Pi}_m\}$, and we associate them with a measurement outcome such that the probability that our measurement gives the result labeled m is:

$$\mathcal{P}(m) = \langle\ \hat{\Pi}_m\rangle \tag{2.66}$$

If we keep the first three properties for the projectors, which allows us to maintain the probability interpretation (2.66), our probability operators have the following properties:

1. They are Hermitian: $\hat{\Pi}_m^\dagger = \hat{\Pi}_m$
2. They are positive operators $\langle\psi|\hat{\Pi}_m|\psi\rangle \geq 0, \forall_{|\psi\rangle}$

3. They are complete $\sum_m \hat{\Pi}_m = \mathbb{1}$

The three properties just described have a remarkable generality since any set of operators that satisfy these three properties correspond to a possible measurement and likewise, any real measurement can be described by the appropriate set of probability operators.

2.8 Phase probability distribution

The phase probability distribution $\mathcal{P}(\phi)$ of a quantum state, is understood here as the marginal distribution in phase space that uses the phase[6] ϕ as a parameter in a similar way that marginals $\mathcal{P}(x)$ and $\mathcal{P}(p)$ along the quadratures use x and p (respectively). A useful definition for $\mathcal{P}(\phi)$ in terms of generalized measurements is [18]:

$$\mathcal{P}(\phi) = \mathrm{Tr}\left[\hat{\rho}\hat{F}(\phi)\right], \tag{2.67}$$

where

$$\hat{F}(\phi) = \frac{1}{2\pi}\sum_{m,n=0}^{\infty} \exp(i\phi(m-n))|m\rangle\langle n|H_{mn} \tag{2.68}$$

is the POVM for a phase measurement with H being a measurement dependent matrix (positive and Hermitian). Moreover, it is worth noticing that $\hat{F}(\phi)$ obeys:

$$\hat{R}(\theta)\hat{F}(\phi)\hat{R}(-\theta) = \hat{F}(\phi+\theta), \forall\theta \in [0, 2\pi) \tag{2.69}$$

with $\hat{R}(\theta) = \exp(i\hat{a}^\dagger\hat{a}\theta)$. In the case of a canonical phase measurement:

$$H^{can}_{mn} = 1. \tag{2.70}$$

In the case of a Heterodyne measurement, we have:

$$H^{het}_{mn} = \frac{\Gamma\left(\frac{m+n}{2}+1\right)}{\sqrt{n!m!}} \tag{2.71}$$

2.8.1 Holevo variance

The traditional measure for variance:

$$V(A) = \left\langle A^2\right\rangle - \langle A\rangle^2 \tag{2.72}$$

[6] Refer to Chapter 4 for a more detailed description of the phase in quantum optics.

presents difficulties when using variables with an inherent periodicity, as is the case of the optical phase, which is a 2π-periodic variable. The problem is illustrated in Fig. 2.5, where the phase probability distribution function of a coherent state is plotted. If such a coherent state lies on the positive X axis, or close to it, eq. (2.72) gives the correct value for the phase variance, while if the state lies close to the negative X axis, $\phi \sim \pi$, the variance is increased to a value close to $(2\pi)^2$. This clearly makes no sense since the phase variance of a coherent state is independent of its phase.

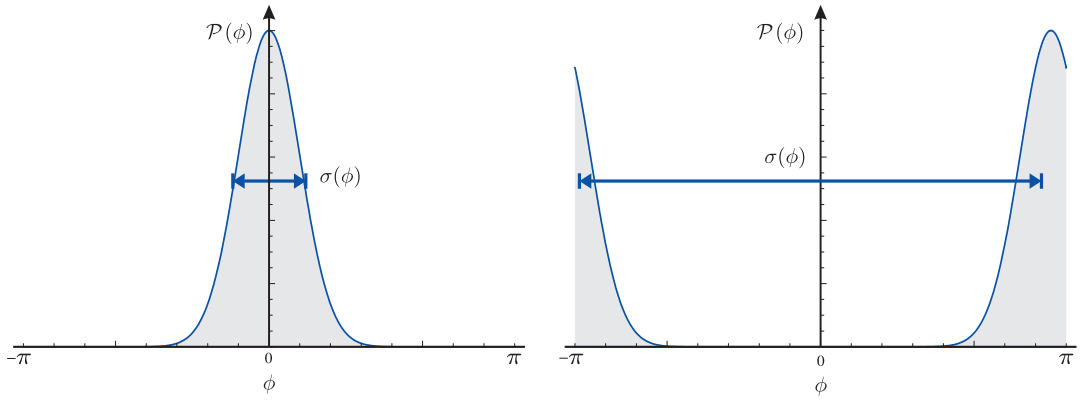

Figure 2.5: Phase variance problem. The phase probability distribution function $\mathcal{P}(\phi)$ is shown for two coherent states, with phases $\phi = 0$ and $\phi \sim \pi$. The standard deviation $\sigma(\phi) = \sqrt{V(\phi)}$ obtained by using the traditional definition eq. (2.72) is indicated.

In this thesis we will use an alternative definition for the phase variance that avoids this problem: The *Holevo phase variance* [2], defined as:

$$V^H = |\mu|^{-2} - 1. \tag{2.73}$$

V^H is a function of the state's phase where $\mu = \langle \exp(i\phi) \rangle$, the mean exponential phase, is known as the *sharpness* of the distribution, which for a canonical phase measurement can be obtained either by knowing the full density matrix $\hat{\rho}$ of the state or particularily by knowing its phase probability distribution $\mathcal{P}(\phi)$ as:

$$\langle \exp(i\phi) \rangle = \int_{-\infty}^{\infty} \mathcal{P}(\phi) \exp(i\phi) d\phi \tag{2.74}$$

The canonical phase probability distribution $\mathcal{P}(\phi)$ can be obtained from eq. (2.67) with $H = 1$ or equivalently from:

$$\mathcal{P}(\phi) = \frac{1}{2\pi} \langle \phi | \hat{\rho} | \phi \rangle \tag{2.75}$$

with phase states defined as:

$$|\phi\rangle = \sum_{n=0}^{\infty} e^{in\phi}|n\rangle \tag{2.76}$$

Summary of operators

Table 2.2: Most common operators in quantum optics.

Operator.	**Name**	**Expression**	**Type**
$\hat{a}$	Annihilation	$\hat{a}$	Non Hermitian
$\hat{a}^\dagger$	Creation	$\hat{a}^\dagger$	Non Hermitian
$\hat{n}$	Number	$\hat{a}^\dagger\hat{a}$	Hermitian
$\hat{\rho}$	Density	$\hat{\rho}$	Hermitian
$\hat{X}$	X quadrature	$\frac{1}{2}\left(\hat{a}^\dagger + \hat{a}\right)$	Hermitian
$\hat{P}$	P quadrature	$\frac{i}{2}\left(\hat{a}^\dagger - \hat{a}\right)$	Hermitian
$\hat{X}_\Phi$	Arbitrary quadrature	$\frac{1}{2}(\hat{a}e^{-i\Phi} + \hat{a}^\dagger e^{i\Phi})$	Hermitian
$\hat{D}(\alpha)$	Displacement	$\exp(\alpha\hat{a}^\dagger - \alpha^*\hat{a})$	Unitary
$\hat{D}^\dagger(\alpha)$	Displacement	$\hat{D}^\dagger(\alpha) = \hat{D}^{-1}(\alpha) = \hat{D}(-\alpha)$	Unitary
$\hat{S}(\zeta)$	Squeezing	$\exp\left[\frac{1}{2}\zeta(\hat{a}^\dagger)^2 - \frac{1}{2}\zeta^*(\hat{a})^2\right]$	Unitary
$\hat{R}(\theta)$	Phase Shift	$\exp(i\theta\hat{n})$	Unitary

Chapter 3

Quantum Amplifiers

Contents

3.1 Introduction

In applications such as Telecommunication, the amplification of a signal is frequently required. Examples of this can be seen every day: in satellite communication, cell phone repeater antennae, long distance transmissions through fiber optics, etc.
The function of an amplifier in such a communication scenario is in principle very simple: it receives a signal (that could be completely unknown in amplitude and phase), then it has to coherently inject extra energy into it (actual amplification) and finally send the resulting signal back into a communication channel. This might appear as an easy task, but surprisingly, deterministic noise-free amplification of an unknown state is in fact impossible as realized by Haus and Mullen in 1962 [3] and further studied by Caves in 1982 [4].

We know that any physical signal is in essence quantum mechanical, then a contradiction emerges: Amplification is used everyday but quantum mechanics prohibits its perfect implementation. The way to solve this apparent discrepancy is to realize that the signals used to carry the information in optical communications are normally coherent states, as in the fiber optics case. We then consider 2 scenarios:

1. If dim coherent states are used, as it happens after strong attenuation or loss in the communication channel, the quantum noise of the possible states may strongly overlap (Fig. 3.1a) that impedes a receiver to distinguish between them. In this case the classical description fails and perfect quantum amplification is impossible, as amplifying them will either maintain the overlap or make it worse.

2. A different situation occurs when such states have a moderate to large amplitude before entering the amplifier, then the overlap could practically disappear[1] (Fig. 3.1b). Moreover, the increased variance do not explicitly depend on the initial state's amplitude but only on the gain, so the effect of the added noise decreases with increasing amplitude and the signals behave just as classical waves, which explains their familiar behaviour in the cited applications[2].

The subject of Quantum amplification has recently attracted a lot of attention and various groups around the world have proposed and implemented different alternatives to amplification, both deterministic amplification at the ultimate quantum limit as well as probabilisitic amplification which may beat the standard limits. In this chapter, the mentioned impossibility of perfect quantum amplification will be described, the proposed alternatives will be presented and finally, in section 3.3 a novel concept of quantum amplification will be analyzed.

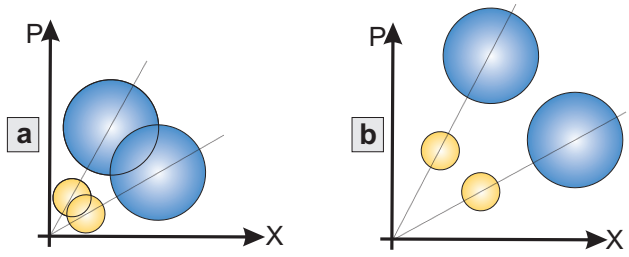

Figure 3.1: Overlap of coherent states before (yellow) and after (blue) amplification. **a.** dim coherent states **b.** coherent states with slightly larger amplitude

[1]The larger the amplitude, the closer to orthogonal they become: i.e. the overlap between 2 coherent states is given by $|\langle\alpha_1|\alpha_2\rangle|^2 = \exp\left(-|\alpha_1 - \alpha_2|^2\right)$

[2]It is important to notice that even in this case, the amplification produces extra noise, but the effect of this noise is minimun as a detector can distinguish between the different states.

3.2 Impossibility of perfect Amplification

It is important to clearly state what is actually impossible[3] in quantum amplification and it can be sumarized as:

> It is impossible to **noiselessly** and **deterministically** amplify an **unknown** input quantum state.

To clarify the terms, *noiselessly* means that the amplifier should not add noise to the output and *deterministically* means that the device should correctly perform the amplification in a single shot (one output for one input), every time it is used. It is also important to stress that the state is assumed to be *unknown*[4]. The aim of this section is to explain this impossiblility, first by giving an argument based on a well known theorem (subsec. 3.2.1), which will be later confirmed with a more general proof (subsect. 3.2.2), that shows that the output of any deterministic amplifier with an unknown input, will always be noisy.

3.2.1 No-cloning argument

The no-cloning theorem [32] has been widely discussed and tested over the years and in fact is now a corner stone in quantum information science. Interestingly, its proof requires only a few lines:

Lets take two generic states $\{|\phi\rangle, |\psi\rangle\}$ and assume that there is a unitary transformation U_{cl} that can independently make a perfect copy of each of them:

$$|\phi\rangle|0\rangle \xrightarrow{U_{cl}} |\phi\rangle|\phi\rangle \tag{3.1}$$

$$|\psi\rangle|0\rangle \xrightarrow{U_{cl}} |\psi\rangle|\psi\rangle \tag{3.2}$$

Now we only need to find the inner product of these states, and use the previous information to arrive at:

$$\langle\phi|\psi\rangle = (\langle\phi|\langle 0|)\,(|\psi\rangle|0\rangle) \tag{3.3}$$

$$= (\langle\phi|\langle\phi|)\,(|\psi\rangle|\psi\rangle) \tag{3.4}$$

$$= \langle\phi|\psi\rangle^2 \tag{3.5}$$

[3] In Physics, the expression "*It is impossible to...*" has to be used with care, as new experiments could at any time defy a physical theory so, it should be safer to read it as "*The currently accepted theory states that it is impossible to...*" but when facts are so well described by the theory and experimentally confirmed over years, there is no harm in writing it in the short form.

[4] If complete knowlege of the initial state were available, perfect cloning would be possible, requiring only a unitary transformation that uses the information about the state. In the case of coherent states such a transformation is a displacement.

Now, this means that our assumption has the condition: $\langle\phi|\psi\rangle = \langle\phi|\psi\rangle^2$ which is satisfied only if the states are orthogonal or if $|\psi\rangle = |\phi\rangle$, so in general there exists no such unitary transformation and we can state:

> An unknown quantum state cannot be cloned, that is, we cannot deterministically get two identical copies of the original [5].

It is straightforward to show that if perfect cloning is prohibited, deterministic amplification is also prohibited. Let us consider the case of coherent states: If a perfect amplifier existed, we could use it with gain $g = \sqrt{2}$ as a first stage in a set up as in Fig. 3.2, then we would only need to send the ouput of the amplifier to a 50:50 BS and introduce an extra phase flip in one of the outputs. This would produce 2 perfect copies of the original unknown coherent state:

$$|\alpha\rangle|0\rangle \xrightarrow{\text{Amplifier}} |\sqrt{2}\alpha\rangle|0\rangle \xrightarrow{\text{BS}} |\alpha\rangle|\alpha\rangle \tag{3.6}$$

which clearly violates the no-cloning theorem. Here we conclude that perfect cloning and amplification belong to the same class of prohibited operations in quantum mechanics.

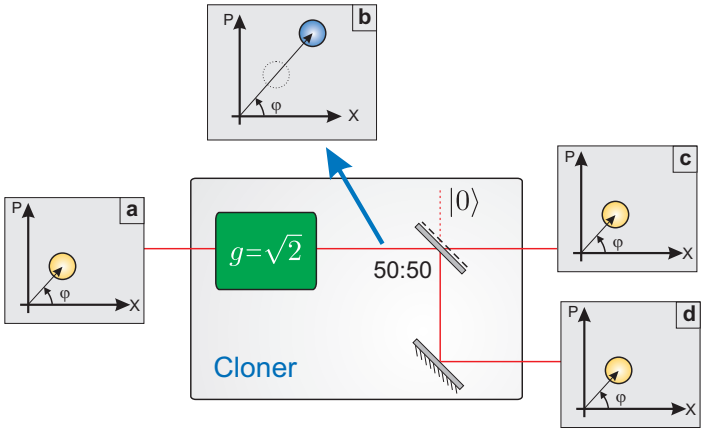

Figure 3.2: A perfect cloner could be built by using a perfect amplifier with gain $g = \sqrt{2}$ and a 50:50 BS. **a.** Input, **b.** Amplified state, **c.** and **d.** Perfect clones.

[5] It is possible, however, to obtain copies with fidelity $F < 1$. A scheme for optimal cloning of coherent states can be found in [37]

3.2.2 Phase Insensitive Linear Amplifier

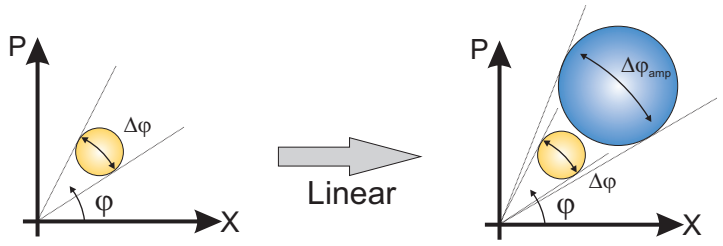

Figure 3.3: Effect of a Linear amplifier on an input coherent state.

The theoretical description of the linear amplifier was originally made by Haus and Mullen [3] and reformulated in terms of fundamental theorems by Caves [4]. A simplified description of the linear amplifier is as follows: first, we demand bosonic modes for both input and output, so the following commutation relations have to be fulfilled:

$$\left[\hat{a}_{in}, \hat{a}_{in}^{\dagger}\right] = 1, \tag{3.7}$$

$$\left[\hat{a}_{out}, \hat{a}_{out}^{\dagger}\right] = 1 \tag{3.8}$$

A linear amplifier can be either phase-sensitive or phase-insensitive, however, in what follows, we are specifically interested in a phase-insensitive linear amplifier (PILA). The linearity refers to a linear relation between input and output modes, and phase-insensitive (or phase-preserving) implies that both quadratures undergo equal amplification, so the simplest expression complying with these conditions would be:

$$\hat{a}_{out} = \sqrt{G}\hat{a}_{in} \tag{3.9}$$

$$\hat{a}_{out}^{\dagger} = \sqrt{G}\hat{a}_{in}^{\dagger} \tag{3.10}$$

where $G = g^2$, $(g > 1)$ is the photon number gain. This clearly does not preserve the commutation relations since $\left[\hat{a}_{out}, \hat{a}_{out}^{\dagger}\right] = G$, and an extra term has to be added:

$$\hat{a}_{out} = \sqrt{G}\hat{a}_{in} + \hat{\mathbb{F}} \tag{3.11}$$

$$\hat{a}_{out}^{\dagger} = \sqrt{G}\hat{a}_{in}^{\dagger} + \hat{\mathbb{F}}^{\dagger} \tag{3.12}$$

where $\hat{\mathbb{F}}$ is an operator associated with the internal modes of the amplifier and is responsible for the added quantum noise in the amplification process. This noise may have different origins, depending on the physical processes involved. Examples

of this noise are spontaneous emission in laser amplification or addition of vacuum fluctuations of the idler mode to the output signal in parametric amplifiers and four wave mixers.

This noise is expected to be uncorrelated with the input $[\hat{\mathbb{F}}, \hat{a}_{in}] = [\hat{\mathbb{F}}^\dagger, \hat{a}_{in}] = 0$, and we get:

$$\left[\hat{\mathbb{F}}, \hat{\mathbb{F}}^\dagger\right] = 1 - G \tag{3.13}$$

Now we can express the relations between input and output variances:

$$\begin{aligned}(\Delta\hat{a}_{out})^2 &= G\,(\Delta\hat{a}_{in})^2 + \frac{1}{2}\left\langle\left\{\hat{\mathbb{F}}, \hat{\mathbb{F}}^\dagger\right\}\right\rangle \\ &\geq G\,(\Delta\hat{a}_{in})^2 + \frac{1}{2}\left\langle\left[\hat{\mathbb{F}}, \hat{\mathbb{F}}^\dagger\right]\right\rangle \\ &\geq G\,(\Delta\hat{a}_{in})^2 + \frac{|G-1|}{2}\end{aligned} \tag{3.14}$$

Here we can see explicitly that the output of every phase insensitive linear amplifier will contain extra noise as compared to the input, and the quantum limit in linear amplification is set by the equal sign in (3.14) [4]. As mentioned before, the noise addition represented by $\hat{\mathbb{F}}$ can be atributed to internal degrees of freedom, and a simple expression for this is $\hat{\mathbb{F}} = \sqrt{G-1}\hat{a}^\dagger_{int}$ and so we arrive at the well known formula for the linear quantum amplifier:

$$\hat{a}_{out} = \sqrt{G}\hat{a}_{in} + \sqrt{G-1}\hat{a}^\dagger_{int} \tag{3.15}$$

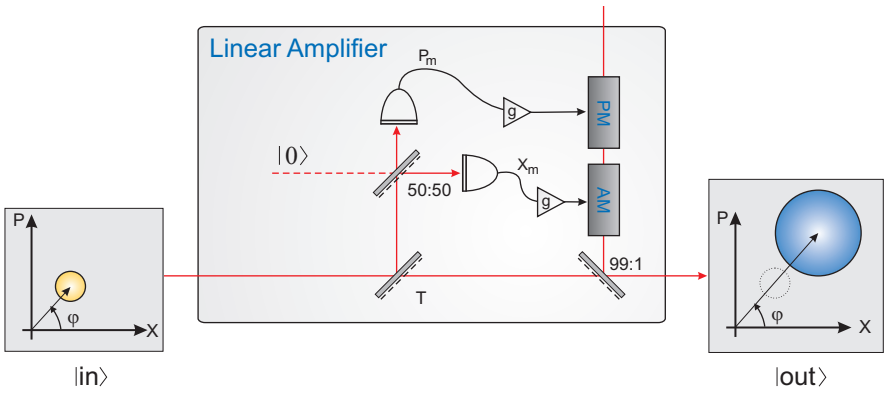

Figure 3.4: Example of a linear amplifier setup. A fraction of the input state state is sent to a 50:50 BS where it is split to measure conjugate quadratures (X_m, P_m). This information is fedforward to a displacement device composed by an auxiliary beam, amplitude and phase modulators (AM and PM) and 99:1 BS.

It is perhaps more appealing from the experimental point of view to express this noise addition in the familiar form of Hermitian quadrature operators, corresponding to observables that can be accessed in the lab:

$$V_{out}(\theta) = GV_{in}(\theta) + (G-1)V_{int}(\theta) \tag{3.16}$$

where: $V(\theta) = \langle(\hat{X}_\theta - \langle\hat{X}_\theta\rangle)^2\rangle$ and $\hat{X}_\theta$ is defined as in (2.9).

One experimental realization of this type of amplifier for coherent states, was carried out by Josse et al. [6]. Their setup is shown in Fig. 3.4 where they remarkably use only linear optics and feed-fordward. In their case a small fraction of the initial coherent state is used to identify it, and this information is employed later to make a displacement operation on the transmitted state to perform the amplification. For the identification of the reflected state, they measure conjugate quadratures (X_m, P_m) simultaneously, which implies a noise penalty of 3dB on each quadrature and therefore the displacement (amplification) will be noisy. The origin of the noise in this case is the injection of vaccum in the unused input port of the 50:50 BS, that splits the state to measure conjugate quadratures.

3.2.3 Probabilistic Noiseless Amplifiers

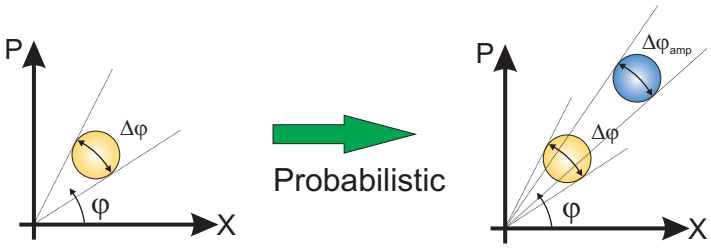

Figure 3.5: Effect of a probabilistic amplifier on an input coherent state.

If one gives up the demand for a deterministic behaviour of the amplifier, or in other words, if one can afford not to have correct amplification for every incoming state but rather for a fraction of them, then the unwanted extra noise can be reduced or even eliminated. It is referred to as probabilistic (or non-deterministic) noiseless amplification. In the following, we describe various different proposals and realizations of noiseless amplification.

3.2.3.1 Quantum Scissors approach

The original proposal of quantum scissors [29] and its experimental realization [30], aimed at teleporting an initial state, but as the resource was an entangled single photon (asymmetric BS in Fig. 3.6), the actual output had a reduced Hilbert space. The teleported state belongs to the 2 dimensional Hilbert space given by a superposition of $|0\rangle$ and $|1\rangle$ that is conditioned on the outcomes of two click detectors.

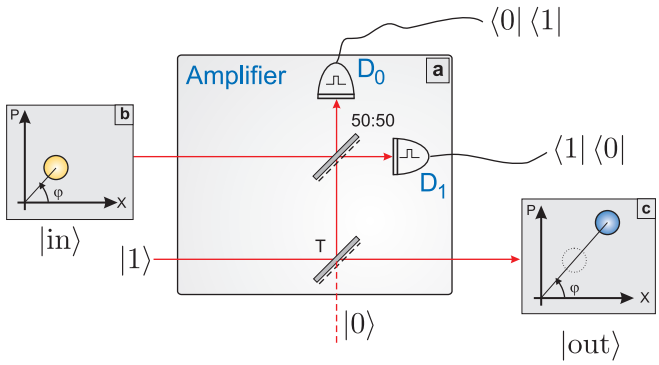

Figure 3.6: Quantum scissors approach to quantum amplification. Click detectors D_0 and D_1 condition the successful amplification of an initial weak coherent state, as explained in the text.

Following this idea, Ralph and Lund realized that the quantum scissors' architecture could be used as a probabilistic quantum amplifier and made a theoretical proposal [7]. In short, the operation of the amplifier is as follows: The output will be heralded under the condition of having a single photon-detection on detector D_1 in Fig. 3.6 and none in the other. This detected photon is the result of two indistinguishable possibilities: it either came from the input state $|\alpha\rangle$ or from the auxiliary single photon. If the click came from the single photon, the output will be vaccum otherwise, it is $|1\rangle$. Under this condition, as it cannot be told where the detected photon came from, the output state will be given by the coherent superposition:

$$|\text{out}\rangle = r|0\rangle + t\alpha|1\rangle \tag{3.17}$$

In this amplifier, the gain can be controlled by manipulating the transmission of the asymmetric BS as: $t/r = g > 1$, and the output can be written as[6]:

$$|\text{out}\rangle = |0\rangle + g\alpha|1\rangle \simeq |g\alpha\rangle \tag{3.18}$$

[6]It should be noticed that the same result is expected if the role of the detectors is interchanged and the output is phase shifted.

In this way, when dim coherent states are used, this amplifier performs approximately the transformation:

$$|\alpha\rangle \rightarrow |g\alpha\rangle \tag{3.19}$$

The groups of Grangier [8] and Pryde [9] performed independent experiments to demonstrate Ralph and Lund's idea, using different ways to characterize the output state.

3.2.3.2 Photon addition/subtraction approach

An alternative for achieving probabilistic noiseless amplification is by performing a specific sequence of photon addition and subtraction[10] [13]. A noiseless quantum amplifier can be described in terms of a Non-unitary operator :

$$\hat{G} = g^{\hat{n}} \tag{3.20}$$

The effect of the amplifier is to transform $|n\rangle$ into $g^{\hat{n}}|n\rangle$, where $\hat{n}$ is the photon number operator. By making an expansion upto N terms we get:

$$\hat{G} = \sum_{k=0}^{N} \frac{(d\hat{n})^k}{k!} \tag{3.21}$$

Let us we approximate the amplifier by taking the first 2 terms ($N = 1$). To ensure that g corresponds to the effective gain, we need: $d = g - 1$ [13]. In this case the amplifier is simplified to the following sequence of photon subtraction and additions:

$$\hat{G} = (g-1)\hat{n} + 1 \tag{3.22}$$

$$= (g-2)\hat{a}^\dagger\hat{a} + \hat{a}\hat{a}^\dagger \tag{3.23}$$

which for $g \neq 2$ is still very difficult to implement experimentally, so we set $g = 2$

$$\hat{G}_{g=2} = \hat{a}\hat{a}^\dagger \tag{3.24}$$

and now, this version of the amplifier ($N = 1$, $g = 2$) can be realized experimentally, as a similar sequence was demonstrated earlier [33].

If applied to a weak coherent state $|\alpha\rangle \simeq |0\rangle + \alpha|1\rangle$, the noise-free amplification process and be easily deduced theoretically:

$$\hat{G}_{g=2}|\alpha\rangle \simeq \hat{a}\hat{a}^\dagger\left(|0\rangle + \alpha|1\rangle\right) \tag{3.25}$$

$$= |0\rangle + 2\alpha|1\rangle \simeq |2\alpha\rangle \tag{3.26}$$

The experimental demonstration of this amplifier was carried out by Zavatta et al.[28] with a setup based on the conceptual diagram shown in Fig. 3.7. The boxes represent a coherent photon addition, $\hat{a}^{\dagger}$-box (experimentally demanding, [33]) and photon subtraction $\hat{a}$-box. To characterize their state, they performed quantum tomography, and as in the case of Grangier, they looked for the effective gain as a function of the initial coherent amplitude.

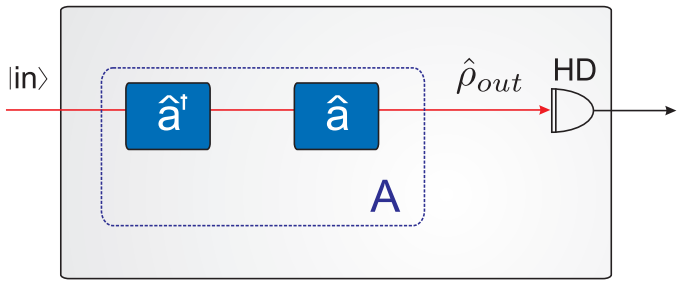

Figure 3.7: Conceptual diagram of the photon addition/subtraction noiseless amplifier. The blue boxes represent individual creation/annihilation operations.

A theoretical comparison of the performance of the scissors' and photon addition/-subtraction noiseless amplifiers regarding their effective gain, can be seen in Fig. 3.8. Here it is evident that the effective gain is rapidly degrading with increasing input amplitude $|\alpha|$ in the scissors approach whereas the addition/subtraction approach seems more versatile.

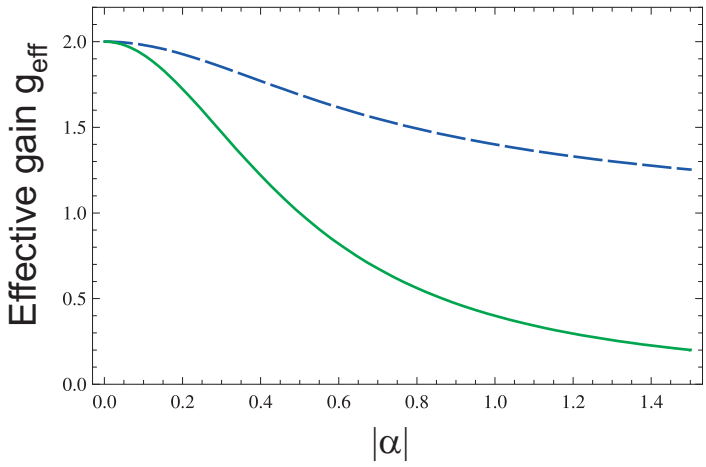

Figure 3.8: Effective gain comparison. The quantum scissors' approach (solid green line) vs photon addition/subtraction (dashed blue line).

3.3 Noiseless Concentration of Phase Information

"In order to attain the impossible,
one must attempt the absurd."

Miguel de Cervantes Saavedra

3.3.1 Introduction

In the previous section, we saw that noise-free amplification is attainable by allowing for a probabilistic operation. Sometimes the amplification operation does not work noiselessly in which case the output will be discarded, and sometimes it works in a nearly noiseless way. Two different experimental realizations were outlined, and both were quite experimentally demanding as they rely on single photons sources, photon addition/subtraction operations and complicated interferometric setups. In this section we will discuss a radically different noiseless amplifier that it is capable of amplifying the phase information noiselessly without the use of any non-classical resources or any strong parametric interactions. Remarkably, the source of energy is a thermal light source, so **the noise-free amplifier is based on the addition of noise!** This type of amplifier has been proposed in ref. [10] and its experimental realization was conducted as a part of this thesis and published in Nature Physics [49]. In this section, we describe in detail the idea and the experimental realization.

Description

We already mentioned in section 3.2.3.2 that by adding photons coherently to an initial coherent state and subsequently subtracting them, the state can be amplified noiselessly. This approach proved to be remarkably difficult to set up experimentally, because even the most simple case, where the amplifier has the form $\hat{G}_{g=2} = \hat{a}\hat{a}^{\dagger}$, is experimentally challenging[7]. But is all this complication really necessary?
Interestingly, it has been realized that there is a more direct procedure, that consists in adding the photons incoherently (instead of coherent addition), followed by a photon subtraction, which amplifies the state nearly noiselessly [10]. In other words, by substituting the highly sophisticated coherent photon addition operation with a thermal source, it is still possible to enable noiseless amplification to a certain extent.

[7] This is the only case of this type of amplifier demonstrated experimentally [28].

Our scheme is illustrated in Fig.3.9. The first operation is the addition of Gaussian noise to a coherent state which produces a displaced thermal state as shown in the phase space diagram. Next, we tap off a small fraction of the beam in an asymmetric beam splitter ($R \ll 1$) and measuring the reflected part with a photon number resolving detector (PNRD). We subsequently herald the state based on the measurement outcomes: If say M photons or more are detected the state is kept, otherwise it is discarded. This effectively corresponds to the subtraction of M (or more) photons from the displaced thermal state, and thus the action will increase

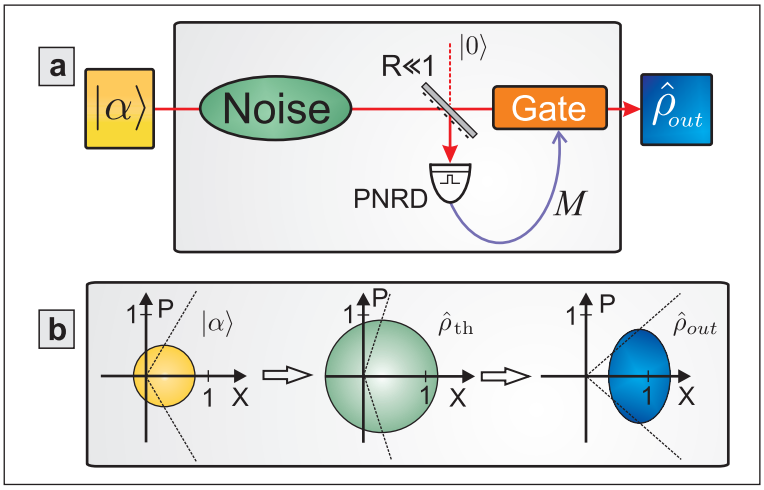

Figure 3.9: **Sketch of procedure and states.**

a. Sketch of the procedure described in the text. **b.** Phase space distributions of the input coherent (yellow), displaced thermal (green) and output state (blue). The dashed lines indicate the phase variance

the amplitude, conserve the mean value of the phase and reduce the phase variance. Because the mean value of the phase is unchanged and the noise is reduced, the signal to noise ratio is increased.

For a simple understanding of the operation, let us assume again a small coherent state $|\alpha\rangle \simeq |0\rangle + \alpha|1\rangle$ with weak Gaussian noise addition followed by single photon subtraction. The resulting state is [10]

$$\hat{\rho} \approx \frac{1}{|\alpha|^2 + N_{\rm th} + 4|\alpha|^2 N_{\rm th}} \left[|\alpha|^2 |0\rangle\langle 0| + N_{\rm th}(|0\rangle + 2\alpha|1\rangle)(\langle 0| + \langle 1|2\alpha^*)\right] \tag{3.27}$$

with the (canonical) Holevo phase variance (sec. 2.8.1):

$$V_{amp}^{H} \approx \frac{1}{4|\alpha|^2}\left(1 + \frac{|\alpha|^2}{N_{\rm th}}\right) - 1, \tag{3.28}$$

where it is assumed that the average number of incoherently added photons is $N_{\rm th} \ll 1$. We quantify the performance of the amplifier by the normalized phase variance, $\Gamma = V^H_{amp}/V^H_{in}$ which for a noiseless operation is smaller than one. For the above approximative example, if $|\alpha|^2 \ll N_{\rm th}$, we find that the normalized variance approaches $\Gamma = 1/4$. Another parameter that will be used to evaluate the amplifier is the gain $g = |\beta|/|\alpha|$ (where β is the average amplitude of the output state), being $g = 2$ for the above example. We therefore see that by simply adding a small amount of noise to the input state followed by a single photon subtraction it is possible to create an output state with twice the amplitude and with a reduced phase variance.

3.3.2 Theory

A more detailed theoretical description is as follows. The P function of the initial coherent state after the addition of thermal noise is represented by:

$$P(\beta) = \frac{e^{-|\beta-\alpha|^2/N_{\rm th}}}{\pi N_{\rm th}} \tag{3.29}$$

which is a displaced thermal state, containing on average $N_{\rm th}$ thermal photons and is centered at the initial coherent state $|\alpha\rangle$, in phase space. This P function is positive, as a thermal state can be seen as a collection of coherent states (Fig. 3.10b), and therefore it can be interpreted as an actual probability distribution, that dictates how the ensemble of coherent states is distributed in phase space.

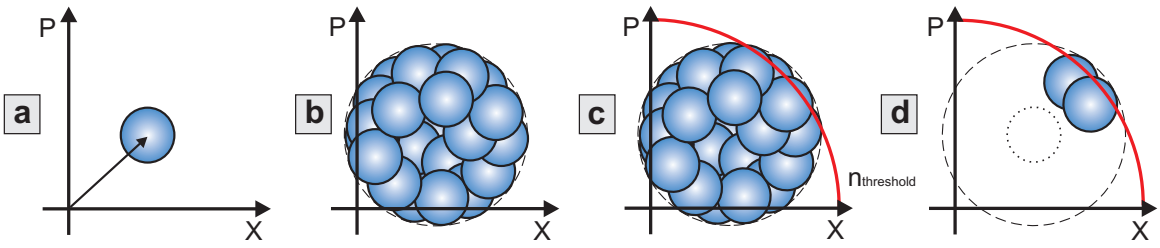

Figure 3.10: Phase space diagram of the following states as seen by the HD detector (after the tap): **a.** the input state **b.** the displaced thermal state **c.** the displaced thermal state and the threshold that is imposed by the photon counting sitting on the other arm (refer to footnote: #8). **d.** the heralded amplified output.

The second stage of the amplifier should condition the output on the successful subtraction of M or more photons from this thermal state. To achieve this subtraction, we tap off a part of the beam with a beam splitter of transmittance T. The reflected part is then directed to a detector that is able to resolve the amount of

photons it receives (PNRD) as mentioned before. The conditioning is made on the outcomes of the PNRD and the complete POVM (detector+conditioning) reads:

$$\hat{\Pi}_1^M = \sum_{n=0}^{M-1} |n\rangle\langle n| \tag{3.30}$$

$$\hat{\Pi}_2^M = \sum_{n=M}^{\infty} |n\rangle\langle n| \tag{3.31}$$

which represents a binary decision on a threshold detector, where M is the number of detected photons. Every time that less than M photons are detected (i.e. subtracted from the transmitted beam), the output is discarded. The successful operation is therefore given by $\hat{\Pi}_2^M$ and as it is applied to the reflected beam we have:

$$\mathcal{P}_\Pi(\beta) = \left\langle \sqrt{\eta(1-T)}\beta \right| \hat{\Pi}_2^M \left| \sqrt{\eta(1-T)}\beta \right\rangle \tag{3.32}$$

This expresses the probability to have M or more detected photons on a detector with quantum efficiency η, placed on the reflected port of an asymmetric BS (with transmission T), when the input is a generic coherent state $|\beta\rangle$. It is now straightforward to write the density matrix of the output state as the weighted sum of the transmitted coherent states, $|\sqrt{T}\beta\rangle$, conditioned as described above:

$$\hat{\rho}_{\text{out}} = \frac{1}{P_S} \int P\left(\frac{\beta}{\sqrt{T}}\right) \mathcal{P}_\Pi\left(\frac{\beta}{\sqrt{T}}\right) |\beta\rangle\langle\beta| \frac{d^2\beta}{T} \tag{3.33}$$

The normalization P_S gives the probability of success:

$$P_S = \int P\left(\frac{\beta}{\sqrt{T}}\right) \mathcal{P}_\Pi\left(\frac{\beta}{\sqrt{T}}\right) \frac{d^2\beta}{T} \tag{3.34}$$

Now we can use this theoretical description along with Fig. 3.10 to understand qualitatively the operation of the amplifier. As before, the description is in terms of individual coherent states: The conditioning is indicated in Fig. 3.10c., where the red circumference represents the threshold of M photons[8], as seen on the phase space of the output state. Only coherent states that are on the circumference or outside it are likely to produce M or more clicks in the detector. Since the states in the transmitted and reflected modes are classically correlated, the conditioning we apply (3.32) on the PNRD, selects the transmitted coherent states with the highest excitation and the proper direction in phase space. The result is an amplified state with reduced phase

[8]Note that the threshold suggested by the red line in Figs. 3.10 and 3.12 is just a visual aid to get some intuition about the effect of PNRD conditioning seen from the output state's phase space. It is, however, good enough to understand the behavior at this level.

variance as sketched in Fig. 3.10d.

Now, to quantitatively evaluate the performance of the amplifier, it is convenient to obtain an expression for the density matrix (3.33) in the familiar base of Fock states. Since this is the same representation that we obtain experimentally after doing tomography, such expression will also allow a direct comparison between theory and experiment. The density matrix elements ($\hat{\rho}^{\text{out}} = \sum \hat{\rho}^{\text{out}}_{nm} |n\rangle\langle m|$) in the Fock basis are:

$$\hat{\rho}^{\text{out}}_{nm} = \int e^{-|\beta|^2} \frac{\beta^m \beta^{*n}}{\sqrt{m!n!}} P\left(\frac{\beta}{\sqrt{T}}\right) \mathcal{P}_{\Pi}\left(\frac{\beta}{\sqrt{T}}\right) \frac{d^2\beta}{P_S T} \tag{3.35}$$

where the detection function can be explicitly given by:

$$\mathcal{P}_{\Pi}(\beta) = 1 - \sum_{k=0}^{M-1} \frac{(\eta(1-T)|\beta|^2)^k}{k!} e^{-(\eta(1-T)|\beta|)^2} \tag{3.36}$$

The performance of this amplifier is basically characterized by two key quantities: the gain and the phase variance. We can use the density matrix to calculate them which as follows:

Gain (g)

Our gain is defined as the ratio between the average amplitudes of the output with respect to the input state. To evaluate these amplitudes we use the quadrature operator along the input state's phase $\hat{X}_\Phi$:

$$g = \frac{\text{Tr}[\hat{\rho}_{out} \hat{X}_\Phi]}{\text{Tr}[\hat{\rho}_{in} \hat{X}_\Phi]} \tag{3.37}$$

The performance of the gain with respect to the added noise is presented in Figure 3.11a.

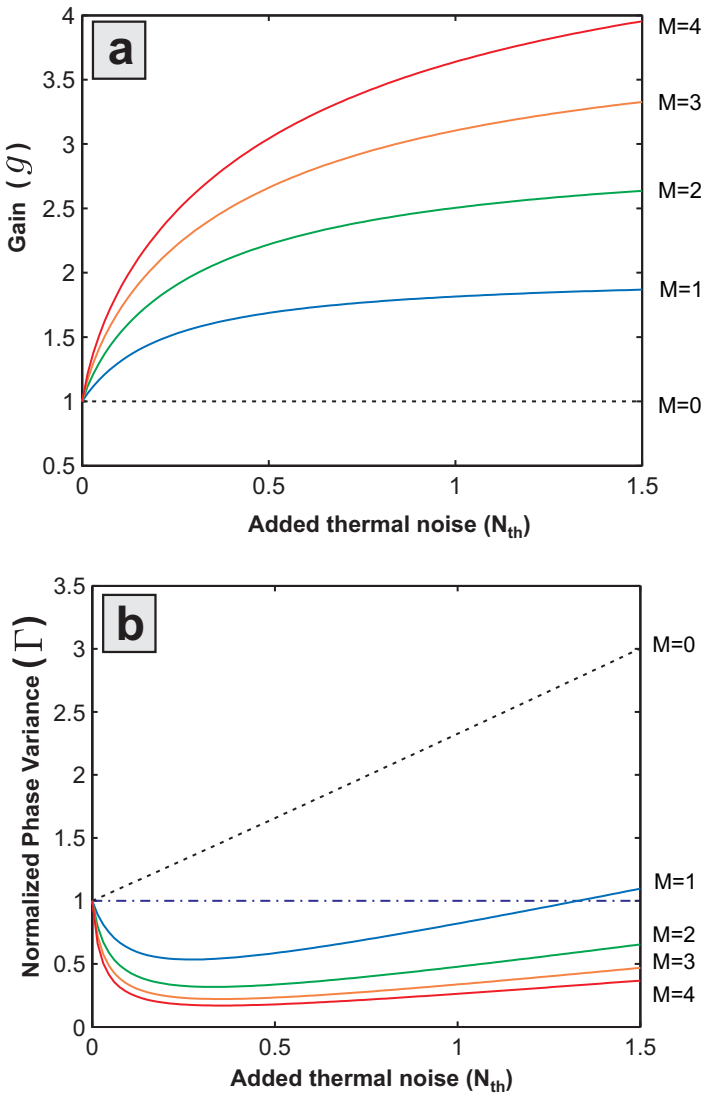

Figure 3.11: Theoretical gain and normalized phase variance vs. the mean number of added thermal photons: **a.** The gain generally grows with the number of photons in the added thermal noise and the threshold M of added thermal photons for an input coherent state of amplitude $|\alpha| = 0.48$. **b.** The canonical variance normalized to the corresponding variance of the input coherent state.

Normalized Holevo variance

The normalized Holevo variance (Γ) is given by:

$$\Gamma = \frac{V_{out}^H}{V_{in}^H} \tag{3.38}$$

where the Holevo variance[9], V^H (subsect. 2.8.1) is defined in terms of the density matrix as:

$$V^H = \left| \mathrm{Tr} \left[\sum_{n=0}^{\infty} |n\rangle\langle n+1|\hat{\rho} \right] \right|^{-2} - 1. \tag{3.39}$$

In particular, V_{in}^H can be written explicitly as [49]:

$$V_{in}^H = \left| \alpha e^{-|\alpha|^2} \sum_{n=0}^{\infty} \frac{|\alpha|^{2n}}{n!\sqrt{n+1}} \right|^{-2} - 1. \tag{3.40}$$

If we have access to the amplitude of the initial state (keeping the phase still unknown), there are still two parameters that we can use for a fine tuning of this amplifier, and these are the mean number of thermal photons N_{th} and threshold M. Fig. 3.11 shows the dependence of the gain and the phase variance on the mentioned parameters. It can clearly be seen in this figure how to choose values for N_{th} and M, depending on what quantity needs to be optimized (e.g. minimum phase variance, maximum gain, etc.).

[9]The Holevo variance of relevance in this case is the canonical, which corresponds to eq. (3.39).

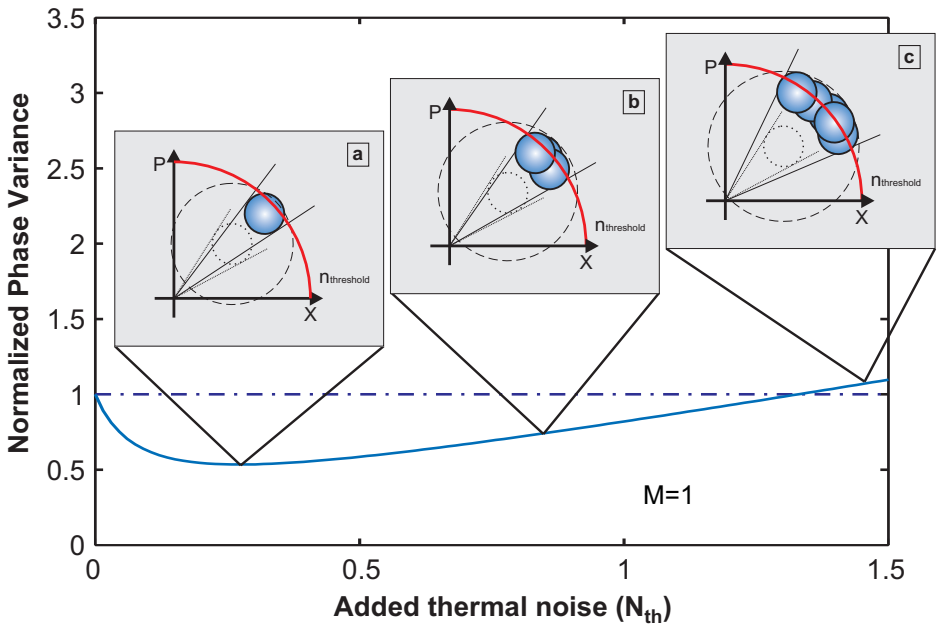

Figure 3.12: Normalized Holevo phase variance of the output state and phase space pictures associated with three different noise additions. Straight lines in the insets indicate the phase variance of the input (dotted) and the output states (solid).

In figure 3.12 we have a closer look at the effect of increasing the thermal noise. This figure is based on Fig. 3.11b in the case $M = 1$. The dashed-dotted line represents the phase variance of the input state. For reference, the input state (small dotted circle), the thermal state (dashed circle) and the remaining states after postselecting on M photons (refer to footnote #8) are plotted in the insets. As we noted before, the phase variance has a minimum for a certain amount of added Gaussian noise Fig. 3.12a. When noise is added beyond this optimal value, the dashed circle becomes larger and more states are accepted. This results in an increased phase variance in the output state (see Fig. 3.12b). Any further increase of noise after the intersection with the dashed dotted line (Γ=1), will result in a noisy phase amplification as shown in Fig.3.12c.

3.3.3 Experimental implementation

The setup is depicted in Fig. 3.13. The source is an external cavity diode laser with $\lambda = 809$nm, whose output is spatially cleaned through a single mode fiber and monitored to ensure quantum-noise-limited signal states. Subsequently the major part of the beam is split off and guided to a homodyne detector to serve as a local oscillator.

Signal preparation

The residual part of the beam is used to create the coherent signal state as well as the noise, which powers the concentration process. Both, the signal and the noise, are generated by a combination of amplitude and phase electro optical modulators (EOM) and a half wave plate (HWP). The modulators displace the signal state (S) using the orthogonally polarized auxiliary oscillator mode (AO), which is relatively bright [23]. After the modulators' calibration, we can displace the signal state to any coherent state with a maximum photon number corresponding to the mean photon number in the AO mode $n_{\max} = |\alpha_{\mathrm{AO}}|^2$. The signal mode can be chosen to be in an arbitrary mixed state, provided that the state's P-function is positive. We can therefore generate the displaced thermal state applying a suitable modulation sequence to both EOMs. The state is modeled with a finite set of (more than) 10^3 coherent states, randomly picked from a 2D normal distribution. The random modulation sequence is varied and repeated throughout the measurement. The resulting signal state resides in a polarization mode orthogonal to the input. This allows us to separate the signal from the spare part of the beam simply via a polarizing beam splitter.

Conditioning and verification

A small portion (20%) of the generated state is tapped off by an asymmetric beam splitter (corresponding to that in Fig.3.9) and guided to a fibre coupled avalanche photo diode APD, operating in an actively gated mode. The dead time of the APD (50ns) is much shorter than the pulse duration (800ns), which allows for multiple detection events.For small mean photon numbers the measured detection statistics exhibits a linear behavior, such that the APD can be used as a photon number resolving detector. The detected number of clicks in the APD is forwarded to a PC, where it is used for the heralding process. To verify the enhanced phase information of the heralded states, we perform a full tomography of the transmitted part of the state.

For this, we use a homodyne detector, which measures the signal with oscillator whose phase is varied harmonically with a by a piezoelectric transducer (PZT) to allow

for quadrature measurements at arbitrary phase angles. The scanning frequency for the PZT is chosen to be 21 mHz, leading to an effective phase drift of only 1.6 mrad within the modulation sequence. This value is negligible from an experimental point of view so that the LO's phase is considered constant within a single modulation sequence. The phase angle needed in the tomography was estimated with a series of phase calibration signals prepended to the modulation sequence. The main source of error in the setup is the drift of the modulators. To compensate for this drift, the calibration point was continuously adjusted.

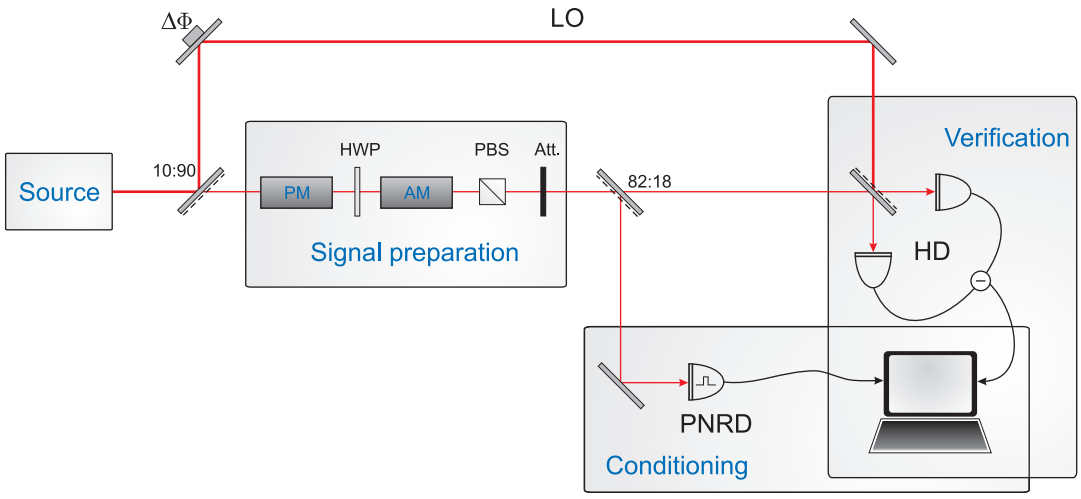

Figure 3.13: Experimental setup: A diode laser with fiber mode cleaning (FMC) acts as the source for the experiment and is split into a local oscillator (LO) and an auxiliary oscillator. The signal is prepared by a combination of two electro-optical modulators (EOM), a half-wave plate (HWP) and attenuation (Att.). A PBS removes the auxiliary oscillator. Part of the signal is tapped by a 82:18 beam splitter and coupled via a multimode fibre into the photo number resolving detector. This measurement is conditioning the output state, which is characterized by a homodyne measurement. The phase of the LO is controlled by a piezoelectric transducer (PZT).

As the homodyne detector (HD) is not a part of the phase concentration scheme itself but only implemented in the setup to prove the effect of the scheme, we do not want to take its imperfections into account in the analysis. We assume therefore perfect detection. The amplitude of the coherent input state $|\alpha|$ is then inferred from the measured mean photon number values in the imperfect PNRD and the ideal HD

$$|\alpha|^2 = |\alpha_{\mathrm{HD}}|^2 + \frac{1}{\eta_{\mathrm{PNRD}}}|\alpha_{\mathrm{PNRD}}|^2 \tag{3.41}$$

where the PNRD's quantum efficiency was calibrated to be $\eta_{\mathrm{PNRD}} = 0.63 \pm 3\%$ using the overall quantum efficiency of the HD. This procedure is preferable as it does not

demand an accurate knowledge of the input coherent states amplitude, the splitting ratio and the losses in the HD.

With the acquired tomographic data, we reconstruct the states' density matrices via a maximum likelihood algorithm [21], [22]. From the reconstructed density matrices, we calculated the Wigner functions, which are shown in Fig. 3.15. We infer the density matrix of the coherent input state by considering the attenuation of the tap measurement. The phase variance of the inferred input is then compared to the phase variances of the heralded states.

3.3.4 Results

Density matrices and Wigner functions

It is possible at this point to make comparisons between theoretical and experimental results. In order to calculate the appropriate theoretical density matrices, we use the theory presented in sec. 3.3.2, along with the parameters shown in table 3.1, which are: input coherent amplitude $|\alpha|$, mean number of added thermal photons N_{th}, transmittance T of the BS in the tap and PNRD's quantum efficiency η. The values for T and η are measured directly in the setup, and the other parameters are obtained from the tomographical result in the experiment. These parameters represent our case of study in all the analysis presented. It is imporant to notice that we use density matrices of order 9 (photon numbers from 0 to 8), where the last term $\rho_{8,8}$ is typically in the order of 10^{-7}. This contains all relevant information as will be shown below.

Table 3.1: Experimental Parameters.

$\|\alpha\|$	N_{th}	T	η
0.431	0.148	0.822	0.630

We first investigate the norm, purity and fidelity of our reconstructed data which is is presented in table 3.2. The norm of all our states is unity, $\text{Tr}[\hat{\rho}] = 1$, which confirms that they represent physical states. The purity shows that our experimental coherent is really a pure coherent state and the rest are of course mixed states and we expect $\text{Tr}[\hat{\rho}^2] < 1$. Finally the fidelity between experimental and theoretical density matrices is very good, higher than 0.98 for all cases, implying that our theoretical analysis gives an accurate representation of these states. For a visual confirmation of these

good fidelities we present the absolute value of the density matrices (theoretical and experimental), and their populations in Fig. 3.14. The colorbar has been excluded for space limitations, but the populations ($\hat{\rho}_{nn}$) give the reference for the heights. Only photon numbers from 0 to 5 are shown, althought all calculations are made with $n_{max} = 8$.

Table 3.2: Norm, purity and Fidelity for reconstructed density matrices ($n_{max} = 8$).

	Inferred coherent	Thermal	M=1	M=2	M=3
Exp. Norm	1.	1.	1.	1.	1.
Exp. purity	1.	0.7668	0.7297	0.7039	0.7127
Fidelity	0.9983	0.9974	0.9982	0.9965	0.9840

From Fig. 3.14 we can extract 3 qualitative conclusions:

1. Small coherent state

The populations show that our coherent excitation is very small, it essentially spans a 2 dim Hilbert space. This particular case even validates the assumptions for the simplest theory presented in the begining of the section with $|\alpha\rangle \simeq |0\rangle + \alpha|1\rangle$.

2. Small thermal addition

The fact that this is a weak Gaussian noise addition $N_{\text{th}} \ll 1$ is seen in the similarity of the densities for thermal and coherent states and the relatively small increase of variance for $\hat{X}$ and $\hat{P}$ quadratures in its Wigner function (Fig 3.15). Notice that this thermal state, unlike the one shown in sec. 2.6.4 (completely mixed), has coherences different from zero and its Wigner function exhibit phase features, since it has a preferred axis along that of the coherent excitation.

3. Photon subtraction effect

By looking at the progression of the states (left to right) in Fig. 3.14, we see that what really redistributes the weights in the populations (shifting to higher photon numbers) is the photon subtractions, and this progressively increases with M. The net effect we expect is gain which will be quantitatively analyzed later.

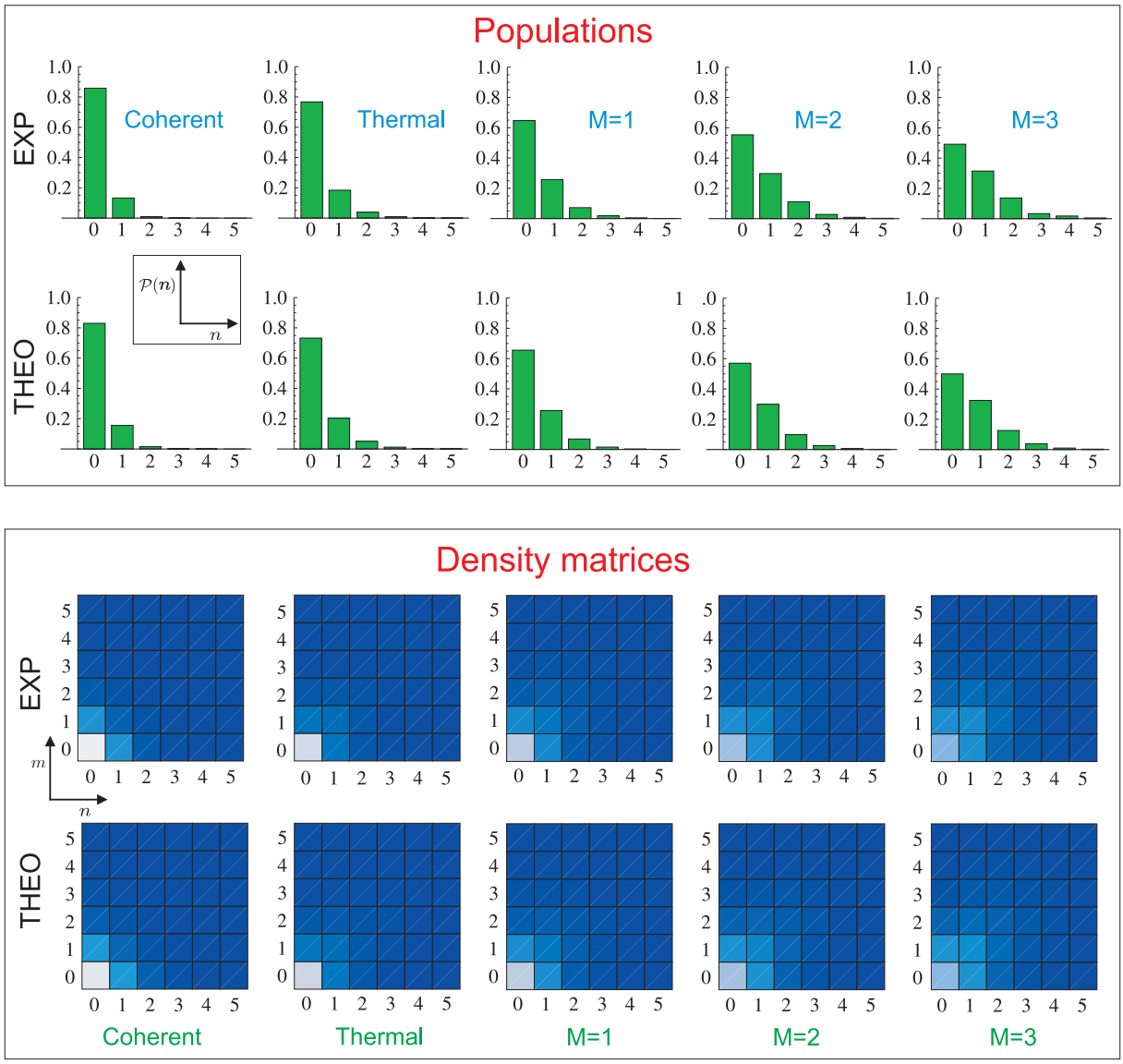

Figure 3.14: Experimental vs theoretical density matrices and populations.

Top: populations (photon number statistics).

Down: corresponding density matrices . It can be visually confirmed the high fidelity that exists between theoretical and experimental density matrices. The coherent state can be approximated to one in a 2 dim Hilbert space, the effect of photon subtraction is to shift the populations' weights to higher photon numbers, which expected effect is gain.

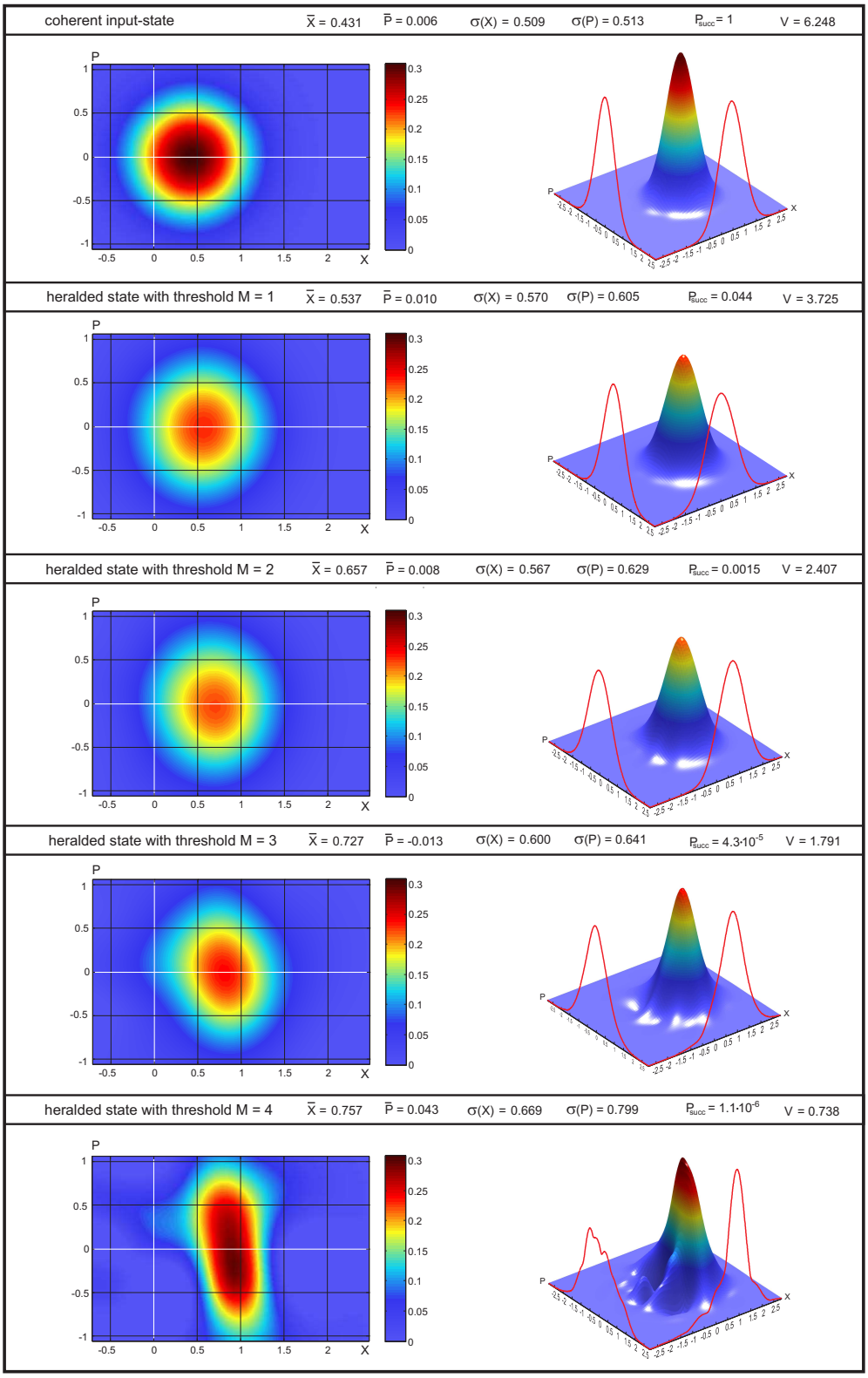

Figure 3.15: Wigner functions reconstructed from experimental data for the input state and the heralded state for different thresholds M. For each experimental reconstruction, the mean values and standard deviations for the X and P quadratures are given with the corresponding measured success probability and canonical phase variance.

phase probability density function (PDF)

We can express the phase PDF, $\mathcal{P}(\phi)$, in terms of the density matrix as:
$\mathcal{P}(\phi) = \mathrm{Tr}\left[\hat{\rho}\hat{F}(\phi)\right]$ where $\hat{F}(\phi)$ is a POVM defined in subsect. 2.8.

Fig. 3.16 shows the phase probability distribution function (PDF) derived from the experimental data (dashed lines) for the measured coherent, the thermal and the conditioned states. Corresponding theoretical functions (solid lines) were calculated for states fitting to experimentally derived parameters.

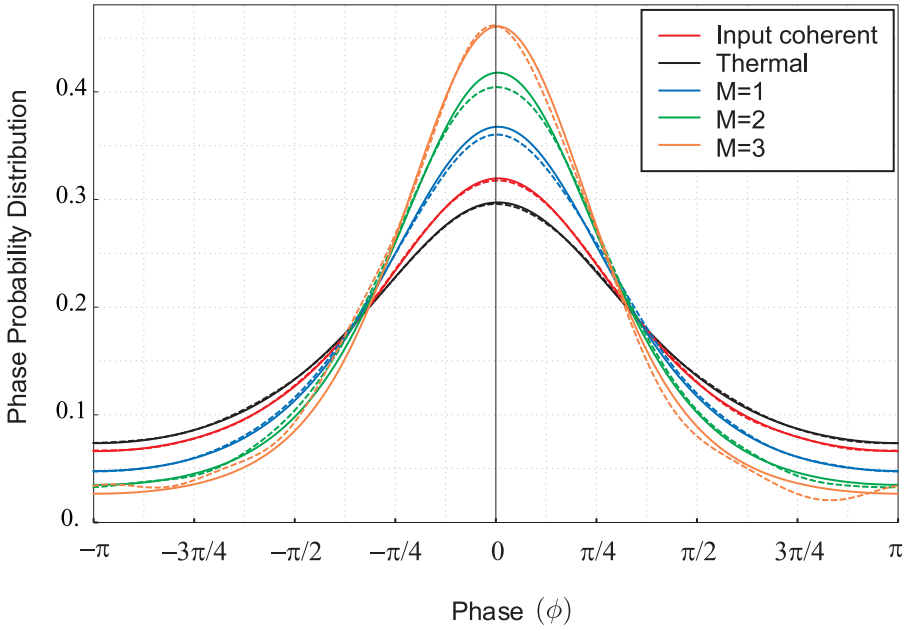

Figure 3.16: Phase probability distribution function comparison between experimental data (dashed lines) and theoretical calculations (solid lines) for different states.

Very good agreement between theory and experiment is achieved. The effect of the amplifier on the phase variance is clear: by increasing the threshold, the output state's phase PDF gets more and more concentrated as the peak of the distribution clearly rises, this implies that the phase variance is reduced.

Holevo phase variance

To calculate explicitly the reduction in phase variance, we can use the expression already mentioned in (3.39), both for experimental data and theoretical calculations.

Fig. 3.17 shows the comparison in phase variance between the experimental data (light blue) and corresponding theoretical values (dark blue) calculated for states fitting to the experimentally derived parameters. The inferred input coherent state serves as the reference value, and is shown as a red dashed line, calculated from expression (3.40). The error bars represent the statistical deviations over many different realizations of the experiment. It is important to notice here, that any bar lying below the red line represents a successful realization of noiseless amplification, and we conclude that phase variance reduction appear only after the conditioning on M.

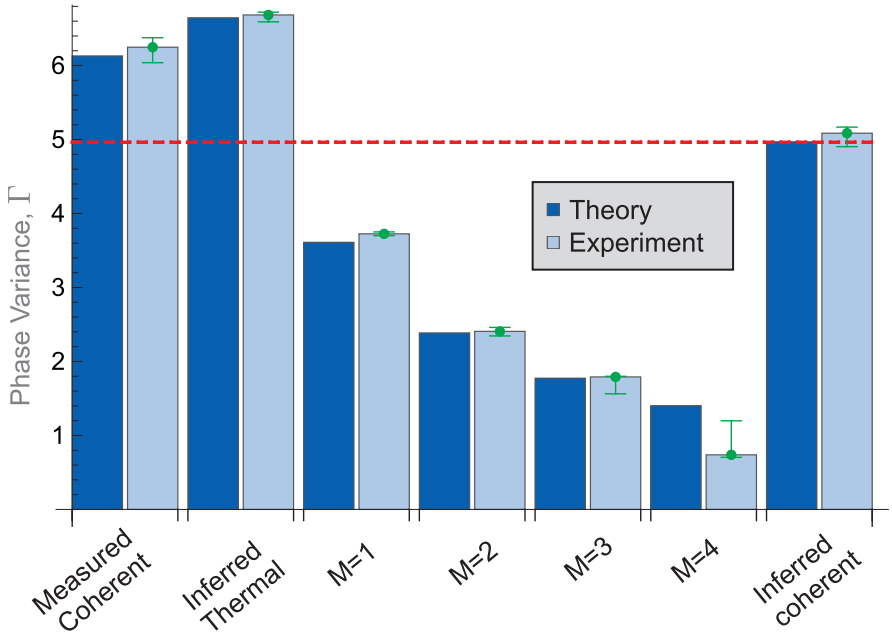

Figure 3.17: Theoretical and experimental phase variances for an input coherent state with amplitude $|\alpha| = 0.431$ are shown for varying threshold parameter M. A clear reduction of the phase variance is already achieved for the subtraction of a single photon.

Gain (g)

A comparison for the gain is shown as calculated from expression 3.42:

$$g = \frac{\mathrm{Tr}[\hat{\rho}_{out}\hat{X}_{\Phi}]}{\mathrm{Tr}[\hat{\rho}_{in}\hat{X}_{\Phi}]}$$

The figure clearly shows a progressive increase in amplification gain with increasing threshold M, which show us that unlike the other probabilistic amplifiers shown before, this allow us to choose from different gains by selecting an appropriate threshold.

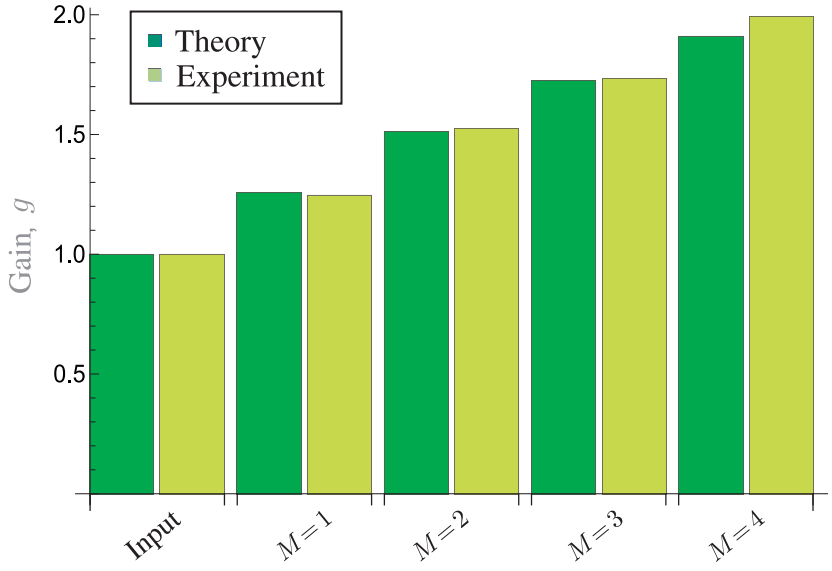

Figure 3.18: Amplifier's gain for different thresholds M.

It is important to notice that the noise addition process does not have any effect on the amplification gain because the mean value of the resulting distribution in phase space is centered in the same place, so the amplification really happens due to the photon subtraction. This is a confirmation of the qualitative analysis from the populations in Fig. 3.14. We saw there that the effect of conditioning was to shift the populations' weights to higher photon numbers which effect is gain.

Success Probability ($\mathcal{P}_{suc}$)

Finally, the cost of decreasing the phase variance on a probabilistic quantum amplifier is a lower success rate. This is perhaps the biggest limitation of this amplifier but it is a fair price to pay remembering that it is impossible to noiselessly and deterministically amplifiy a quantum state. The figure below presents the decrease of success rate with increasing M, so the better the amplifier performs (higher gain and lower phase variance), the less frequent it happens.

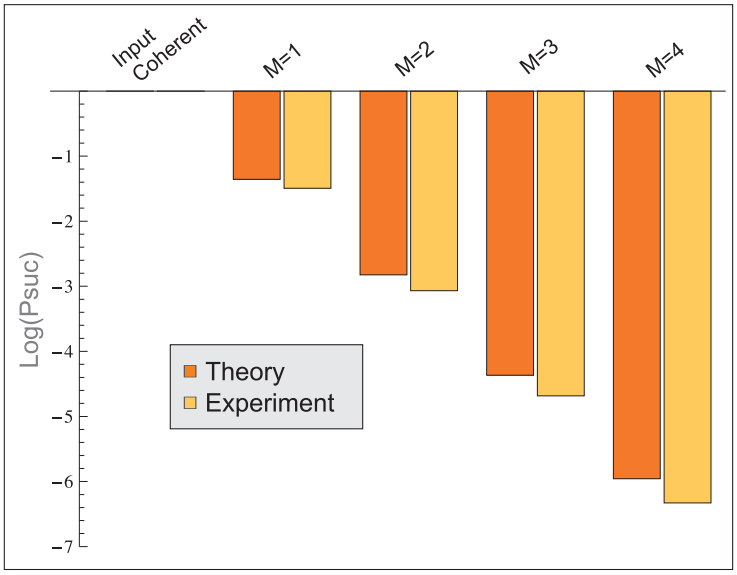

Figure 3.19: Success Probability $\mathcal{P}_{suc}$ for the different states considered.

Final remarks

To optimize the performance of the amplifier - that is, to minimize the phase variance - the amount of added thermal noise should be chosen appropriately with respect to the input coherent state amplitude. Furthermore, we note that having detailed information about the input alphabet, the structure of the noisy displacements can be tailored accordingly, thereby drastically reducing the amount of energy used to drive the amplifier. For example if the input is a phase-covariant coherent state alphabet, the optimized structure of the noisy displacement is also phase covariant. Such tailoring of the displacements as well as applications of the amplifier will be interesting directions for future research. Finally, we note that the noise addition process can be also carried out with a linear amplifier. Such an approach will not

only add thermal noise to the input state but will also displace it coherently in the preferred direction, thereby further concentrating the phase information.

A further improvement can be done by inserting several of these amplifiers in parallel in a multi-path interferometer, in a similar way as it was suggested for the scissors approach [7]. In this way it is in principle possible to noiselessly amplify an arbitrary coherent state.

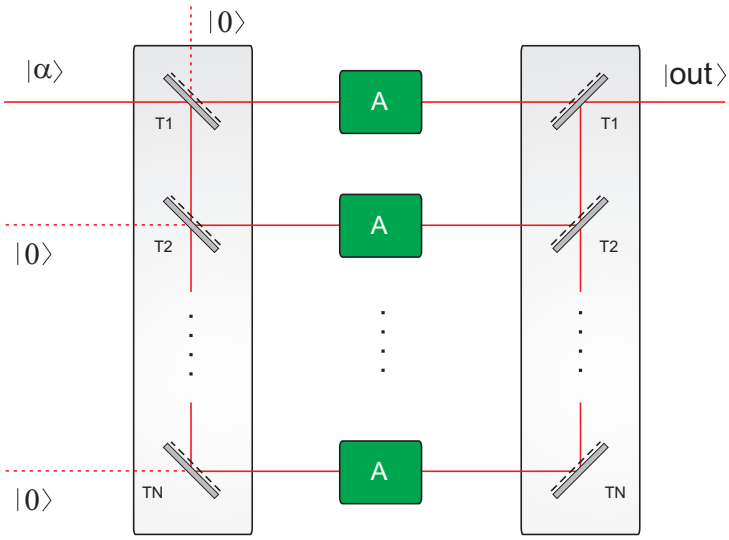

Figure 3.20: Noiseless amplification of an arbitrary coherent state. Several amplifiers can run in parallel upon an initial spliting in an array of beam splitters. The amplified states are later recombined to form the output state.

3.3.5 Conclusion

We have presented a device that reduces the phase uncertainty of an input coherent state of light through noiseless probabilistic amplification. In contrast to previous approaches to noisefree amplification, the amplifier is neither based on an ample supply of nonclassical resources nor on strong parametric interactions, but solely on Gaussian noise addition and photon counting. Due to its pivotal properties such as simplicity and robustness, it is expected that this approach to probabilistic noisefree amplification will be of interest to a large variety of experiments and protocols involving phase estimation such as quantum metrology and quantum communication.

Chapter 4

Adaptive Single Shot Phase Estimation

Contents

4.1 Introduction

Optical Phase is a topic of great importance both, in classical and quantum optics, as it is an essential component in many different applications. For instance, it is used to transmit information and it also plays an important role in metrology. Interestingly, the absolute phase ϕ[1] cannot be measured (not even classically), as it lacks a meaning before we relate it to a known reference, so what we could in principle measure is a phase difference $\Delta\phi$[1]. In metrology, by choosing a proper transducer, one can

[1] to simplify the notation, we will use ϕ in the rest of the chapter to denote a phase difference.

relate a phase difference to a physical quantity of interest. The canonical example is an interferometer, where fringe position (phase difference) can be mapped into a measurement of length, frequency, temperature, displacement, etc.

Unfortunately, this phase difference cannot be measured directly by currently available detectors (sometimes called square module detectors), as they are only sensible to electric field intensity[2] $I \sim |E|^2$. The common solution to resolve the phase is to interfere the signal of interest with a reference beam, typically called the local oscillator (LO), producing intensity modulations $I(\phi)$ that can be registered by our detectors. Figure 4.1 illustrates this process of measuring a physical quantity λ through the use of optical phase. A transducer maps the physical quantity of interest λ, into the phase of an optical field that is then mixed with an LO and detected. The phase is inferred from the recorded intensity and the value of λ can be finally recovered. A typical example of such a transducer is a mirror mounted on a piezoelectric actuator, which by changing the optical path length changes the phase of the beam and produces a phase-dependent-displacement: $\phi = \phi(d)$.

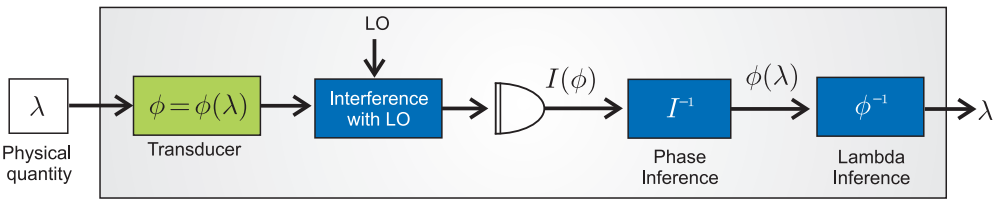

Figure 4.1: Phase Metrology.

If one wants to go further and try to reach the precision limits, a Quantum mechanical description of the problem is required. This complicates the picture of phase metrology in Fig.4.1, as it imposes limits on how well we can measure incompatible operators (through Heisenberg uncertainty relations), and in some sense[3], optical intensity (proportional to photon number) and phase are incompatible. So by resorting to an intensity measurement, we are fundamentally limited in the determination of the phase. It is then worth finding an observable for the phase, no matter how complicated it is to construct in practice, as it would allow for a direct phase measurement and eventually reach the ultimte precision limits. The quest for a phase observable is the subject of the next section.

[2] another reason is that optical frequencies are extremely fast to be detected ($f \sim 10^{14}$Hz).
[3] this point will be discussed later.

On the Hermitian phase operator.

4.1.0.1 Observables

In Quantum mechanics, if a physical quantity can be measured in practice, it needs to have a counterpart in the theory in the form of a Hermitian operator. The result of a measurement is therefore, a real number as the eigenvalues of a Hermitian operator are real. So, as the annihilation operator:

$$\langle\alpha|\hat{a}|\alpha\rangle = \alpha \tag{4.1}$$

gives complex amplitudes of the field, it is clearly not Hermitian. It is however possible to construct Hermitian operators as combinations of $\hat{a}$ and $\hat{a}^\dagger$; $\hat{X} = (\hat{a} + \hat{a}^\dagger)/2$ and $\hat{P} = i\left(\hat{a}^\dagger - \hat{a}\right)/2$, known as quadrature operators with expectation values (for a coherent state):

$$\langle\alpha|\hat{X}|\alpha\rangle = |\alpha|\cos(\phi) = \mathrm{Re}\{\alpha\} \tag{4.2}$$

$$\langle\alpha|\hat{P}|\alpha\rangle = |\alpha|\sin(\phi) = \mathrm{Im}\{\alpha\} \tag{4.3}$$

as shown in last column in Table 2.1. Quadrature operators are therefore observables, and they correspond to the real and imaginary parts of the electric field. Moreover, the simultaneous measurement of the two conjugate quadratures can give phase information but this kind of measurement is not optimal with respect to a phase measurement (Fig. 4.2). Let us study different approaches to define a proper Hermitian phase operator.

4.1.0.2 Dirac approach

Dirac [11] proposed a phase operator $\hat{\phi}$ in terms of a polar decomposition of creation and annihilation operators:

$$\hat{a} = e^{i\hat{\phi}}\sqrt{\hat{n}} \tag{4.4}$$

$$\hat{a}^\dagger = \sqrt{\hat{n}}e^{-i\hat{\phi}} \tag{4.5}$$

which seems natural as $\sqrt{\hat{n}}$ would represent the amplitude and $\hat{\phi}$ the phase of the electric field. Now by imposing the bosonic commutation relation $\left[\hat{a}, \hat{a}^\dagger\right] = 1$, we get:

$$e^{i\hat{\phi}}\hat{n}e^{-i\hat{\phi}} - \hat{n} = 1 \tag{4.6}$$

where we have explicitly assumed $\hat{\phi}$ to be Hermitian. We can evaluate this expression with the aid of the Baker-Campbell-Hausdorff (BCH) formula **??**, and we get:

$$\hat{n} + [i\hat{\phi}, \hat{n}] + \frac{1}{2!}[i\hat{\phi}, [i\hat{\phi}, \hat{n}]] \cdots - \hat{n} = 1 \tag{4.7}$$

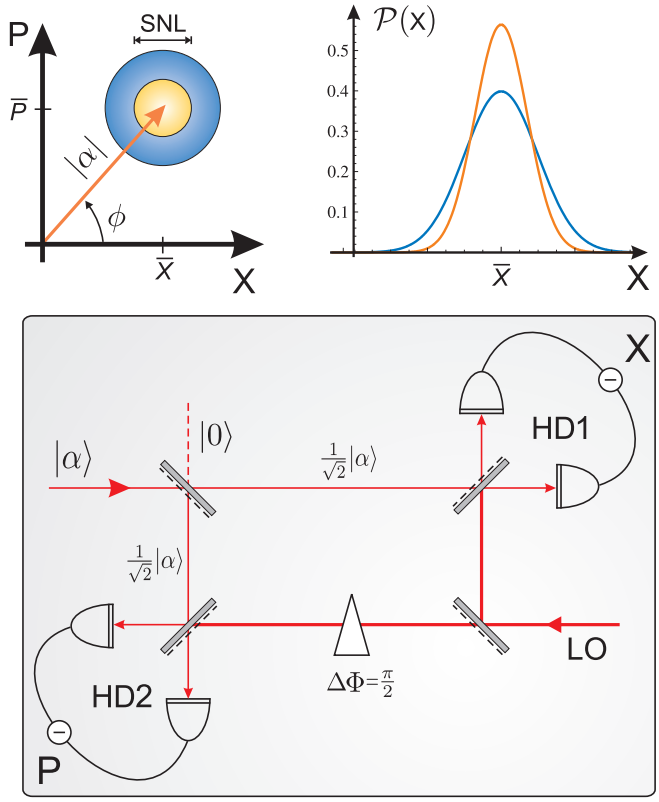

Figure 4.2: Simultaneous measurement of conjugate quadratures. The state is divided on a 50:50 BS and sent to two independent homodyne detection stages whose local oscillators' phases are shifted by $\pi/2$. An effect of this measurement is to have extra noise as illustrated in phase space. **Top left:** Wigner distribution (yellow) and measured distribution (blue), **Top right:** corresponding marginals. A phase estimate can be obtained by $\tilde{\phi} = \arctan(P/X)$ which has the correct mean value but higher variance.

To satisfy the condition 4.7 it is enough to impose:

$$[\hat{n}, \hat{\phi}] = i \tag{4.8}$$

The commutator 4.8 becomes the condition for this phase operator to be Hermitian. This commutator has a nice form that allow us to think of $\hat{n}$ and $\hat{\phi}$ as canonically conjugated quantities, and we can now express their Heisenberg relation by using eqs 2.4 and 2.5:

$$\Delta\hat{\phi}\Delta\hat{n} \geq \frac{1}{2} \tag{4.9}$$

Let us analyze this result. The spectrum of the operator $\hat{\phi}$ is continuous and periodic, $\phi \in [0, 2\pi)$, while the spectrum of $\hat{n}$ is discrete and bounded from below $n \in \{0, 1, 2, \ldots, \infty\}$. We can see that this relation is problematic because the maximum uncertainty for the phase is $\Delta\hat{\phi}_{max} = 2\pi$, which imposes a limit for the uncertainty in the photon number $\Delta\hat{n} \geq \frac{1}{4\pi}$ but this does not seem to be justified[4]. Moreover, if we evaluate eq. 4.8 with fock states $|n\rangle, |m\rangle$, we obtain:

$$\langle n| \left[\hat{n}, \hat{\phi}\right] |m\rangle = i\langle n|m\rangle \tag{4.10}$$

$$\langle n|\hat{n}\hat{\phi}|m\rangle - \langle n|\hat{\phi}\hat{n}|m\rangle = i\delta_{nm} \tag{4.11}$$

$$(n-m)\langle n|\hat{\phi}|m\rangle = i\delta_{nm} \tag{4.12}$$

which leads to the absurd result $0 = i$, and we can conclude that a Hermitian phase operator (if it exists) cannot be written in the form 4.4.

4.1.0.3 Susskind-Glogower phase operator

Another approach was followed by Susskind and Glogower [67], where they proposed an exponential (SG) phase operator:

$$\widehat{\exp}(i\phi) \equiv (\hat{n}+1)^{-1/2}\hat{a} = (\hat{a}\hat{a}^\dagger)^{-1/2}\hat{a} \tag{4.13}$$

$$\widehat{\exp}(i\phi)^\dagger = \hat{a}^\dagger(\hat{n}+1)^{-1/2} = \hat{a}^\dagger(\hat{a}\hat{a}^\dagger)^{-1/2} \tag{4.14}$$

which can be written in terms of Fock states:

$$\widehat{\exp}(i\phi) = \sum_{n=0}^{\infty} |n\rangle\langle n+1| \tag{4.15}$$

$$\widehat{\exp}(i\phi)^\dagger = \sum_{n=0}^{\infty} |n+1\rangle\langle n| \tag{4.16}$$

[4]for example, any Fock state $|n\rangle$ will have $\Delta\hat{n} = 0$. Notice, however, that it is plausible for coherent states with large amplitude.

This definition of the phase exponential operator seems right, since it can be shown that its eigenstates are the well known phase states $|\phi\rangle$:

$$|\phi\rangle = \sum_{n=0}^{\infty} e^{in\phi}|n\rangle, \tag{4.17}$$

furthermore, its eigenvalues are complex exponentials of ϕ as :

$$\widehat{\exp}(i\phi)|\phi\rangle = e^{i\phi}|\phi\rangle. \tag{4.18}$$

Unitarity is the condition for this exponential operator, which is equivalent of Hermiticity on a phase operator. Let us check this:

$$\widehat{\exp}(i\phi)^{\dagger}\widehat{\exp}(i\phi) = \mathbb{1} \tag{4.19}$$

$$\widehat{\exp}(i\phi)\widehat{\exp}(i\phi)^{\dagger} = \mathbb{1} - |0\rangle\langle 0| \tag{4.20}$$

and we find that $\widehat{\exp}(i\phi)$ is not unitary due to the extra term $|0\rangle\langle 0|$.

4.1.0.4 Other approaches

Other approaches to find a Hermitian phase operator have been tried, but all of them have difficulties. One successful definition that avoids the mathematical complications has to do with extending the Fock space to negative photon numbers [66]:

$$\widehat{\exp}(i\phi) = \sum_{n=-\infty}^{\infty} |n\rangle\langle n+1| \tag{4.21}$$

$$\widehat{\exp}(i\phi)^{\dagger} = \sum_{n=-\infty}^{\infty} |n+1\rangle\langle n| \tag{4.22}$$

With this definition we find that the operator is unitary:

$$\widehat{\exp}(i\phi)^{\dagger}\widehat{\exp}(i\phi) = \mathbb{1} = \widehat{\exp}(i\phi)\widehat{\exp}(i\phi)^{\dagger} \tag{4.23}$$

The problem with this last operator is in the physics rather than in the mathematics, as negative Fock states are unphysical. We can at this point look for alternatives to avoid the difficulties of a phase observable, which is discussed in the next section.

It is important to notice that the problems shown above do not prevent us from using phase states $|\phi\rangle$ as defined in eq. 2.76. They are complete:

$$\frac{1}{2\pi}\int_0^{2\pi} d\phi|\phi\rangle\langle\phi| = 1$$

and we can still use them to evaluate the phase probability distribution of a given state $\hat{\rho}$:

$$\mathcal{P}(\phi) = \frac{1}{2\pi}\langle\phi|\hat{\rho}|\phi\rangle$$

4.1.1 Measurement vs Estimation

The difficulties previously presented in defining a Hermitian phase operator can be avoided if we reformulate the problem of obtaining the value of the phase of an optical state. Instead of thinking of the phase as a physical measurable quantity, one can think of it as parameter of a certain operator that needs to be estimated. Here we will use the phase-shift operator which depends parametrically on ϕ:

$$\hat{U}(\phi) = \exp(i\phi\hat{n}) \tag{4.24}$$

We can think of the phase of a given state $\hat{\rho}_\phi$, as a phase shift ϕ imposed on an initial state $\hat{\rho}_0$:

$$\hat{\rho}_\phi = \hat{U}(\phi)\hat{\rho}_0\hat{U}^\dagger(\phi) \tag{4.25}$$

this can be seen as the state preparation stage[5] as shown in Fig.4.3, and since this preparation is inaccessible to us, the phase ϕ is unknown. To estimate the parameter

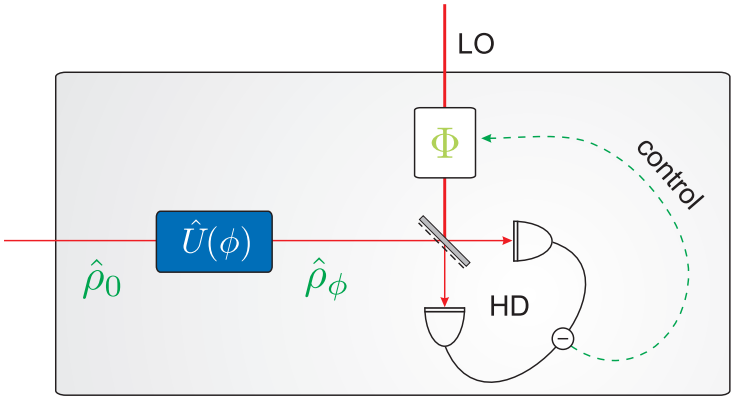

Figure 4.3: Phase estimation scheme. The state $\hat{\rho}_\phi$ is prepared by phase shifting the initial $\hat{\rho}_0$, where ϕ is an unknown parameter representing the phase shift. Phase estimation is done by performing homodyne detection and controlling the local oscillator phase Φ.

ϕ, one needs to relate it to an actual measurement. Here we chose homodyne detection as it is experimentally accessible (represented by the quadrature observable) and because the measurement outcome depend on the unknown phase ϕ of the state. Such a measurement also depends on the phase Φ of the local oscillator that serves as a reference. In this case we have total control over Φ and we will use this ability in order to estimate ϕ. The precise form of the control we will use is discussed later

[5]this can be an actual state preparation made by a sender in a communication channel or the effect of a transducer in a metrological setup as discussed before (Fig.4.1).

in section ??. The remainder of this section gives some useful definitions related to the phase estimation problem.

4.1.2 Phase estimation classification

Ab initio phase estimation vs Phase sensing

Phase estimation presents two scenarios regarding the initial knowledge that we have about the phase. One of them is when we have some a priori information; perhaps we know that the phase lies in a small range and what we want is to reduce this uncertainty and obtain a value with a higher precision. We call this case *phase sensing*. The other possibility is when the value of the phase is absolutely undetermined, and we have no way of guessing its value before the measurement is performed. This case is known as *Ab initio phase estimation*.

Single shot vs Repeated measurements

Single shot measurement does not necessarily mean a single measurement. In fact one could have several (partial) measurements inside the duration of the pulse that define the state or even a continuous measurement record as in Fig. 4.4. The term single shot refers to the measurement of a *single copy* of the system. It is also possible (and normally easier) to perform phase estimation with several copies of the system, it is the case of HD tomography [21], Bayesian phase estimation [57], etc.

Adaptive vs Non-adaptive

In homodyne detection, we have complete control over the local oscillator's phase, Φ. For phase estimation, we can change Φ in real time as a function of the HD photocurrent as suggested by Fig. 4.3. In such a case the measurement can be progresively *Adapted* to optimize the measurement of the state. It is also possible to drive Φ independently on the HD. This case is known as *Non-adaptive measurement* and is similar to open loop control [77].

Table 4.1: Phase estimation classification. Different phase estimation strategies that will be discussed in this chapter are classified according to the previously presented criteria.

Class	**Adapt.**	**No-Ad.**	**Sensing**	**Ab init.**	**1 shot.**	**Repeat.**
Mark I, II	X			X	X	
Heterodyne		X		X	X	X
HD Tomography		X		X		X
Bayes	X	X	X			X

4.2 Semiclassical theory

The traditional treatment in quantum optics of quadratures and homodyne detection as given in sections 2.2 and 2.3 is usually sufficient to discuss fixed quadrature measurements, but it is not enough to account for time dependent situations. Since we are interested in real time feedback schemes, we will need to extend the theory given there. In this section we describe a semiclassical theory for time dependent homodyne measurements, and we start by writing the single mode electric field:

$$E(t) = \left(\frac{2\hbar\omega u(t)}{\epsilon_0 V}\right)^{1/2} \mathrm{Re}\left\{\alpha e^{-i\omega t}\right\}, \tag{4.26}$$

where $u(t)$ is a real valued temporal mode function and α is the field's complex amplitude. The power of such a field is $P = \epsilon_0 V \langle E^2(t)\rangle$, where $\langle E^2(t)\rangle$ is an average over many cycles. We can write the rate of photoelectron production as:

$$\lambda(t) = \frac{\epsilon_0 V \langle E^2(t)\rangle}{\hbar\omega} = \frac{|\alpha|^2}{\tau}, \tag{4.27}$$

which represents the electrons produced in a detector corresponding to the average number of incoming photons ($|\alpha|^2$) per time τ[6]: the photon flux of the signal beam.

4.2.0.1 Local oscillator (LO)

In order to maximize the visibility of the interference between the signal beam and the LO as required in homodyne detection, it is important to use a local oscillator as

[6]In this chapter, we denote by τ the duration of the state, which also corresponds to the duration of a single shot measurement.

similar as possible to the signal beam. We then assume for the LO, the same mode function $u(t)$

$$E_{LO}(t) = \left(\frac{2\hbar\omega u(t)}{\epsilon_0 V}\right)^{1/2} \beta \mathrm{Re}\left\{e^{-i\omega t + i\Phi(t)}\right\}, \tag{4.28}$$

where the LO amplitude β is real and its phase $\Phi(t)$ is slow[7].
We can write the rate of photoelectron production on each detector in the HD due to the interference:

$$\lambda_\pm(t) = \frac{1}{2}|\alpha \pm \beta e^{i\Phi(t)}|^2 u(t)$$

As usual we require $\beta \gg |\alpha|$. If we take a homogeneous pulse with temporal duration τ, we find:

$$\lambda_\pm(t) = \frac{1}{2}\frac{|\alpha \pm \beta e^{i\Phi}|^2}{\tau} \tag{4.29}$$

Let us now consider the interval $[t, t+\delta t)$ where δt is small compared to the lenght of the pulse, τ, but longer than the mean time between photodetections:

$$\frac{\tau}{\beta^2} < \delta t < \tau \tag{4.30}$$

We can consider the number of photodetections to follow a Poisson distribution [70] with mean $\lambda_\pm \delta t$:

$$\mathcal{P}(n) = e^{-\lambda_\pm \delta t}\frac{(\lambda_\pm \delta t)^n}{n!} \tag{4.31}$$

We know that the amplitude of LO, β, is large so we expect several photodetections in $[t, t+\delta t)$, in that is: $\lambda_\pm \cdot \delta t > 1$. In this case, one can approximate the poisson $n \sim Poisson(\lambda_\pm \delta t)$ to a Gaussian distribution $n \sim N(\mu = \lambda_\pm \delta t, \sigma = \sqrt{\lambda_\pm \delta t})$, and the number of photodetections in the interval $[t, t+\delta t)$, for each detector will be:

$$\delta n_\pm(t) = \lambda_\pm(t)\delta t + \sqrt{\lambda_\pm(t)}\delta W_\pm(t) \tag{4.32}$$

Here the last term represents white noise with variance $\lambda(t)\delta t$. We can rewrite this expression in terms of known quantities:

$$\delta n_\pm(t) = \frac{|\alpha \pm \beta e^{i\Phi}|^2}{2\tau}\delta t + \frac{|\alpha \pm \beta e^{i\Phi}|}{\sqrt{2\tau}}\delta W_\pm(t). \tag{4.33}$$

To obtain an expression for the time dependent homodyne detection photocurrent, we need to evaluate the following limits for the photodetection difference:

$$I(t) = \lim_{\delta t \to 0}\lim_{\beta \to \infty}\frac{\delta n_+(t) - \delta n_-(t)}{\beta \delta t} \tag{4.34}$$

[7] In what follows, this condition is always fulfilled as at optical frequencies $\omega \sim 10^{14}$Hz and in our case $t \lesssim s.$ compared to ωt

the result is conveniently expressed as:

$$I(t)dt = \frac{4|\alpha|}{\tau}\cos[\Phi(t) - \phi]dt + \frac{dW(t)}{\sqrt{\tau}}. \tag{4.35}$$

which gives the time dependent stochastic [41, 42] variation of the photocurrent in homodyne detection. Eq.(4.35) is the simplest expression that captures all the details we are interested in: First, it changes continuously in time and gives the explicit dependence of each quantity on time. Second, it implies that the photocurrent mean value is proportional to a quadrature measurement, in fact, if we allowed $\Phi(t)$ to vary, it would correspond to the rotated quadrature: $\hat{X}_{\Phi(t)}$. Finally we notice that the noise dW is additive and Gaussian, as it should be for a coherent state.

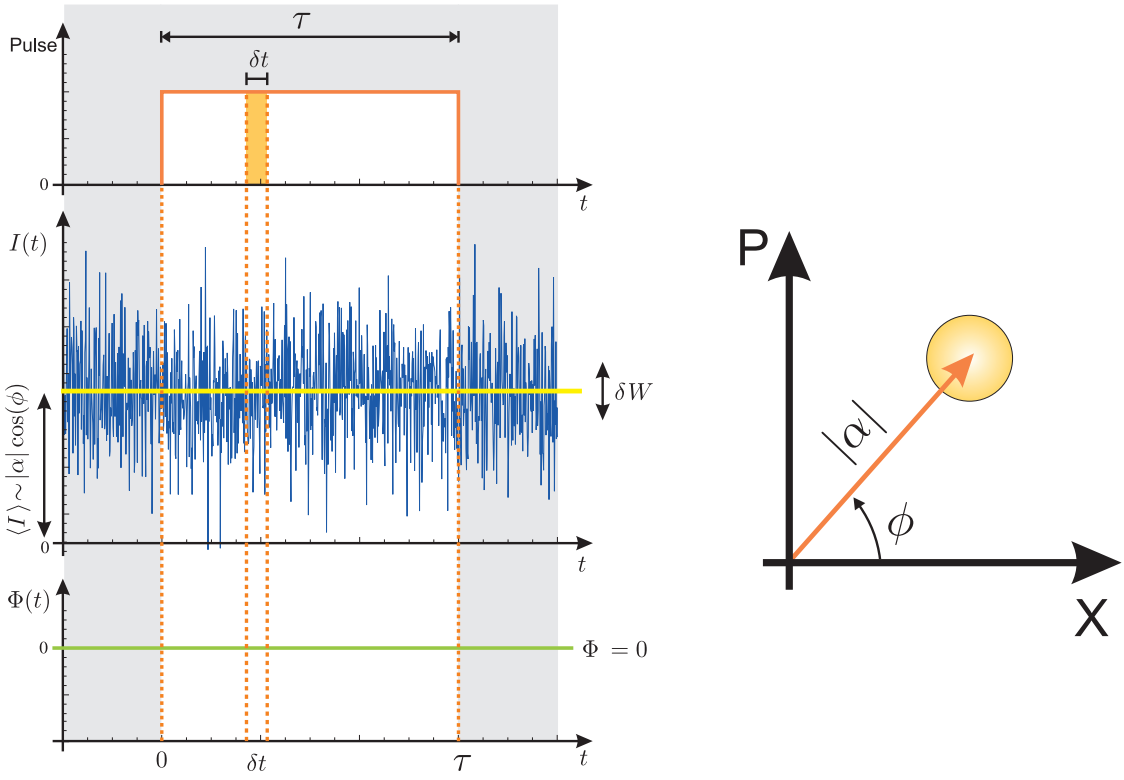

Figure 4.4: **Single shot homodyne measurement:** A single copy of the state defined in $[0, \tau)$ is measured. **Left:** Pulse shape and duration, stochastic variation of the HD photocurrent and LO phase are shown. The mean photocurrent $\langle I \rangle$ is proportional to the quadrature $\hat{X}$, and it is constant in this case since $|\alpha|, \phi$, and Φ are all constant in time. **Right:** Corresponding Phase space picture of the state $|\alpha\rangle = ||\alpha|e^{i\phi}\rangle$. A single shot measurement corresponds to a single point on that distribution.

Figure 4.4 illustrates the case of photocurrent recording in a static situation (Φ=0). The temporal mode of our state (and LO) is constant and defined in a time interval $\Delta t = \tau$, which gives the temporal extent of the state and therefore, the measurement time for a single shot. This is the type of outcome that one would expect in the lab by locking the phase of the state and LO without imposing any other control over the phase Φ. In section ?? we analyze an estimation strategy where an active control of Φ is needed.

4.3 Quantum theory

The results shown in the previous semiclassical derivation seem correct, as it successfully models the basic characteristics observed experimentally. By quantizing the field, we will find essentially the same result:

$$I(t) = \lim_{\delta t \to 0} \lim_{|\beta| \to 0} \frac{\delta \hat{n}_1(t) - \delta \hat{n}_2(t)}{|\beta|\, \delta t} \tag{4.36}$$

$$\sim \left\langle \hat{a} e^{-i\Phi(t)} + \hat{a}^\dagger e^{i\Phi(t)} \right\rangle + \xi(t) \tag{4.37}$$

But we could go further and use this result for the photocurrent (which is essentially a classical quantity), to describe what happens to the state in the course of a measurement and for this we need to use quantum measurement theory.

We will now focus on the way to extract relevant information about the measured quantum states through the measurement record $\mathbf{I}_{[0,t)}$ corresponding to the HD photocurrent in the interval $[0, t)$. We can express the probability of obtaining $\mathbf{I}_{[0,t)}$, given the state $\hat{\rho}$ and the local oscillator history $\Phi_{[0,t)}$ as:

$$\mathcal{P}\left(\mathbf{I}_{[0,t)} | \hat{\rho}, \Phi_{[0,t)}\right) = \mathrm{Tr}[\hat{\rho} \hat{F}_t] \tag{4.38}$$

where $\hat{F}_t$ is then, the positive operator-valued measure POVM for $\mathbf{I}_{[0,t)}$ (parametrized by the continuous variable t). Wiseman [85] has evaluated this POVM as:

$$\hat{F}_t = \hat{F}(A_t, B_t) \tag{4.39}$$

$$= \mathcal{P}_0(A_t, B_t) \hat{G}_t(A_t, B_t). \tag{4.40}$$

where $\mathcal{P}_0(A_t, B_t)$ is an ostensible PDF [85] and G_t is a positive operator given by:

$$\hat{G}_t(A_t, B_t) = \exp\left(\frac{1}{2} B_t \hat{a}^{\dagger 2} + A_t \hat{a}^\dagger\right) \cdot \exp\left(-\hat{a}^\dagger \hat{a} t\right) \cdot \exp\left(\frac{1}{2} B_t^* \hat{a}^2 + A_t^* \hat{a}\right). \tag{4.41}$$

A_t and B_t are functionals of $\mathbf{I}_{[0,t)}$, they are explicitly given by:

$$A_t = A_t[\mathbf{I}_{[0,t)}] = \int_0^t e^{i\Phi(s)} e^{-s/2} I(s)\, ds, \tag{4.42}$$

$$B_t = B_t[\mathbf{I}_{[0,t)}] = -\int_0^t e^{i2\Phi(s)} e^{-s}\, ds \tag{4.43}$$

and contain all the useful information about the measurement, in fact this result for $\hat{F}_t$ is very general and can be applied to different cases of photodetection in the large LO limit. In particular, $\hat{F}_t$ can describe the effect of the feedback loops, and we will use it to estimate the phase of an input quantum state.

4.4 Feedback

We already showed the case of heterodyne detection, which is a technique to simultaneously measure both quadratures $\hat{X}$ and $\hat{P}$ and thus to estimate the phase of the input field with the problem of having extra noise. The origin of that noise is precisely the effect of the simultaneous measurement of non commuting operators, obeying Heisenberg's uncertainty principle (sec. 2.1.1).

Homodyne detection would be a better choice as one is measuring only one quadrature, but to estimate the phase correctly one normally needs repeated measurements at different phases, as in the bayesian estimation or in quantum tomography.

We want instead to use HD for the estimation of the phase in a single shot. The idea will be to adaptively control the phase of the LO,$\Phi(t)$, based on a partial estimate $\tilde{\phi}(t)$, in such a way that at the end of the measurement, the LO is orthogonal to the initially unknown signal in phase space. To this end we just need to impose the following condition onto the LO:

$$\Phi(t) = \tilde{\phi}(t) + \pi/2 \tag{4.44}$$

We will follow the proposal of Wiseman to calculate the partial and final estimates, which are based on the A_v and B_v coefficients mentioned earlier.

During the course of the single shot we will do a realtime feedback with the partial estimate given by:

$$\tilde{\phi}(t) = \int_0^t \frac{I(t)}{\sqrt{t}}\, dt \tag{4.45}$$

and for the final estimates, we have two posibilities:

1. Mark I: consists of just taking the estimate at time $t = \tau$, which of course depends on the whole photocurrent history. This corresponds to $\tilde{\phi}_I = arg A_\tau$

2. Mark II: corresponds to $\tilde{\phi}_{II} = \tilde{\phi}_I + arg(1 + C_\tau)$, where $C_\tau = B_\tau A_\tau^*/A_\tau$

4.5 Simulations

We have performed stochastic simulations to evaluate the behaviour of our feedback system. Fig. 4.5 shows a single realization of the feedback algorithm. The expected effect is found, the photocurrent has to be around Zero and the phase estimate $\tilde{\phi}$ converges to the real value of the phase ϕ_{REAL}.

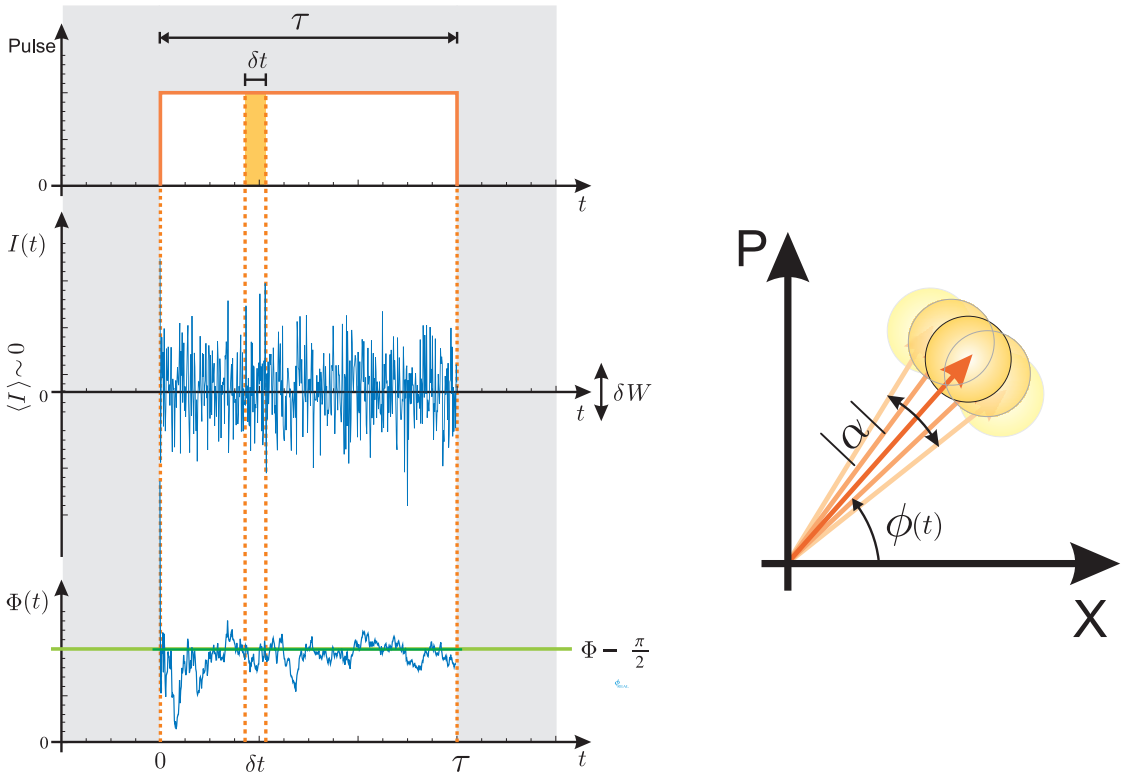

Figure 4.5: Simulated feedback. Homodyne Photocurrent $I(t)$ and Phase estimate evolution

We found during the simulations that the convergence of the feedback is linked to the feedback gain, as is shown in figure 4.6. This is a very important detail that has to be taken into account for an experimental realization. Note that there are cases where one could have a small standard deviation but a wrong final estimate, so it is more useful to increase the feeback gain until one ensures that the estimate converges deterministically to the actual value of the phase.

After performing intensive simulation, we find a collection of trajectories followed by the phase estimate and accumulate them. In Fig. 4.7, we present the range of variation of those trajectories in time (maximum and minimum values) as a green area, their standard deviation (orange curves) and mean value (black line). Notice that for

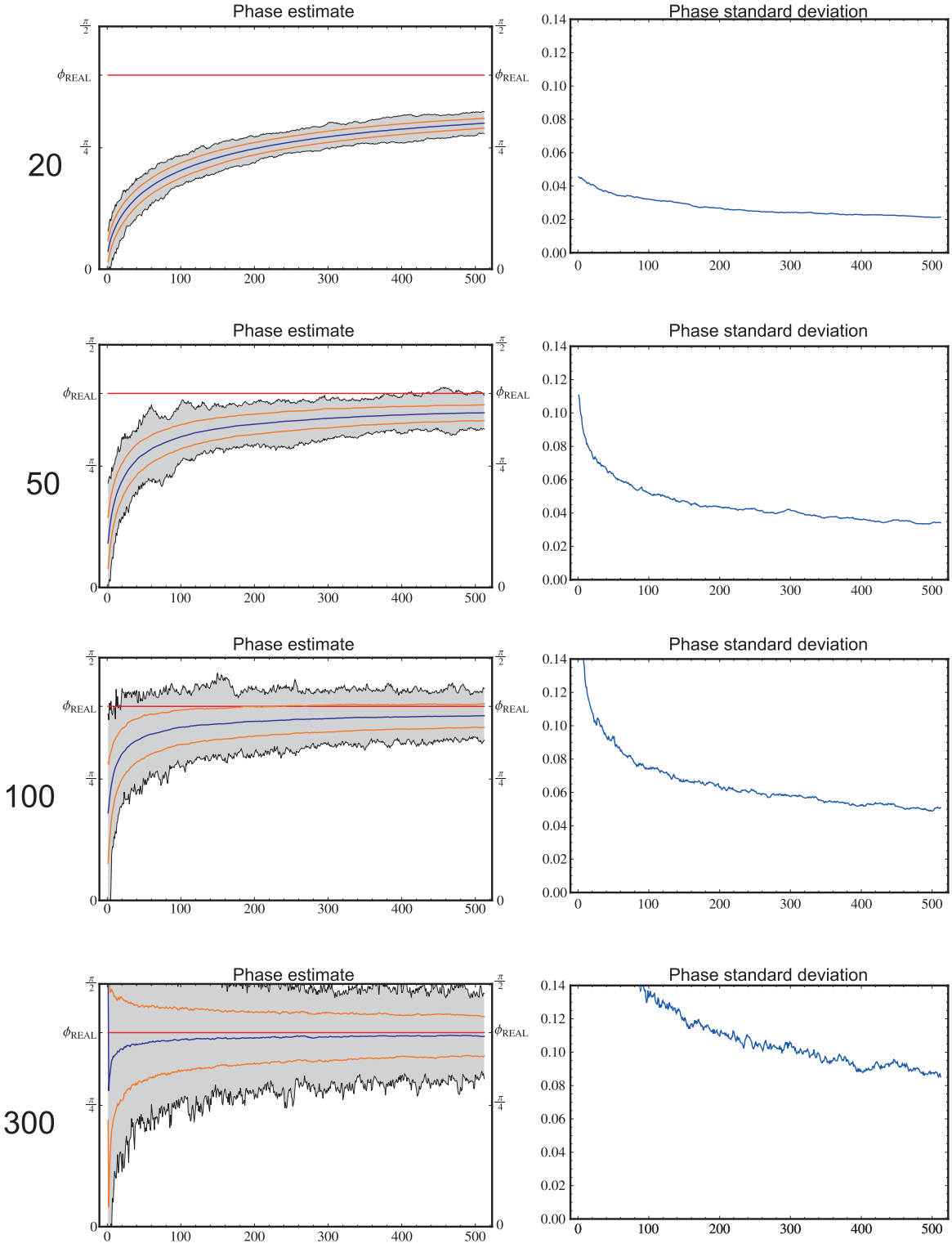

Figure 4.6: Effect of feedback gain in the convergence and standard deviation of the simulated feedback.

the gain selected, the convergence of the estimate trajectories to the real phase value (red horizontal line) is very fast. From those trajectories we can extract the last value that correspond to the final estimate, as is plotted in the center of the figure. One can also plot a histogram of those individual estimates and we found a Gaussian-like distribution. We can repeat this process for different coherent amplitudes, and as can be seen in the upper right corner, they tend to the same mean value. The phase variance depends on the amplitude and it is shown in the lower right corner, where the phase variance of the simulation follows the theoretical asymptote (orange) and the black line corresponds to the ultimate quantum limit.

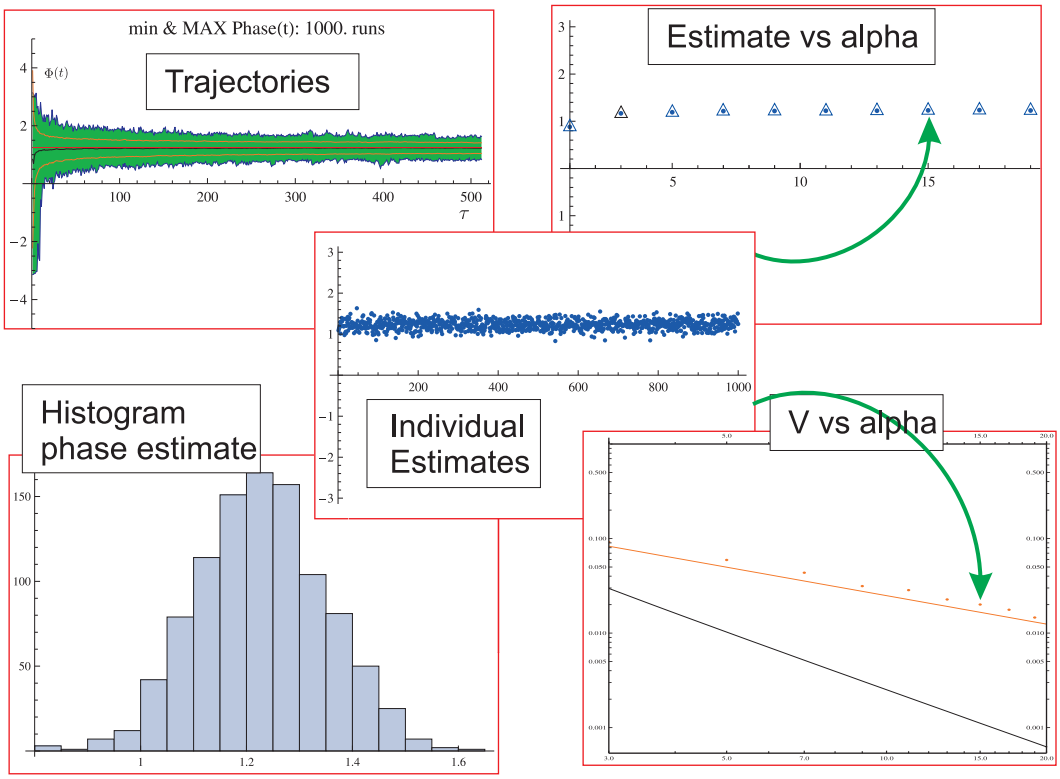

Figure 4.7: Summary of simulations. Trajectories, Estimates their varinaces and histogram.

4.6 Experiment

4.6.1 Setup

The experimental setup is shown in Fig.4.8. The light source is a CW Nd:YAG laser operating at 1064nm whose output is spectral and spatially filtered through a mode cleaning cavity (MCC), which minimizes the excess noise in the field and produces a clean TEM_{00} mode[8]. The MCC output is then sent to a beam splitter (BS) with variable transmission, composed of a half wave plate (HWP) and a polarizing beam splitter (PBS), where the power ratio between signal beam and local oscillator is set.

State preparation

We choose to prepare our quantum states at the sideband modes ($\pm$10MHz) of the signal beam [58], since this allows us to avoid classical noise at low frequency originated from mechanical instabilities and low frequency noise in the laser. The sidebands of our signal beam (after the MCC cleaning) are in a vacuum state (quantum noise limited) before we impose any modulation onto it. For the preparation, we use a pair of electro-optical modulators (EOM) which allow us to generate pure sideband coherent states by transferring energy from the optical carrier to the vacuum sideband. The EOMs are independently driven by two phase-locked RF signal generators running at 10MHz, giving independent control on the phase and amplitude of our signal states. The amplitude modulation is achieved by preparing the signal beam in circular polarization (by a combination of HWP and QWP) which is sent through a birrefringent electro-optic crystal (first EOM in Fig.4.8). This results in a polarization modulated beam, which is mapped into amplitude modulation by sending it to a PBS that will select only the horizontal component of the field. The phase modulation requires only this linearly polarized beam to be sent through the crystal(s) of the second modulator.

Local Oscillator

An essential component of the experiment is the local oscillator, with which we set the phase reference (direction of the $\hat{X}$ quadrature) and control the feedback loop for the adaptive measurement. Our LO is a bright coherent beam with an optical power of about 12mW while the sideband states are typically of only few pW. We control the LO phase, Φ, by sending it through a wave guide phase modulator (WGM), driven with an FPGA as will be described later. The input and output of the WGM are

[8]Further details about the MMC, regarding performance and control are omitted as they are not relevant for the current discussion.

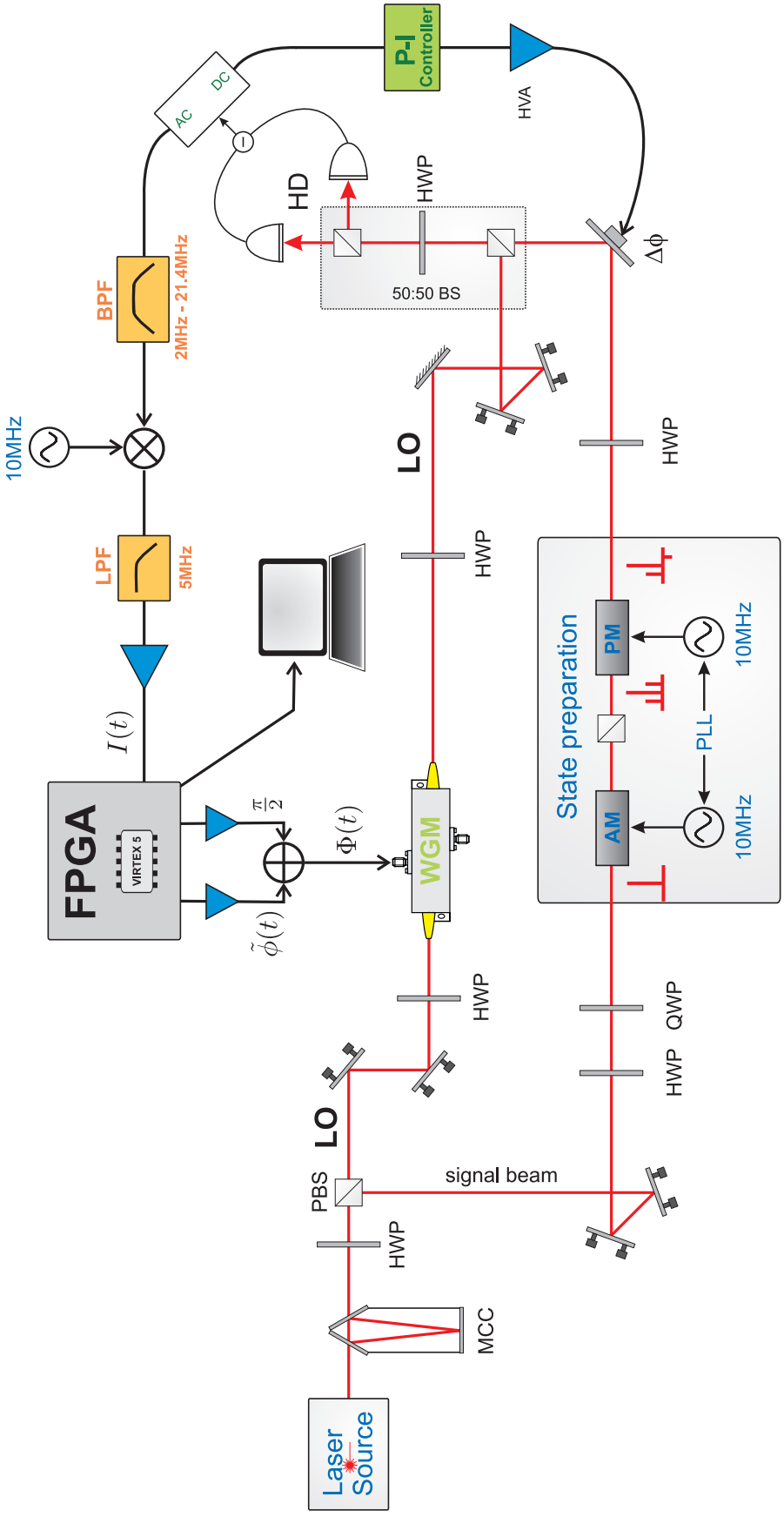

Figure 4.8: AdaptiveSetup

connected to polarization maintaining fibers (PM-fibers) that allow us to precisely control the polarization of the beam. The use of the WGM[9] implies an insertion loss of 4dB added to the incoupling losses into the fiber, but we chose it and use it due to its remarkable speed that outperforms by far all our modulators. Moreover, these losses are not critical since no quantum features are lost, and the output power (12mW) output is more than enough to drive the experiment. The clearance of the SNL over the electronic noise on the homodyne detectors, while performing the experiment is about 17dB.

Detection

The LO and signal beam are interfered on a BS formed by a combination of two PBS and a HWP, and adjusted to be 50:50 as indicated in Fig.4.8. Homodyne fringe visibility:

$$VIS = \frac{I_{max} - I_{min}}{I_{max} + I_{min}} \tag{4.46}$$

is a measure on how good the interference is. I_{max} and I_{min} are respectively, the maximum and minimun of the optical intensity in the interference fringes. The visibility (VIS) needs to be maximized, to minimize the losses. Several factors are detrimental for the visibility, in particular:

1. Direction mismatch of the beams, which is solved by *beam walking*[10]

2. Non parallel polarization, solved by rotating the polarization with HWPs.

3. Non perfect overlap that is solved with mode matching lenses.[11]

After optimizing these aspects, we obtain for our setup a visibility of 97%. The interference is finally sent to the individual detectors which consist of *Epitaxx500* InGaAs PIN photodiodes. Each of these two photodiodes is internally connected to a transimpedance amplifier that converts the photocurrent to voltage. The detectors' bandwidth is approximately 20MHz. Their quantum efficiency of the diodes is about $\eta_{PIN} = 90 \pm 5\%$ which results in an overall detection efficiency[12] of $\eta_{overall} = 85\%$. The HD photocurrent is internally divided by our detectors on AC and DC components[13], the first of which will contain the measurement information (in the mentioned sidebands) and the second is used to phase lock the HD to a specific quadrature.

[9] Technical specifications of the WGM can be found in Appendix 2.

[10] It is an experimental technique consisting in steering a pair of mirrors to fully control the direction of a beam.

[11] Extra optical components used for mode matching the beams, incoupling into the modulators, cavity and focussing into the detectors are excluded for simplicity.

[12] $\eta_{overall} = \eta_{PIN} \cdot VIS^2$

[13] Notice that what we call DC, has reality a BW of few Hz to resolve the interference fringes.

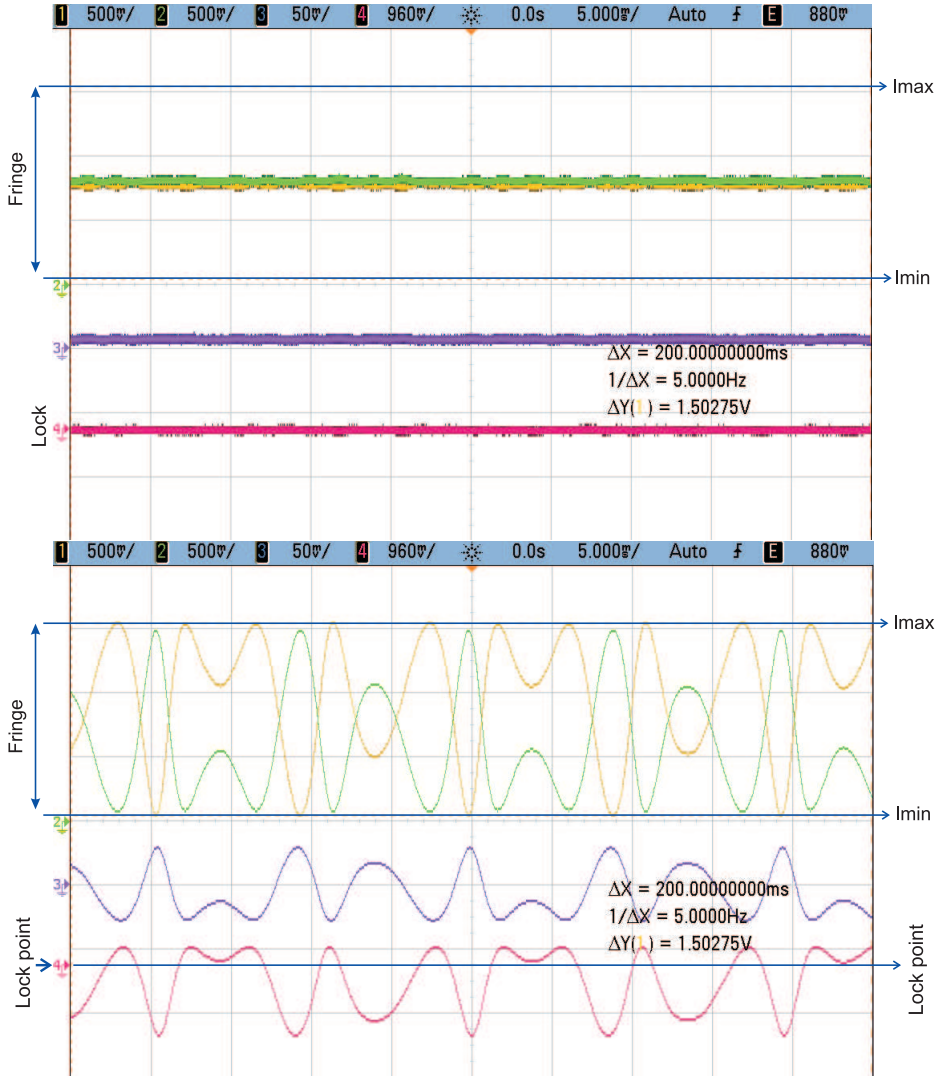

Figure 4.9: Time traces for **a.** Locking and **b.** Scanning the phase of LO. traces 1 and 2 are individual detectors in HD. 4. PI controller locking monitor. The 'fringe range' at HD detectors is indicated.

We measure the subtraction of the AC homodyne on a SA, resulting in a common mode rejection of about 30dB. The subtracted signal is then Band-passed filtered with $f_{min}^{BPF} = 2MHz$ to cancel low frequency noise coming from the relaxation oscillations of the laser and ($f_{max}^{BPF} = 21.4MHz$) that eliminates any effect from the MCC locking frequency (33.5MHz). The signal is then mixed with an electronic local oscillator at $f = 10$MHz from a RF signal generator. This produces 2 beating signals of which we retain only the low frequency component by using a low pass filter ($f_{cut}^{LPF} = 5MHz$) . Note that the last filter is the limiting factor for the speed of the FPGA loop.

Lock

The DC part of the homodyne signal is used to stabilize the interference between signal beam and LO. For this purpose, we use a PI controller in a DC lock, that give us the possibility to monitor the fringes, as seen in the 4th trace in Fig.4.9b, and also to set the lock point in the fringe (4th trace in Fig.4.9a) This lock is used to maintain a fixed relative phase over long periods of time compared to the pulse duration. We can make several single shot measurements on the same state's phase to construct statistics and calibrate our device. This is intended to be a relatively slow lock with a bandwidth (BW) of just few KHz, so that it is not affected by very fast oscillations like those caused by the fast FPGA loop, hereby avoiding conflict between both loops. The limiting factor for the speed of this lock is the High voltage amplifier (HVA) used to drive the piezo, whose BW is approx. 1KHz.

LO control (FPGA)

For an active control of the local oscillator's phase, we needed an electronic controller capable of signal processing at a very high speed, in such a way that could perform a feedback faster than the pulse duration, which is an essential condition for the adaptive single shot measurement we are interested in. The best candidate for this task is a field programmable gate array (FPGA) that is a powerful electronic device consisting of a silicon chip with reprogrammable digital circuitry [86]. The downside of this technology is that the user has to define and configure every single component used, their interconnections, clock management, etc. This is generally specified using a hardware description language (HDL), such as VHDL. This makes it harder to use than, for instance, microcontrollers but they are generally slower and more restricted. So, FPGAs are not a "plug and play" technology but their versatility pays off when they are used for demanding tasks as ours.

We selected a Virtex 5 FPGA board and an analog interface card[14] that performs conversions: digital to analog and vice versa through ADC and DAC converters that sample input and output respectively, at 100MSPS[15]. The converters we use have a discretization of 14bits, allowing in principle to divide input and output signals into 16384 voltage levels. The main components of our FPGA system are depicted in Figure 4.10 and described below.

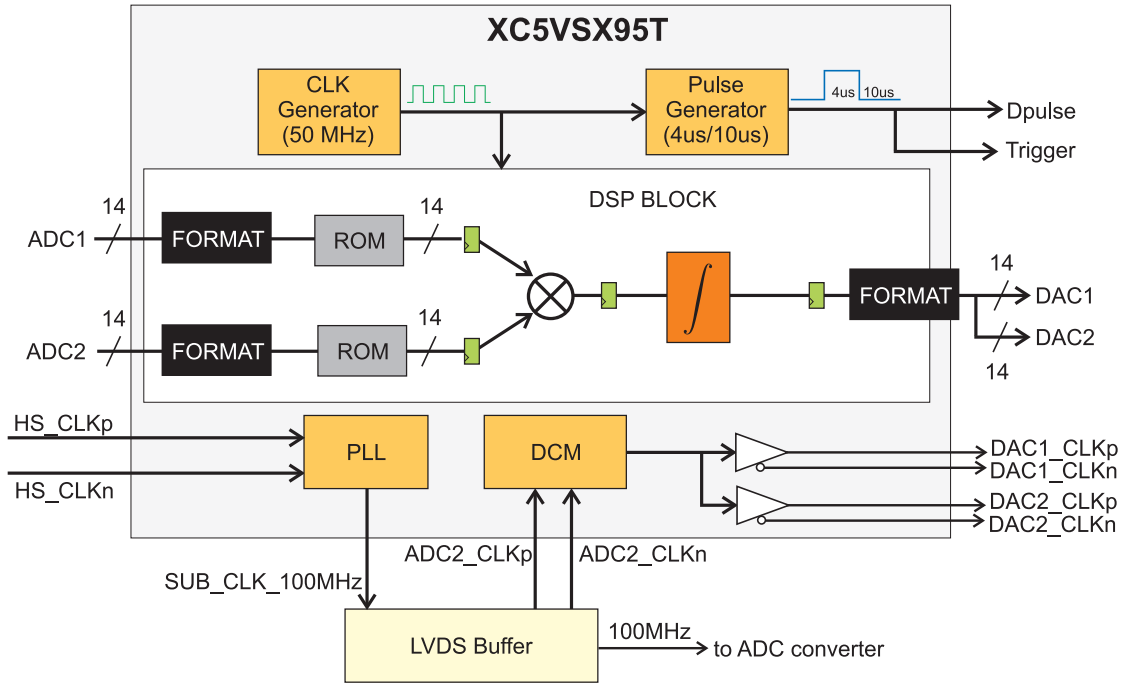

Figure 4.10: Main components of the FPGA: timing control elements (light orange boxes), DSP block and connection to external hardware. These digital elements and their connections are defined in VHDL hardware programming and downloaded to the chip.

Timing

The original clock in the board runs at 50MHz which is not enough to run the system, so we set our global clock to run at 100MHz and drive the ADC and DAC converters, by using two elements: a phase locked loop (PLL) and digital clock manager (DCM) [87]. We later create a clock at 50MHz dedicated to drive the digital signal processing

[14]FPGAs boards are digital, if the use mixed signals (analog and digital) is needed as in our case, one has to find an appropriate analog card specifically designed for the FPGA board and they are normally scarce for the speed we required.

[15]more details about the board are found in the Appendix ??

(DSP) block and a pulse generator that will output a digital signal used to define the state and the time between measurements. This digital pulse is split to be used also as a trigger to collect the data and to make the required $\pi/2$ phase shift on the estimate $\tilde{\phi}$. The synchronization of the components is important to perform the calculations on time but its details along with those for enabling and resetting the elements after each pulse are omitted for simplicity.

DSP block

One needs to understand that FPGAs are very fast devices but the only thing they are able to do, is bit operations on strings of 1's and 0's according to digital logic. They do not "understand" mathematics the way we do. We therefore have to translate or approximate those operations that are natural for us (negative numbers, decimals, multiplications, integrals, etc.) into binary language, in order to correctly perform the processing of our signals. This is important because as we use hardware programming, one has to take these details into account.

Our DSP block (shown in Fig. 4.10) runs at 50MHz, and is configured to receive a signal and multiply it by a function proportional to $1/\sqrt{t}$ that we store in a ROM memory. This product is later sent to an element that approximates an integral of its input and the result is sent to the board's output. Other extra blocks are needed in order to translate binary formats between converters and signal processing.

Let us analyze this operation. We are taking an input HD measurement point, multiply it for an exotic function of time, integrate and deliver it, all of this every **20ns** back into the system[16]. It cannot be stressed enough the difference between doing this real time feedback (where a delay of some 10's of ns could spoil the result) and standard protocols of common use in quantum optics (like post-selection), that normally have the option to analyze the data offline, this is, at anytime and even in a computer.

From the FPGA, we define our pulse to be of 4μs long, Fig. 4.11, LPF in down mixed HD remains constant during 200μs and we perform operations at 50MHz, which give us the possibility of over sampling the data.

4.6.1.1 Adaptive feedback loop

Finally, our feedback loop is composed of the HD, FPGA and WGM. The HD measurement is sent to the FPGA to be processed by the DSP block that gives a partial

[16]of course we do not use all this BW in the optical system due to the Low pass filter in the measurement that limits the speed of the loop.

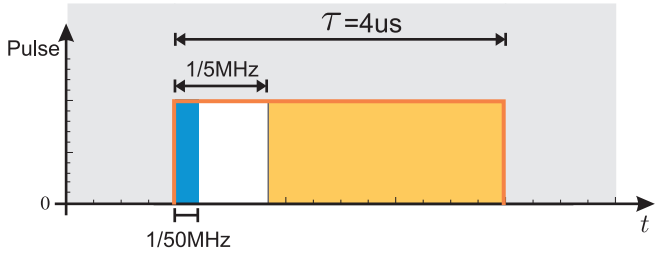

Figure 4.11: Time scales, **Orange square:** the pulse defining the state $\tau = 4\mu$s, **White:** minimum resolved part of the state due to LPF (∼200ns) **Blue:** calculation time (∼ 20ns).

phase estimate $\tilde{\phi}(t)$. The algorithm, eq. (4.44), requires the addition of $\pi/2$ to that estimate, which is done by an analog sum with a digital pulse whose voltage corresponds to the proper phase shift on the WGM. This sum acts on the LO via the WGM as shown in Fig.4.8. In addition to this, we need to care about the different gains in the feedback:

1. FPGA input gain (analog): It has to be adjusted to cover the full dynamic range of the input, in order to minimize errors due to discretization.

2. FPGA output gain 1 (analog for digital pulse): It has to be tuned to reach $\pi/2$ in the WGM (as explained above).

3. FPGA output gain 2 (analog for estimate): It needs to cover 2π in the WGM.

4. FPGA internal gain2 (digital): has to set to adjust the overall feedback gain (see simulations) at the same time as avoiding to saturate the integrator.

4.6.2 Experimental Results

In Fig.4.12, we present typical time traces obtained while running our experiment. The temporal definition of the pulse is shown in the orange trace, that is set by the FPGA as previously explained. At the same time, it sets the measurement period (high voltage intervals) of 4μs and the time between measurements is 10μs. This figure presents 4 different single shot measurements of a fixed phase.

The phase estimate trace (purple) shows a clear spike at the end of every measurement period. It is mainly caused by the switching off of our integrator that produces a sudden change in the FPGA output. We were not concerned about it, because it does not affect our measurement record (it happens between measurements) but also because we consider it beneficial for this protocol as it helps randomizing the initial phase estimate (beginning of the pulse) which emphasizes the *ab initio* character of

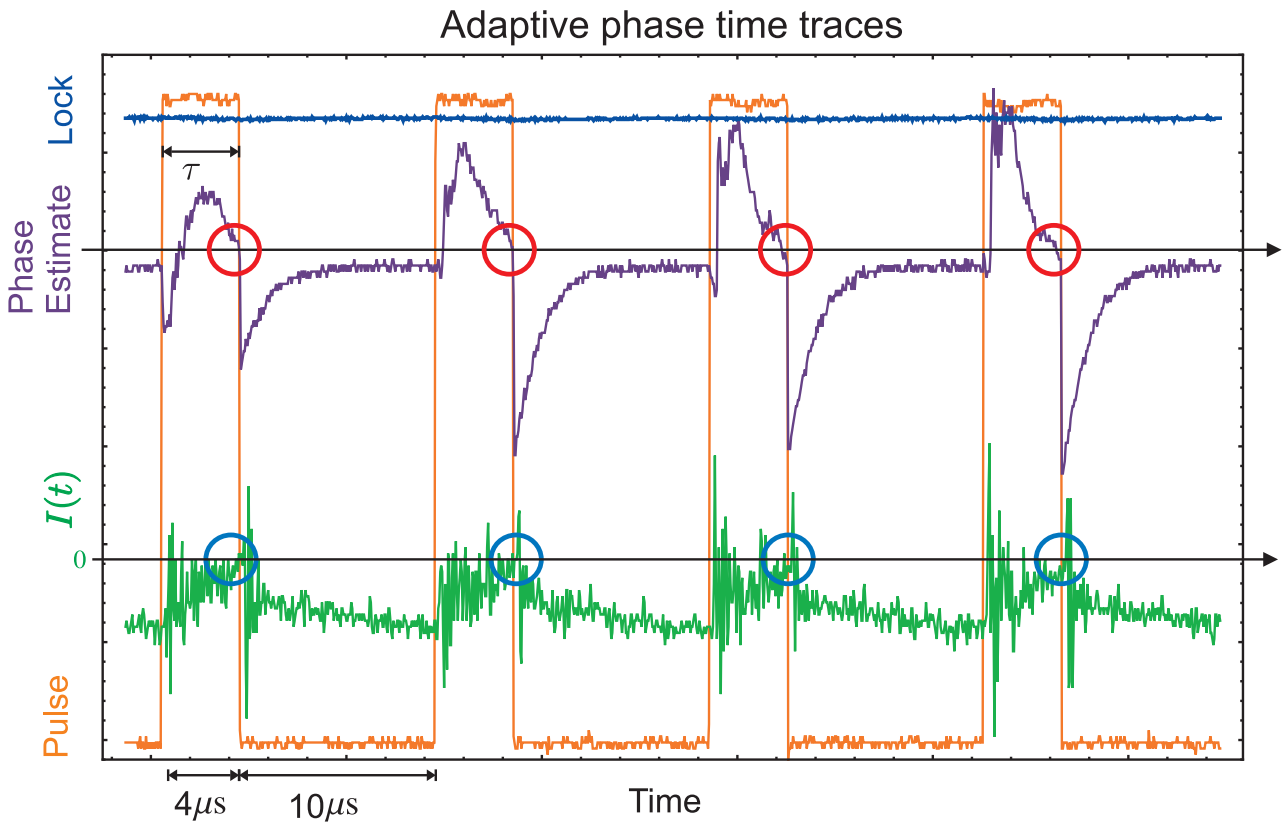

Figure 4.12: Time traces. **Orange:** time definition of the pulse, **Green:** Downmixed HD photocurrent, $I(t)$, **Purple:** the phase estimate $\tilde{\phi}(t)$ and **Blue:** DC HD monitor.

our phase estimation. The red circles on top of this trace indicate the last phase estimate and we can see that it consistently ends around the same phase. The green trace, shows the AC HD photocurrent, $I(t)$, and we notice that during the measurement, the FPGA forces the system to take this current to zero, indicated by the blue circles which means that we end with the LO orthogonal to the signal. During the period between measurements, the FPGA does not act and the state returns to the original position set by the DC lock, which is also observed in the figure through the HD current I. The blue trace is the DC signal from one of the HD that helps monitoring the performance of the lock which in this case is very good. In general we observe that it keeps the lock over long enough periods to perform thousands of measurements. We now proceed to measure a large amount of pulses and observe

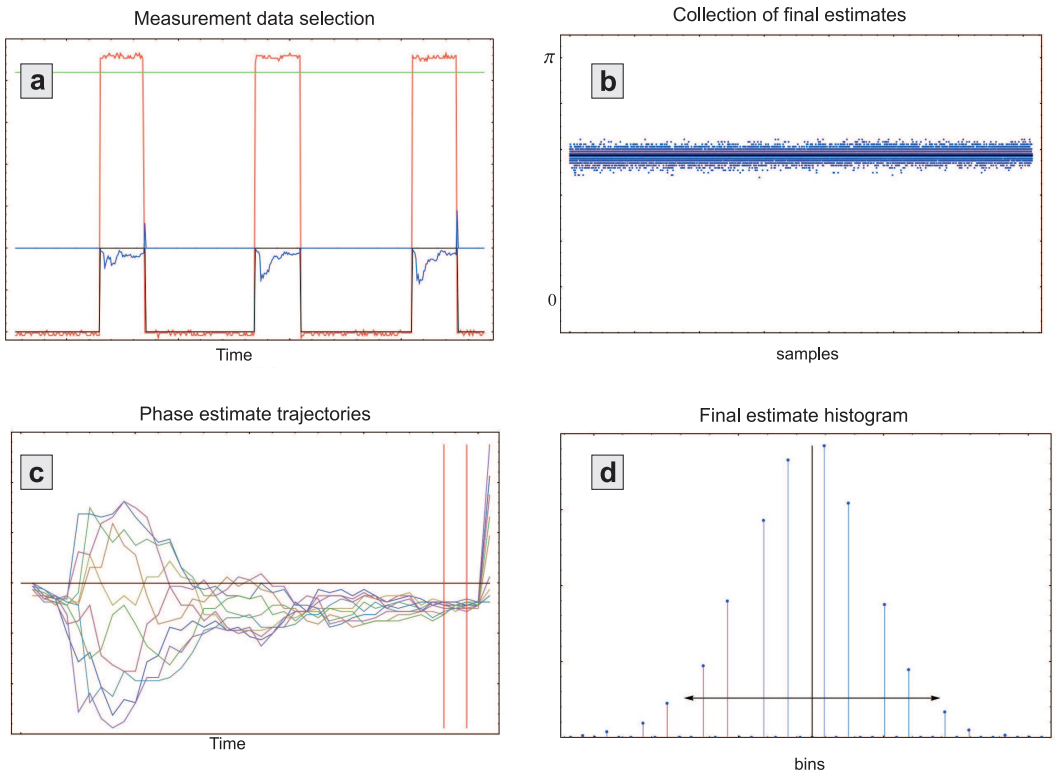

Figure 4.13: Estimates Analysis. **a.** Extraction of measurement information from the full time trace. **b.** Phase estimate trajectories for 10 different pulses, where the vertical lines indicate the position of the last estimate. **c.** Collection of estimates after performing 15000 single shot estimations. **d.** Histogram of the estimates shown in c.

the statistical behavior of the estimate. Figure 4.13 presents the analysis of the data after performing 15000 single shot estimations. First, we extract the measurement

information from the full time trace and eliminate the rest (a), we extract the trajectories followed by the phase estimate $\tilde{\phi}(t)$ in each run and take the final estimate given by the last point in the measurement and indicated in the figure by a pair of vertical red lines (b.). Now with the collection of final estimates (c), we can proceed to construct a histogram (d). The histogram has a Gaussian-like distribution and this is the confirmation that the estimate consistently sets at the same point. We can now go further and do the same analysis for different phases by locking the system at different fringe points. The result is shown in figure 4.14, where we took 4 different phases. Here we see that the qualitative behavior of the estimation is correct, as the distribution presents a different phase shift estimate for every prepared phase. We also notice a different variance for the estimates depending on the position of the lock on the fringe and we attribute this to the variable sensitivity of the system that depends on the lock position. The system has a higher phase sensitivity at midfringe (steeper slope) and therefore responds better to the FPGA loop as in 4.14b and c, while performing worse in the fringe extrema a and d, because the system responds slower and the FPGA control is less effective which results in a larger dispersion of the estimates.

Final remarks and future plans.

Until here we see that qualitatively the system behaves as expected, since:

1. The photocurrent is set to zero at the end of the measurement period

2. The phase estimate settles consistently to the same value when keeping the phase constant.

3. Different prepared phases produce estimates with different mean values.

The next step would be to quantify the performance of the controller via estimates for different amplitudes and phases and this requires a careful preparation of the states, a very precise calibration of their phases and larger amounts of data. Due to time limitations, we decided to try to calculate a rough values for the estimates and their variances based on the data we had and leave a more detailed system calibration for another time. We took an arbitrary state and assigned phase zero when locked at the lower fringe point and π when locked at the top and used this as a reference for the other states. The result is shown in fig4.15, where the yellow boxes represent coherent states of definite amplitude and measured at different phases. The reference is state 2. The tendency we observe with this rudimentary procedure is again that when we lock close to midfringe (90 degrees in the figure), the variance is smaller.

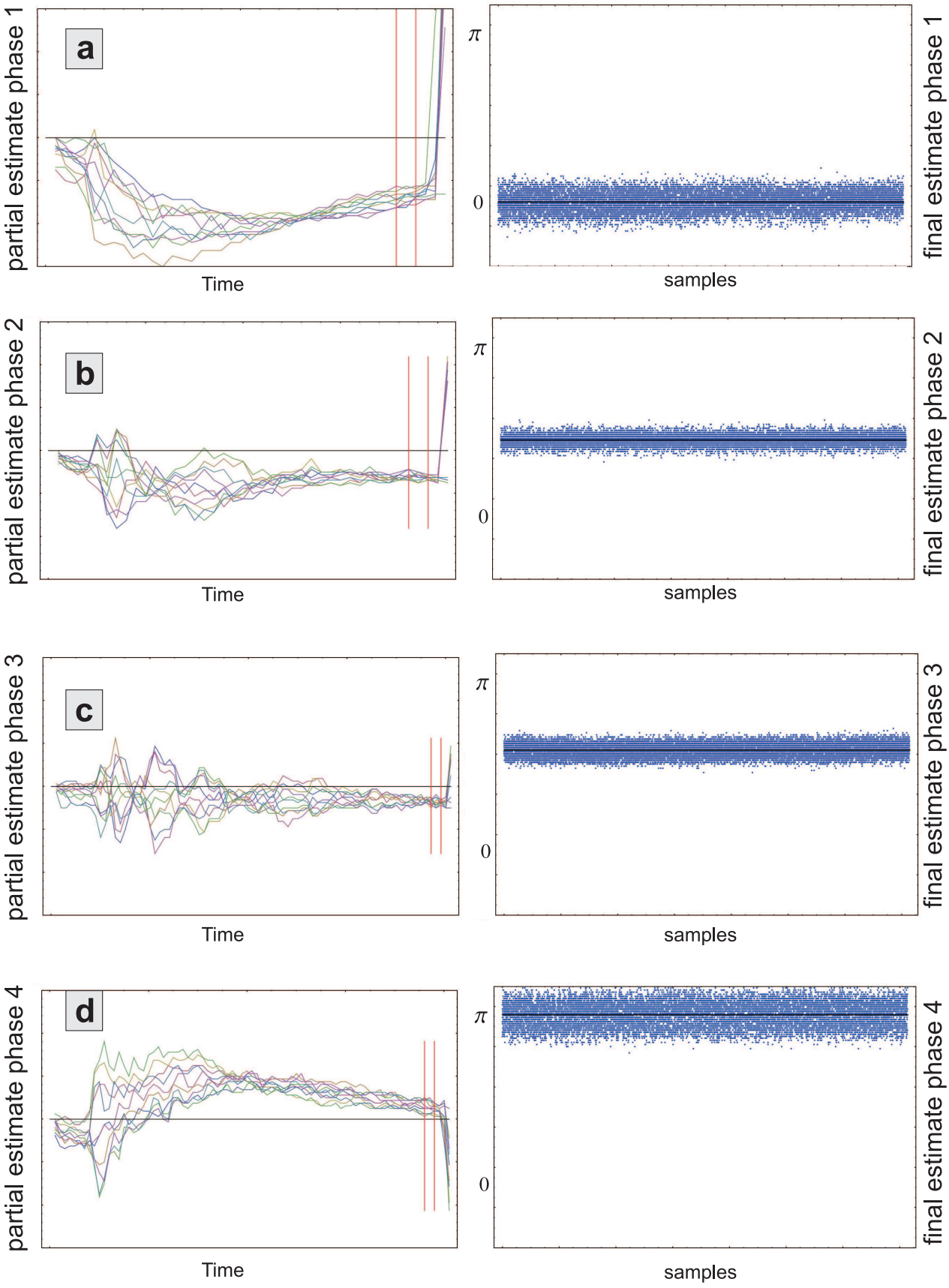

Figure 4.14: Phase Estimates at different phases

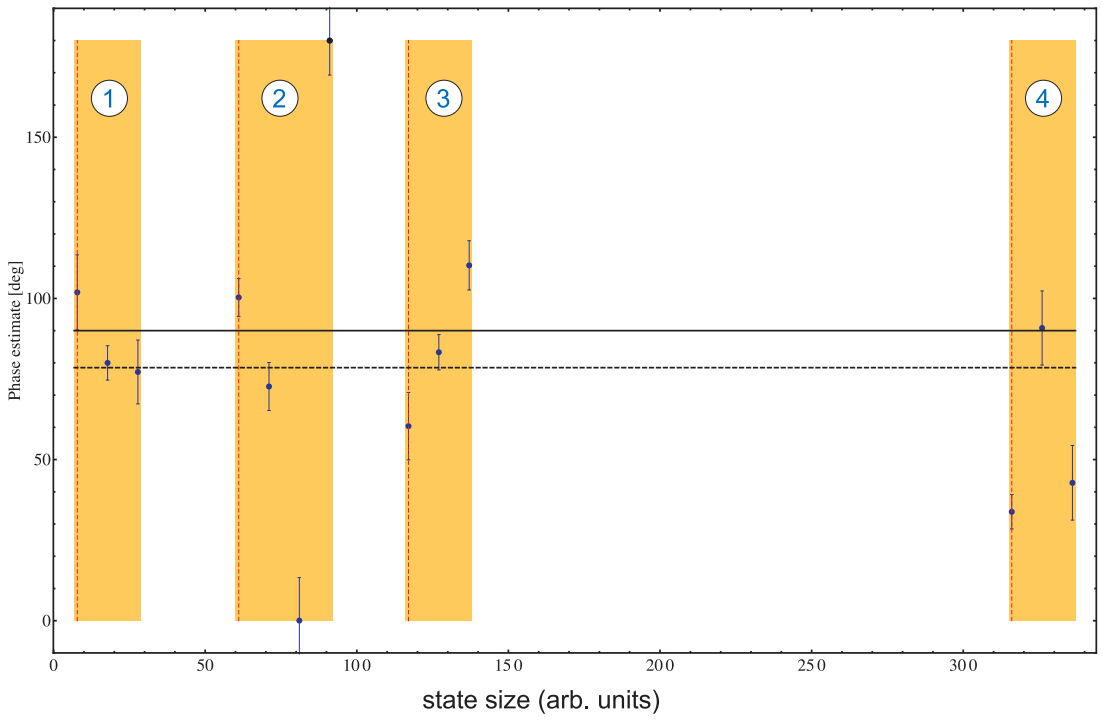

Figure 4.15: variance of estimates with different state amplitudes

In order to perform a detailed calibration, it is needed to eliminate some power fluctuations that the system has over long periods, and we relate them with a non optimal performance of the MCC, that will affect our lock. Other steps that would help to improve the system would be to recalibrate frequently (not only once) and use a different locking technique that is independent of power fluctuations.

The preparation has to be done at a single lock point the one we identify with minimum variance: midfringe and control the modulators to generate the phase shifts and check the performance for: a. states with equal amplitude and different phases b. states with different amplitude

In the future: we plan to have a better phase control caring specially on eliminating any excess noise source to later perform the experiment with squeezed states with which one presumably beats the SQL.

4.6.3 Conclusions

We started the study of adaptive feedback in quantum optics and acquire understanding of a very general theory of phase estimation via homodyne measurements. We have shown experimentally the basic components of the most complicated version of phase estimation, that is to estimate the phase with a single copy of the state (single

shot) without any initial reference (ab initio) by progressively aquiring information via HD. This was done by combining a quantum optical setup with very high speed control, which is technically demanding. It is important to stress that the theory presented as well as the experimental ingredients shown, can account for most (if not all) the phase estimation (given the appropriate experimental tuning and control policy) protocols: single shot/repeated measurements, adaptive/nonadaptive, ab initio/phase sensing and combinations.

Chapter 5

Quantum State Discrimination

Contents

5.1 Introduction

The field of Quantum Communication [51] deals with the preparation, transfer and reception of quantum states. It allows for the secure transmission of secret information [50, 54] and can be used to increase the capacity of transmission channels. The information carriers are quantum states that can vary in complexity from single photons or coherent states to exotic entangled states. We will focus on coherent states as they have proven to be a very robust system, they are easy to prepare and compatible with current technology. Moreover, this type of states is of interest in quantum communication as they allow for unconditional secure information transfer between two parties in a network, which is a result of the impossibility of perfectly discriminating different coherent states.

In a standard communication scenario, there is a specific set of quantum states $\{\hat{\rho}_0, \hat{\rho}_1, \ldots, \hat{\rho}_N\}$ called the alphabet, that is used to encode the information to be

transmitted. This set is known by both parties: sender and receiver. The task of a detector is to decode the information by identifiyng which of the states was sent. This task of state discrimination, however, is not trivial when the alphabet is composed of non orthogonal quantum states. In fact, quantum mechanics in this case forbids any physical device to identify with certainty which state is received. In practice, this means that every detector will unavoidably make errors[1], and the field of quantum discrimination aims at using the tools of quantum mechanics to minimize these errors.

The aim of quantum state discrimination (QSD) is not necesarily to acquire all the information about a state by a precise measurement of it (as in quantum estimation) but rather to construct a measurement apparatus that can distinguish a state within the given alphabet with minimum error.

In this chapter, we will present some examples of measurement devices that discriminate states in a coherent state alphabet and present their corresponding error probability. First, binary discrimination is discussed which is later extended to the case of 4 states in a new proposal.

Hypothesis testing

In QSD, a detection device has to make decisions based on measurement outcomes. This can be formally stated as a hypothesis testing procedure, by associating a given decision with a possible measurement outcome of the detector.

When there are different options to chose from, one can organize them as a set of hypotheses: $H = \{H_0, H_1, \ldots, H_N\}$ and express the overall probability of error as:

$$P_{err} = \sum_{k \neq l} P(H_k|H_l)P(H_l). \tag{5.1}$$

The conditional probabilities $P(H_k|H_l)$ are associated with wrong decisions: they refer to the probability of selecting hypothesis H_k, given that the correct option was H_l. They are weighted by the priors $P(H_l)$, which are probabilities that we assign to the occurrence of the event H_l based on information previous to the measurement.

[1] This impossibility of perfectly distinguish non-orthogonal quantum states in other contexts can be used as an advantage, for example it powers the field of quantum key distribution [53] where it is possible to identify when an eavesdropper tries to acquire information as this disturbes the state.

In quantum discrimination, we are given the alphabet $A = \{\hat{\rho}_0, \hat{\rho}_1, \ldots, \hat{\rho}_N\}$, and a set of a priori probabilities:

$$P(\hat{\rho}_k) = p_k, \quad \sum_k^N p_k = 1 \tag{5.2}$$

so, we can directly assign a hypothesis H_k to its k-th element, $\hat{\rho}_k$. As there is no ambiguity in this context, we use the notation $P(\hat{\rho}_k)$ to express $P(H_k)$ and $P(\hat{\rho}_k|\hat{\rho}_l)$ for $P(H_k|H_l)$. To calculate the probability of error in eq. (5.1), we need to define the measurement procedure in terms of a POVM[2], and finally apply Born's rule, as it will be shown later.

5.2 Binary decision problem for coherent states

Let us imagine a scenario where we want to transmit binary information, i.e. strings of 1's and 0's. The simplest way to do this is to transmit one bit[3] of information per state, so, the minimum number of states required is two and the alphabet would be given by: $A = \{\hat{\rho}_0, \hat{\rho}_1\}$. This alphabet is illustrated in Fig.5.1.

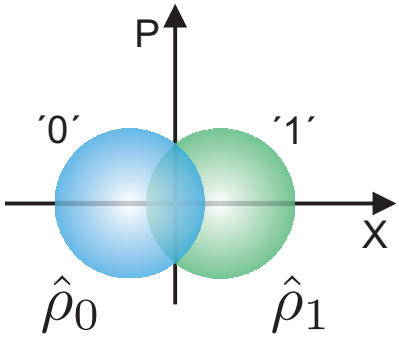

Figure 5.1: Binary state comunication, where quantum states $\hat{\rho}_0$, $\hat{\rho}_1$ represent classical bits 0, 1

For example, if the sender wants to transfer the message $\{0, 1, 0, 0, 1, 1, 0, 1\}$, she will prepare and send the following sequence of states: $\{\hat{\rho}_0, \hat{\rho}_1, \hat{\rho}_0, \hat{\rho}_0, \hat{\rho}_1, \hat{\rho}_1, \hat{\rho}_0, \hat{\rho}_1\}$.

The receiver faces a binary discrimination problem where the aim is to discriminate $\hat{\rho}_0$ from $\hat{\rho}_1$ with prior probabilities p_0 and $p_1 = 1 - p_0$. These probabilities are known to the the receiver. We then state the hypothesis as:

[2]POVMs are introduced in section 2.7.

[3]It is important to note that these are classical bits encoded in quantum states, as opposed to quantum bits or *qubits* that are also used in quantum comunication and computation [44].

H_0: the state $\hat{\rho}_0$ was sent.
H_1: the state $\hat{\rho}_1$ was sent.

The error probability takes in this case a simple form:

$$P_{err} = P(\hat{\rho}_1|\hat{\rho}_0)p_0 + P(\hat{\rho}_0|\hat{\rho}_1)p_1. \tag{5.3}$$

and we can now express it in terms of measurements. As there are 2 possible outcomes, we can simply use a two-element POVM $\{\Pi_0, \Pi_1\}$. The conditional probabilities are given by $P(\hat{\rho}_k|\hat{\rho}_l) = \mathrm{Tr}[\hat{\Pi}_k\hat{\rho}_l]$ and the error probability is then:

$$\begin{aligned} P_{err} &= P(\hat{\rho}_1|\hat{\rho}_0)p_0 + P(\hat{\rho}_0|\hat{\rho}_1)p_1 && (5.4)\\ &= p_0\mathrm{Tr}[\hat{\Pi}_1\hat{\rho}_0] + p_1\mathrm{Tr}[\hat{\Pi}_0\hat{\rho}_1] && (5.5)\\ &= p_1 + \mathrm{Tr}\left[(p_0\hat{\rho}_0 - p_1\hat{\rho}_1)\hat{\Pi}_1\right]. && (5.6) \end{aligned}$$

5.2.1 Detection Schemes and Helstrom bound

We now proceed by evaluating the error probabilities for different detection schemes. In the following we will assume that the sender prepares the following coherent states:

$$\begin{aligned} \hat{\rho}_0 &= |-\alpha\rangle\langle-\alpha| \\ \hat{\rho}_1 &= |\alpha\rangle\langle\alpha| \end{aligned} \tag{5.7}$$

with equal priors: $p_0 = p_1 = 1/2$.

5.2.1.1 Helstrom bound

Helstrom [31] demonstrated the minimum error probability that can be achieved when discriminating between states $\hat{\rho}_0$ and $\hat{\rho}_1$ with a priori probabilities p_0 and $p_1 = 1 - p_0$, which implies a minimization over all possible POVMs:

$$\min_{\hat{\Pi}} P_{err} = \frac{1}{2} - \frac{1}{2}\left\|p_0\hat{\rho}_0 - (1-p_0)\hat{\rho}_0\right\|_1 \tag{5.8}$$

which, for the coherent states in the original aphabet A (5.7), reduces to:

$$\min_{\Pi} P_{err} = \frac{1}{2}\left(1 - \sqrt{1 - e^{-4|\alpha|^2}}\right) \tag{5.9}$$

a physical implementation was proposed by Dolinar [38] and demonstrated recently [39].

5.2.1.2 Kennedy receiver

The states in the initial alphabet $A = \{\hat{\rho}_0, \hat{\rho}_1\}$ cannot be distinguished by direct photon counting, since their only difference is a phase factor that cannot be seen by such a detector. A way to distinguish them is to perform a displacement $\hat{D}(\alpha)$ before the photon counting, so that one of them is shifted to vacuum $\hat{\rho}_0 \to \hat{\rho}'_0 = |0\rangle\langle 0|$, while the other doubles its amplitude $\hat{\rho}_1 \to \hat{\rho}'_1 = |2\alpha\rangle\langle 2\alpha|$. Whenever the photon counter receives $\hat{\rho}'_0 = |0\rangle\langle 0|$, no errors will occur, $P(\hat{\rho}_1|\hat{\rho}_0) = 0$. The detector will make errors if it wrongly decides for $H_0{=}\hat{\rho}_0$ when it actually received $\hat{\rho}_1$:

$$P(\hat{\rho}_0|\hat{\rho}_1) = \mathrm{Tr}[\hat{\Pi}_0^K \hat{\rho}_1] = |\langle -\alpha|\alpha\rangle|^2 \tag{5.10}$$

This is because any coherent state has a finite probability of not producing a detection event. This type of receiver was originally proposed by Kennedy [52], and its POVM (displacement+photon counting) is given by:

$$\begin{aligned} \hat{\Pi}_0^K(\alpha) &= \hat{D}^\dagger(\alpha)|0\rangle\langle 0|\hat{D}(\alpha) = |-\alpha\rangle\langle -\alpha| \\ \hat{\Pi}_1^K(\alpha) &= \mathbb{1} - \hat{\Pi}_0^K(\alpha). \end{aligned} \tag{5.11}$$

Finally, we find that the error probability for the kennedy receiver is:

$$P_{err}^K = P(\hat{\rho}_1|\hat{\rho}_0)p_0 + P(\hat{\rho}_0|\hat{\rho}_1)p_1 \tag{5.12}$$

$$= 0 + \frac{1}{2}|\langle -\alpha|\alpha\rangle|^2 = \frac{1}{2}e^{-|4\alpha|^2}. \tag{5.13}$$

5.2.1.3 Optimal displacement receiver

A recent proposal [23, 55] demonstrated that it is possible to do better than the kennedy receiver, in fact a near-optimal probability of error can be achieved by using the same resources: fixed displacement and photon counting. The associated POVM for this proposal is:

$$\begin{aligned} \hat{\Pi}_0^{OD}(\beta) &= \hat{D}^\dagger(\beta)|0\rangle\langle 0|\hat{D}(\beta) = |-\beta\rangle\langle -\beta| \\ \hat{\Pi}_1^{OD}(\beta) &= \mathbb{1} - \hat{\Pi}_0^{OD}(\beta) \end{aligned} \tag{5.14}$$

where β is the optimized displacement given by the condition [55]:

$$\sqrt{T}\alpha = \beta \tanh\left(2\sqrt{T}\alpha\beta\right) \tag{5.15}$$

The displacement is obtained by interfering the signal states with an auxiliary coherent state on an asymmetric BS with transmittance $T \approx 1$. The error probability for this optimized displacement receiver is found to be:

$$P_{err}^{OD} = \frac{1}{2} - e^{-\left(T|\alpha|^2+|\beta|^2\right)}\sinh\left(2\sqrt{T}\alpha\beta\right). \tag{5.16}$$

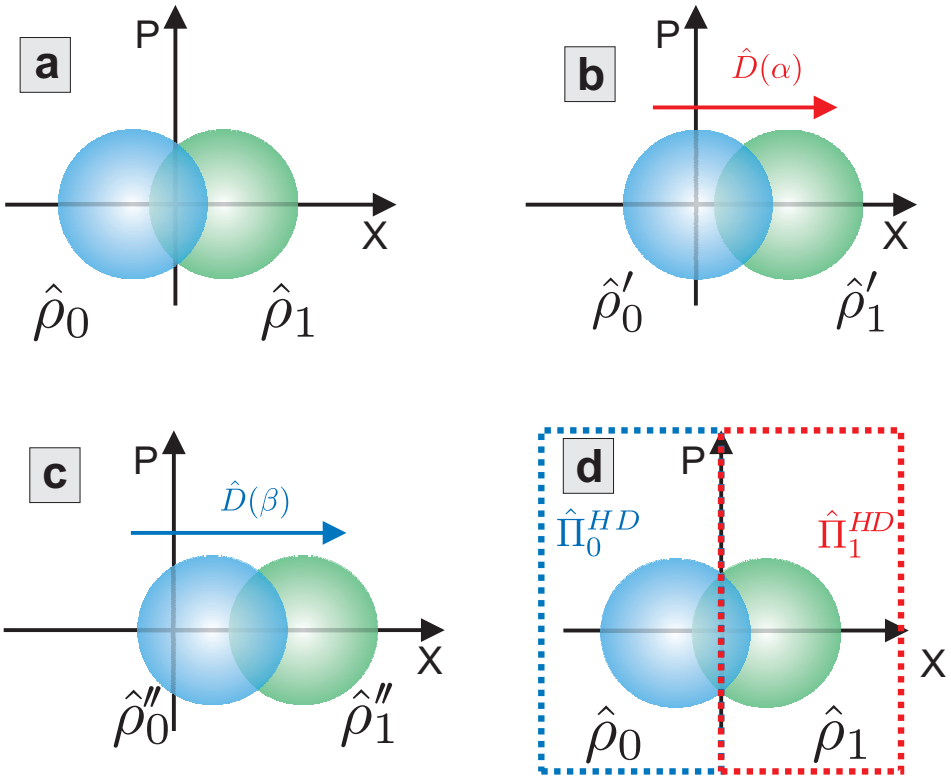

Figure 5.2: Detection schemes and alphabets in phase space:

a. Original alphabet. **b.** Kennedy receiver: The original states are first displaced so that one of them becomes a vaccum state, and they are later measured with a photon counter. **c.** Optimal displacement receiver: An optimized displacement is performed, followed by photon counting. **d.** Homodyne receiver: phase space is divided into two areas: $X \geq 0$ and $X < 0$, and every positive outcome selects $\hat{\rho}_1$.

5.2.1.4 Homodyne receiver

A homodyne receiver can be used to discriminate states from the alphabet A, by the following hypothesis:

H_0: If the HD outcome is $X < 0$, $\hat{\rho}_0$ was sent.
H_1: otherwise, the state $\hat{\rho}_1$ was sent.

This is captured by the following POVM:

$$\hat{\Pi}_0^{HD} = \int_{-\infty}^{0} |x\rangle\langle x|\, dx,$$
$$\hat{\Pi}_1^{HD} = \mathbb{1} - \hat{\Pi}_0 \tag{5.17}$$

and the Homodyne error probability is:

$$P_{err}^{HD} = \frac{1}{2}\left(1 - \mathrm{erf}\sqrt{2}|\alpha|\right). \tag{5.18}$$

To sumarize, we can find in Fig. 5.2, the states used in the presented detection

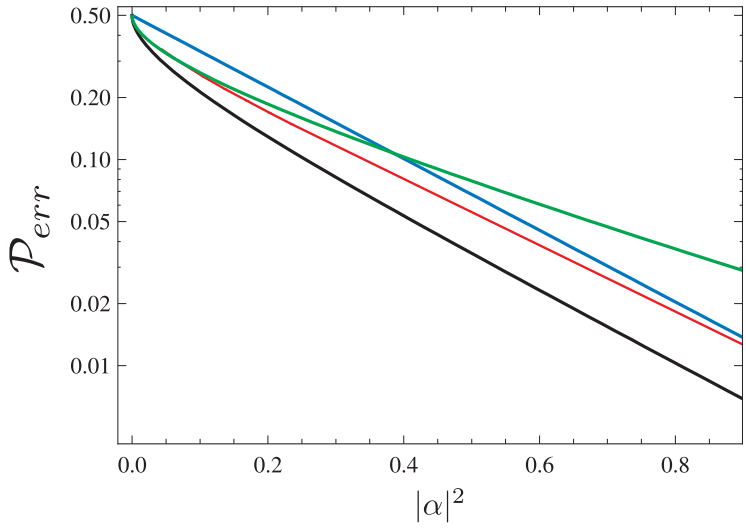

Figure 5.3: Error probabilities vs $|\alpha|^2$: **Blue:** Kennedy receiver **Green:** Homodyne **Red:** Optimized receiver **Black:** Helstrom bound.

schemes, illustrated in phase space. The error probabilities are found in Fig. 5.3, where they are plotted against the signal mean photon number $|\alpha|^2$. The Helstrom bound which is here the ultimate bound, is shown as a continuous black line. It can be seen that homodyne detection (green) performs better than Kennedy (blue) for $|\alpha|^2 \lesssim 0.4$ and this situation is reversed for higher $|\alpha|^2$. The optimized displacement detector error (red) outperforms the previous two: $P_{err}^{OD} < P_{err}^{HD}$ and $P_{err}^{OD} < P_{err}^{K}$ in the interval shown.

5.3 Discrimination of a QPSK alphabet via a hybrid receiver

5.3.1 Introduction

Previously in this chapter, the description of different types of receivers for the discrimination of binary alphabets was given. The main focus was in the case of binary phase shift keying (BPSK) applied to coherent states, which allowed to encode one classical bit per state, using the alphabet $A_{BPSK} = \{|\alpha\rangle, |-\alpha\rangle\}$. A lot of attention has already been devoted to the development of optimal and near-optimal discrimination strategies for this binary encoding [78, 79]. A more interesting situation and perhaps less studied in quantum communication, is when the alphabet is increased to 4 states as in the case of quadrature phase shift keying (QPSK). This type of encoding is more efficient, because the reception of one state gives directly 2 bits of information, effectively doubling the data rate.

QPSK is used for instance by the HSDPA protocol in UMTS networks for mobile phones [80] and in digital satellite communication. The QPSK alphabet comprises four states equally separated by a phase of $\pi/2$, $A_{QPSK} = \{|\alpha\rangle, |i\alpha\rangle, |-\alpha\rangle\, |-i\alpha\rangle\}$. The minimal error rates for the discrimination of the QPSK alphabet have been derived by Helstrom [31]. It has been shown that the feasible secret key rates of quantum key distribution systems can be largely improved by optimizing the receiver scheme [25, 26]. In particular, this has also been shown for the QPSK alphabet [54, 81–83], such that optimized QPSK receivers are very promising and of great interest for the quantum key distribution community.

In this section, we present two novel discrimination schemes. We use a hybrid approach which means that we consider both fundamental representations of our quantum states: the particle and the wave representation. We proof in theory that the standard scheme - heterodyne detection - can be outperformed for any signal amplitude and provide experimental evidence.

Let us discuss different discrimination strategies for the QPSK alphabet. Besides heterodyne detection, there are two other advanced discrimination schemes, based on a photon counting detector and feedback that were proposed by Bondurant [83]. In all these receivers, the measurement is performed by a single detection stage. In contrast, it is also possible to divide the state into parts which can be distributed among serveral detection stages. This method is for instance utilized in dual homodyne detection, where the received state is inferred by first splitting it on a balanced beam

splitter and subsequently measuring the projections along two orthogonal quadratures via two homodyne detectors. However, the retrieved information in a dual homodyne measurement and in a heterodyne detection is identical such that the error rate is not reduced by the additional detection stage.
Our strategy is to perform two successive measurements on parts of the quantum state, whereat the result of the first measurement reveals partial information about the state and is used to optimally tune the receiver for the second measurement. A schematic of the discrimination procedure is presented in Fig.5.4. The first measurement is performed by a homodyne detector and hence addresses the wave nature of the state. The homodyne measurement under a proper quadrature allows us to discard half of the possible states by making a binary decision based on the quadrature projections of the signal. The homodyne result is forwarded to a photon counting receiver, which finally identifies the input state by discriminating between the two remaining states. This task is performed near-optimally by an optimized displacement receiver [23, 84], which as we previously saw, is an advancement of the Kennedy receiver [52]. We implemented the hybrid scheme employing both the Kennedy receiver and the optimized displacement (OD) receiver. The comparison with the heterodyne scheme shows that the performance of the HD-Kennedy receiver beats the standard scheme for signal powers above a threshold (around $|\alpha|^2 \approx 1.6$). However the HD-OD receiver outperforms the Gaussian approach for any signal power.

5.3.2 Description and Theory

We are given a quadrature phase-shift keyed (QPSK) coherent alphabet $A = \{\hat{\rho}_1, \hat{\rho}_2, \hat{\rho}_3, \hat{\rho}_4\}$, with $\hat{\rho}_n = |\alpha_n\rangle\langle\alpha_n|$, where $\alpha_n = |\alpha|\, e^{i(n-\frac{1}{2})\frac{\pi}{2}}$, and having equal a priori probabilities $p_n = 1/4$. As before, the receiver, based on measurement outcomes, has to choose one of the n hypothesis H_n related to the reception of the state $\hat{\rho}_n$. The quantum limit - the Helstrom bound [31]- for the discrimination of these signals is asymptotically given by $P_{err}^{Hel} = \frac{1}{2}e^{-2|\alpha|^2}$ for $|\alpha|^2 \gg 1$. For simplicity, we will refer to the states in the alphabet directly by the corresponding ket $|\alpha_n\rangle$ since all $\hat{\rho}_n$ are pure states.
We will analyze two cases of a hybrid receiver:

HD+K: composed of Homodyne detection and kennedy receiver.
HD+OD: Homodyne detection and optimal displacement receiver.

Each of these hybrid receivers require the input signal to be divided and sent simultaneously to the individual binary receivers (HD and K or HD and OD). This splitting is done on an asymmetric beam splitter (ABS) with transmittance $T = t^2$

and reflectivity $R = r^2 = 1 - t^2$. First, one performs a homodyne detection along the $\hat{P}$ quadrature in phase space and makes a decision whether the signal is in the upper or the lower half plane. The result is forwarded to the other receiver, which is then tuned for the discrimination of the remaining pair of states, as shown in Fig.5.4.

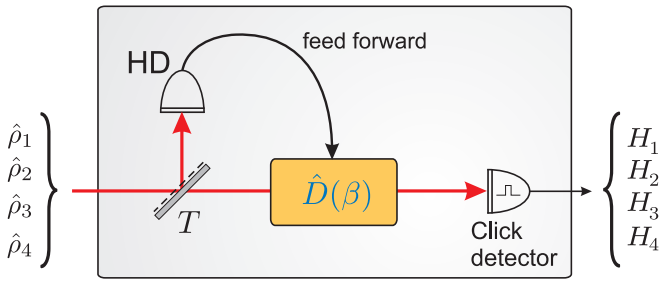

Figure 5.4: Schematic of the hybrid discrimination scheme. First a homodyne detector distinguishes between pairs of states. The result is forwarded to a click detector stage, which is tuned for the discrimination of the remaining binary state.

QPSK error probability for hybrid detectors

Let us recall the expression for the error probability in hypothesis testing (5.1):

$$P_{err} = \sum_{m \neq l} P(H_m|H_l)P(H_l)$$

In the case of 4 states, this expression contains 12 terms corresponding to detection errors expressed by conditional probabilities $P(H_m|H_l)$. In order to calculate P_{err}, it will be more convenient to first evaluate the individual success probabilities for the binary receivers[4] $P^{ind}_{succ}(m) = P(H_m|H_m)$ and then simply find[5]: $P_{err} = 1 - P^{hyb}_{succ}$, which has only 4 terms. In the case of the hybrid detectors analyzed here, the probability of success of the individual binary receivers is independent, and we can write:

$$P^{\mathrm{HD+K}}_{err} = 1 - \sum_m p_m P^{\mathrm{HD}}_{succ}(m) P^{\mathrm{K}}_{succ}(m) \tag{5.19}$$

$$P^{\mathrm{HD+OD}}_{err} = 1 - \sum_m p_m P^{\mathrm{HD}}_{succ}(m) P^{\mathrm{OD}}_{succ}(m) \tag{5.20}$$

Let us illustrate the procedure to calculate these probabilities in more detail, by assuming that the signal is prepared in the state $|\alpha_1\rangle$ as indicated in Fig.5.5. After

[4] ind=HD, K or OD
[5] hyb=HD+K or HD+OD

the splitting, the reflected part $|r\alpha_1\rangle$ is guided to the homodyne detector. The POVM elements for the homodyne detection along the $\hat{P}$ quadrature are:

$$\hat{\Pi}_0^{HD} = \int_0^\infty |p\rangle\langle p|\, dp,$$
$$\hat{\Pi}_1^{HD} = \mathbb{1} - \hat{\Pi}_0^{HD}, \tag{5.21}$$

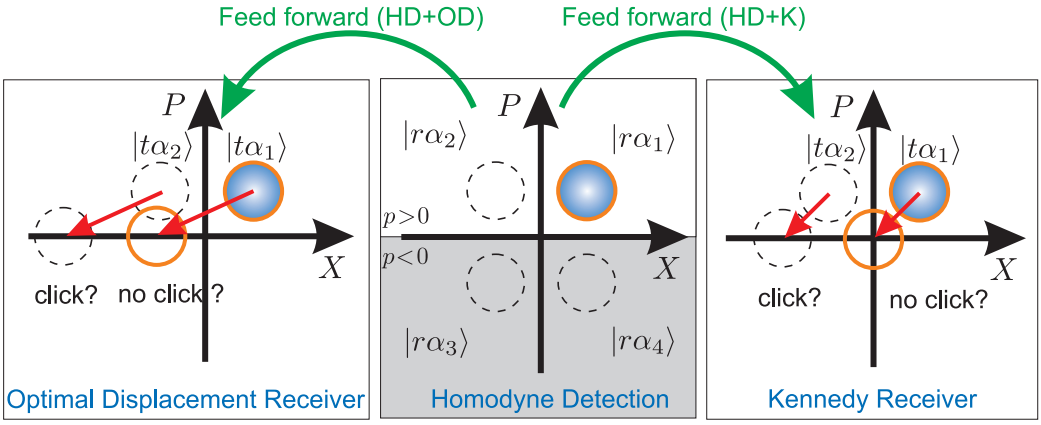

Figure 5.5: Illustration of the hybrid receivers in phase space. The HD projects the states onto the $\hat{P}$ quadrature and forwards the measurement outcome to the click detector stage. Based on the forwarded information, the displacement prior to the click detector is tuned for the discrimination of the remaining pair of states.

and the success probability to observe the outcome $p > 0$ when sending $|\alpha_1\rangle$ is then given by:

$$P_{succ}^{HD}(m=1) = \int_0^\infty |\langle p|r\alpha_1\rangle|^2\, dp = \frac{1}{2}\left(1 + \mathrm{erf}\sqrt{2}\frac{|r\alpha|}{\sqrt{2}}\right). \tag{5.22}$$

Note, that due to the projection onto the $\hat{P}$ quadrature, the effective signal amplitudes in the homodyne detection are reduced by a factor of $1/\sqrt{2}$. Assuming that the homodyne measurement was successful, the next task is to discriminate between $|t\alpha_1\rangle$ and $|t\alpha_2\rangle$ via the Kennedy or the optimal displacement receiver.

Homodyne-Kennedy receiver

The signal is displaced such that one of the remaining candidate states is shifted to the vacuum state $|0\rangle$, while the other state gets amplified to an amplitude of $|\sqrt{2}t\alpha|$. In the scenario depicted in Fig.5.5(center and right), the displacement was (arbitrarily) chosen to shift $|t\alpha_1\rangle$ to the vacuum. Therefore, the hypothesis is $|\alpha_1\rangle$, whenever no

click was detected, whereas the input state is identified as $|\alpha_2\rangle$ if a detection event is recognized in the click detector.

The corresponding POVM elements of the Kennedy receiver (diplacement+photon counting) are in this case:

$$\begin{aligned}\hat{\Pi}_0^K(\alpha) &= \hat{D}^\dagger(t\alpha_1)|0\rangle\langle 0|\hat{D}(t\alpha_1) = |-t\alpha_1\rangle\langle -t\alpha_1| \\ \hat{\Pi}_1^K(\alpha) &= \mathbb{1} - \hat{\Pi}_0^K(\alpha)\end{aligned} \tag{5.23}$$

As the vacuum state is an eigenstate of the photon number operator ($\hat{n} = \hat{a}^\dagger\hat{a}$), the state shifted to the vacuum state will never generate a click and the success probability $P_{succ}^K(1)$ is unit. The success probability $P_{succ}^{HD+K}(1)$ for correctly guessing $|\alpha_1\rangle$ is then given by

$$P_{succ}^{HD+K}(1) = \frac{1}{4}P_{succ}^K(1)\cdot P_{succ}^{HD}(1) = \frac{1}{4}P_{succ}^{HD}(1) \tag{5.24}$$

If instead the input signal was $|\alpha_2\rangle$, the success probability of the Kennedy receiver is $P_{succ}^K(2) = 1-e^{-2|t\alpha|^2}$, where the errors originate from the remaining overlap between the displaced state and the vacuum state. The total success rate for the detection of $|\alpha_2\rangle$ is given by

$$P_{succ}^{HD+K}(2) = \frac{1}{4}P_{succ}^K(2)\cdot P_{succ}^{HD}(2) = \frac{1}{4}\left(1-e^{-2|t\alpha|^2}\right)P_{succ}^{HD}(2) \tag{5.25}$$

Note, that the same error rates follow for the other signals ($n = 3, 4$). Consequently, the total error probability (5.19) for the HD+Kennedy hybrid receiver is

$$P_{err}^{HD+K} = 1 - \frac{1}{2}\left(P_{succ}^K(1)\cdot P_{succ}^{HD}(1) + P_{succ}^K(2)\cdot P_{succ}^{HD}(2)\right) \tag{5.26}$$

$$= 1 - \frac{1}{2}\left(1-\frac{1}{2}e^{-2|t\alpha|^2}\right)(1+\mathrm{erf}[|r\alpha|]) \tag{5.27}$$

Homodyne-Optimal Displacement receiver

The error rates for the HD+OD receiver follow directly by exchanging the Kennedy success rates $P_{succ}^K(1,2)$ for the success rates of the OD receiver. The optimal displacement parameter β for the QPSK signal can be derived by separating the displacement into two elementary steps as illustrated in Fig.5.9. First, the states are displaced to the quadrature. The situation is then equivalent to a binary state discrimination problem for two states with amplitude $\frac{|\alpha|}{\sqrt{2}}$.

The optimal displacement γ for these states is given by the solution of the transcendental equation:

$$\frac{t\alpha}{2} = \gamma\tanh\left(\sqrt{2}t\alpha\gamma\right) \tag{5.28}$$

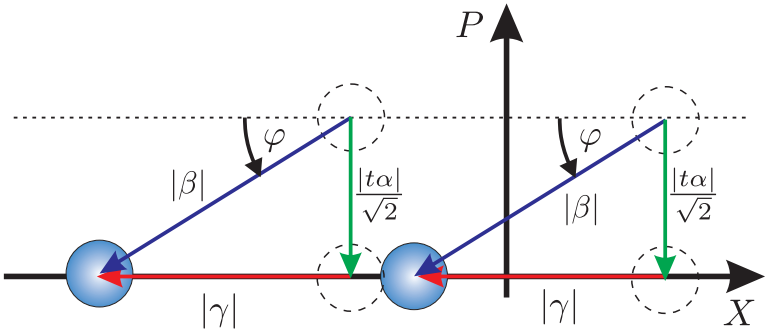

Figure 5.6: Sketch illustrating the two elementary displacement operation from which the optimal displacement for the QPSK alphabet is derived.

At the optimized displacement γ, the error rate is equal for both states and has the form:

$$P_{err}^{OD} = \frac{1}{2} - \exp\left(\frac{T|\alpha|^2}{2} + |\gamma|^2\right) \sinh\left(\frac{\sqrt{2}t\alpha\gamma}{2}\right). \tag{5.29}$$

The optimal displacement amplitude $|\beta|$ and phase φ for the QPSK signal are:

$$|\beta| = \sqrt{\frac{|t\alpha|^2}{2} + |\gamma|^2} \tag{5.30}$$

$$\varphi = \text{atan}\left(\frac{|t\alpha|^2}{\sqrt{2}|\gamma|}\right), \tag{5.31}$$

and the OD receiver is described by the POVMs:

$$\begin{aligned} \hat{\Pi}_0^{OD}(\beta) &= \hat{D}^\dagger(\beta)|0\rangle\langle 0|\hat{D}(\beta) = |-\beta\rangle\langle -\beta| \\ \hat{\Pi}_1^{OD}(\beta) &= \mathbb{1} - \hat{\Pi}_0^{OD}(\beta) \end{aligned} \tag{5.32}$$

The optimal displacement parameters for the Kennedy receiver and the OD receiver are shown as a function of the transmitted signal in Fig.5.7. The displacement in the OD receiver is clearly increased for small signal powers and has a minimum value of $|\beta|^2 = 0.5$ in the limit of very low signal powers. Asymptotically, the displacement of the OD receiver approaches the values of the Kennedy receiver, which is identical to the transmitted signal power. The phase φ describes the direction of the displacement in phase space as sketched in Fig.5.9. In case of bright signals, both detectors displace the states towards the vacuum state, which corresponds to a phase of $\varphi = \pi/4$. With decreasing signal power the phase in the OD receiver is asymptotically approaching $\varphi = 0$, which corresponds to a displacement parallel to the $\hat{X}$ quadrature.

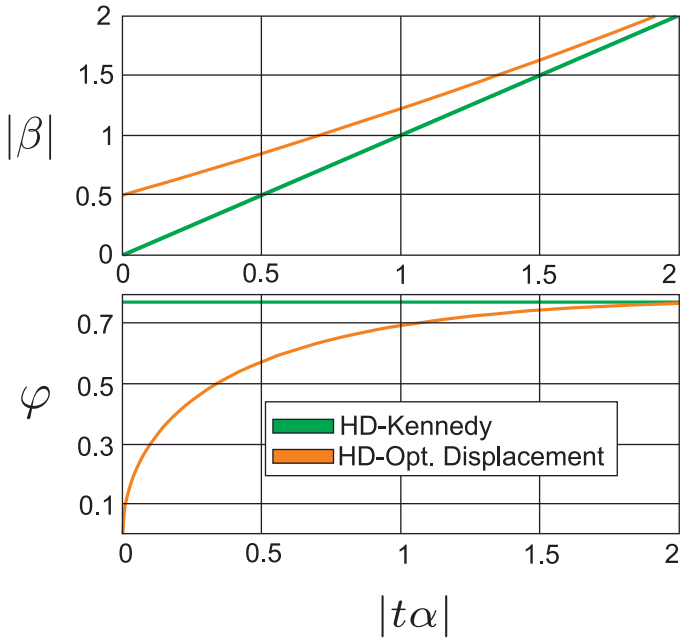

Figure 5.7: Optimal absolute values for the displacement $|\beta|^2$ and optimal displacement phases φ in dependence of the transmitted part of the signal $|t\alpha|^2$.

Besides of the displacement parameter β, the transmittance t^2 of the beam splitter can be optimized to minimize the error rate. The optimal parameters are shown in Fig.5.9. In case of small signal powers $|\alpha|^2 \approx 1$, the quantum state in the HD+OD receiver is distributed nearly equally among the two receiver stages $t^2 \approx 0.5$. With increasing signal power the share of the photon receiver is monotonically decreasing. In contrast, the optimized transmission for the HD+Kennedy receiver shows a distinct maximum around $|\alpha|^2 \approx 0.5$, but approaches the optimal transmission parameter of the HD-OD receiver asymptotically with increasing signal power. In the limit of very high signal powers $|\alpha|^2 \gg 1$ (not shown in the figure), the share of the photon receiver tends to $t^2 = 0$. This reflects the increasing imbalance between the performance in binary state discrimination of the photon receivers compared to HD detection [23]. In this regime, the photon counting receivers' performance is (in theory) exceedingly superior to the quadrature measurements, which thus constitutes the main source of errors. The total error is minimized by allocating the major share of the state to the HD detector. Practically however, the performance of click detectors in the high amplitude regime is limited by dark counts.

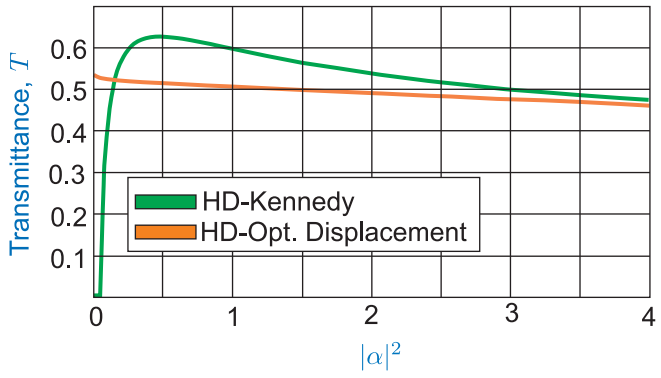

Figure 5.8: Optimal parameters for the transmittance to the photon detection stage in case of the Kennedy- and the optimized displacement receive

5.3.3 Experiment

We proceed with a description of the experimental setup, which is shown in Fig. 5.9. Our source is a grating-stabilized diode laser operating at a wavelength of 809 nm. The laser has a coherence time of 1 μs and is measured to be shot noise limited within the detected bandwidth. First, the beam passes a single mode fiber to purify the spatial mode profile. Subsequently, the beam is split asymmetrically into two parts: a bright local oscillator (LO), which is guided to the HD stage and an auxiliary oscillator (AO), which is used both to prepare the signal states and to realize the displacement at the photon receiver stage. Directly after the first beam splitter, the AO passes an attenuator (Att.) to reduce its intensity to the few photon level. The use of of electro-optical modulators (EOMs) and wave plates allows to generate signal states as pulses of 800 ns and at a repetition rate of 100 kHz in the same spatial mode as the AO but with an orthogonal polarization.

The signal is split on a beam splitter and the parts are guided to the homodyne detector HD and the photon receiver, respectively. In the HD path, the signal mode is separated from the AO via an optical isolator aligned to absorb the remaining AO. Moreover, the isolator avoids back-propagation of photons from the LO to the photon counting receiver. Subsequently, the signal is spatially superposed with the LO on a polarizing beam splitter (PBS). Up to this point signal and LO are still residing in orthogonal polarization modes. The required interference is achieved by a combination of a HWP and a PBS. The wave plate is aligned to rotate the polarization axis by an angle of $\pi/4$. At this point, the signal and the LO have equal support on the principal axis of the subsequent PBS, such that they are split symmetrically and the interference is achieved. The measured quadrature in the HD is adjusted via a

feed back controlled piezo-electric transducer in the LO path. The measured visibility between the signal and the LO is $V = 95\%$ and the quantum eficiency of the photo diodes is measured to be $\eta_{diodes} = 92 \pm 3\%$. From this, the total quantum eficiency of the homodyne detection follows as $\eta_{HD} = V^2 \cdot \eta_{diodes} = 83 \pm 3\%$.

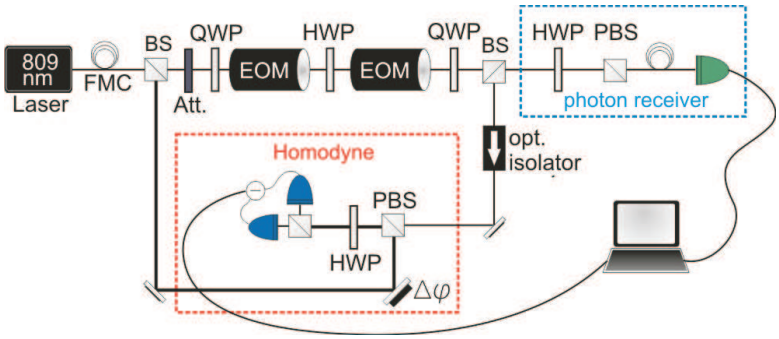

Figure 5.9: Experimental setup for the discrimination of the QPSK coherent states.

In the photon receiver path the displacement is generated by coupling photons from the AO to the signal mode. This is achieved by first rotating the polarization of the signal and the AO via a HWP, followed by a projection onto the original signal polarization mode by a PBS. The angle of the HWP, and hence the displacement strength, is controlled by a stepper motor. If the required rotation angle θ is small, i.e. for a suficiently bright AO, the disturbance of the signal states is small and the operation is equivalent to a perfect displacement operation. The displacement operation can be described as

$$|\alpha\rangle|AO\rangle \xrightarrow{HWP} |\alpha\cos\theta + AO\sin\theta\rangle|AO'\rangle \xrightarrow{\cos\theta\approx 1} |\alpha+\beta\rangle|AO'\rangle \tag{5.33}$$

where $|AO\rangle$ denotes the coherent state in the auxiliary oscillator mode. Experimentally however, increasing the AO power results in an increased dark count rate originating from the limited extinction ratio of the EOMs, which is measured to be $C \approx 1/500$. We therefore adjusted the mean photon number in the AO to optimize the trade off between state disturbance and dark count rate, which leads to an AO with about 20 photons. Finally, the displaced signal is coupled to a multi-mode fiber connected to an avalanche photo diode (APD). The APD is operated in an actively gated mode and has a measured quantum eficiency of $\eta_{\mathrm{APD}} = 63 \pm 3\%$.

We probe the receiver with a sequence of test signals. Each sequence is composed of an initial block of phase calibration pulses used to lock the quadrature in the homodyne measurement, followed by 9 blocks of probe pulses. Each block contains

the full QPSK alphabet for 34 different amplitudes in the range $|\alpha|^2 \in [0, 1.8]$. The stepper motor controlling the displacement is actuated after every 4000 runs of the sequence to vary the displacement $|\beta|^2$. The results of the individual measurements are sent to a computer and saved. The feed forward is emulated in the post-processing, where only the data in which the adjusted displacement concurred with the result of the HD measurement is evaluated. A limitation in performing the displacement by means of a HWP is that the direction of the displacement is restricted along one specific quadrature, depending on the relative phase ϕ of the AO with respect to the signal mode. However, in order to fulfill the optimality criterion in the HD+OD receiver, the direction of the displacement has to be adjusted depending on the signal amplitude (see eq. (5.31) and Fig.5.7). To account for this requirement, the signals in the probe blocks are generated with an equidistantly varying relative phase to the AO in the range $\phi \in [0, \pi/4]$.

The aim of the experiment is to provide a proof-of-principle demonstration of the hybrid receivers' performance unaffected by any imperfections of the implemented hardware, but only limited by the physical concept. In the analysis of the experimental data, we therefore assume unit quantum eficiencies for the individual receivers. Losses and detection ineficiencies, which can also straightforwardly be described as loss, merely result in a linear rescaling of the states' amplitudes. By combining this with the linearity of a beam splitter interaction, we can assign the detection ineficiencies to the state generation stage. This trick has proven to ease the understanding of the protocol by removing unnecessary prefactors. The assignment leads to a beam splitter with an effective splitting ratio: $T \to T' = \eta_{\mathrm{APD}} T/(\eta_{\mathrm{APD}} T + \eta_{\mathrm{HD}} R)$ and $R \to R' = \eta_{\mathrm{HD}} R/(\eta_{\mathrm{APD}} T + \eta_{\mathrm{HD}} R)$.

5.3.4 Experimental Results

We measured the error rates for both the HD-Kennedy receiver and the HD-OD receiver at an effective splitting ratio of $T/R = 53/47$. The results are compared to the performance of an ideal heterodyne receiver in Fig. 5.10a. The solid curves correspond to the theoretical error rates under ideal conditions, whereas the dashed curves include the detrimental effects of dark counts, which occurred with the probability of $2,72\%$. The error bars were derived by error propagation of the experimental uncertainties in the input amplitude $\Delta|\alpha| = 0.01$ and the displacement amplitude $\Delta|\beta| = 0.039$ as well as the fluctuations among repeated realizations of the experiment which were around 0.5%.

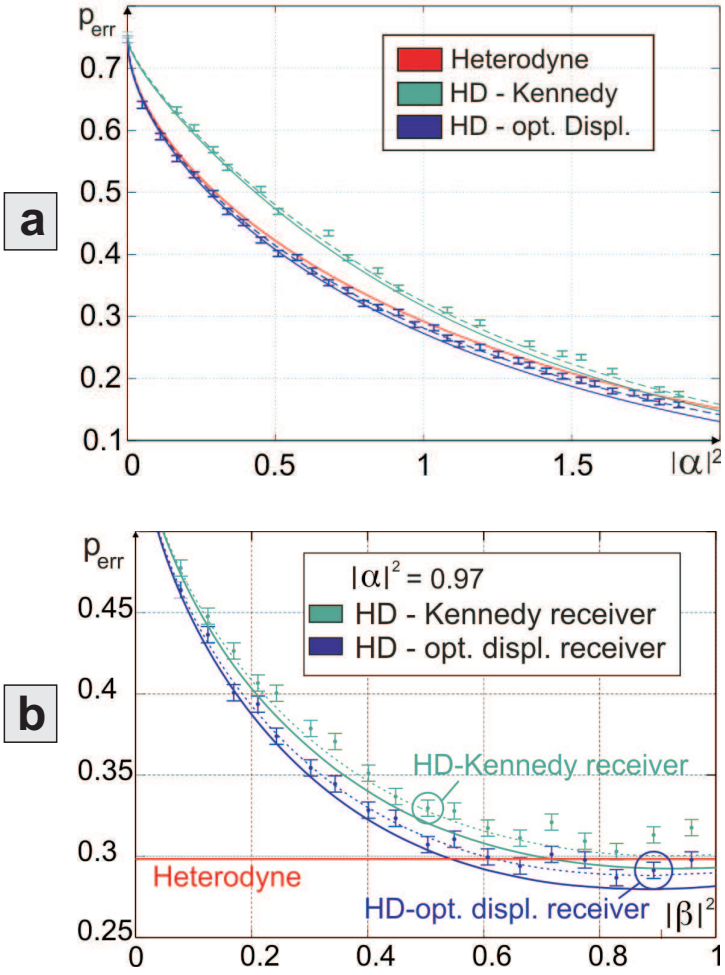

Figure 5.10: **a.** Experimental results for the error rates of the hybrid receivers compared to a perfect homodyne detector. The dashed lines correspond to the theoretical prediction including the detrimental effects of dark counts. **b.** Dependence of the hybrid receivers' error rates on the displacement amplitude for a input state with $|\alpha|^2$=0.97. The curves differ in the direction of the displacement in phase space.

We find the error rates for the HD+Kennedy receiver by evaluating the data where the signal power of the displaced state $|\alpha - \beta|^2$ is minimal, i.e. when one state has been displaced to the vacuum. The error rates for the HD+OD receiver are derived by minimizing the error rate over the range of measured displacements $|\beta|^2$ and displacement phases φ. The results for both receivers are in good agreement with the theoretical predictions. The measured error rates for the HD-OD receiver are below the corresponding error rate of the ideal heterodyne detector for any input amplitude. Moreover, most of the measurements beat the heterodyne receiver's performance with a significance of more than one standard deviation.

The essential difference between the HD+Kennedy and the HD+OD receiver is illustrated in Fig. 5.10b., where the dependence of the error rates over the displacement is shown for an input signal with mean photon number $|\alpha|^2 = 0.97$. The curves differ in the respective displacement angles in the two receivers. While the HD+Kennedy receiver was measured at $\varphi = \pi/4$, the phase in the HD+OD receiver was adjusted to fulfill the optimality criterion $\varphi = 0.62$. The configurations for the HD+Kennedy ($|\alpha|^2 = |\beta|^2$) and the HD+OD receiver (minimal error rate) are highlighted. Obviously, the performance of the HD+Kennedy receiver can already be enhanced by increasing the displacement amplitude $|\beta|^2$, however the minimal error rates are only achieved if both the displacement amplitude and phase are optimized. The corresponding error rate for the standard heterodyne receiver is shown as a reference and is surpassed by the HD+OD receiver for a wide range of displacement amplitudes. The curvature of the error rate around the minimum is remarkably flat, such that the dependence on the absolute amplitude of the displacement $|\beta|^2$ is low.

The relative error rates $\tilde{p}_{err}$ of the hybrid receivers, normalized to the error rates of heterodyne detection are shown Fig.5.11. Additionally, the relative error rates of the before mentioned Bondurant receiver [83] is shown. Bondurant had proposed two similar discrimination schemes which he termed type I and type II, respectively. The curve shown in the figure correponds to the Bondurant reveiver of type I, which provides the better performance in the considered region. While this receiver outperforms heterodyne detection and also our hybrid approaches for conventional signal amplitudes, it can not provide an enhanced performance in the domain of highly attenuated signals. The HD+OD receiver provides to the best of our knowledge the hitherto minimal error rates for signals with mean photon numbers $|\alpha|^2 \leq 0.75$.

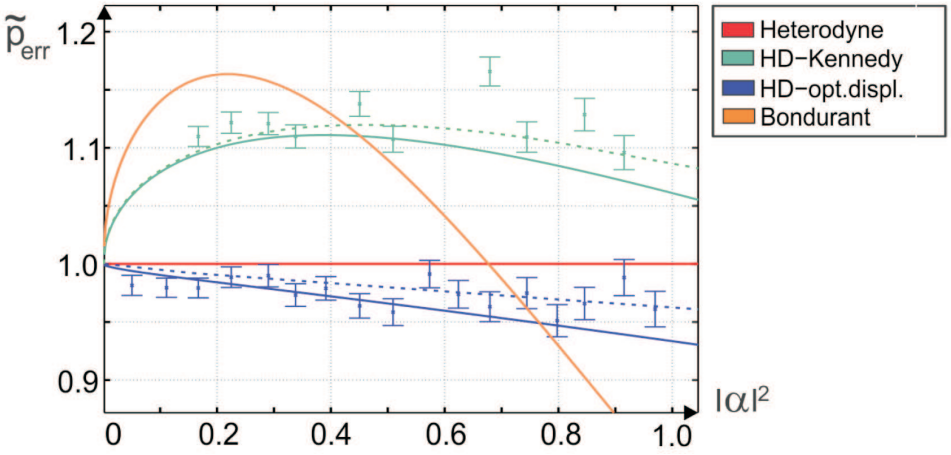

Figure 5.11: Comparison of the error rates from different receivers normalized to the standard scheme - heterodyne detection. Solid lines correspond to the error rates under ideal conditions, while the dashed lines include the detrimental effects of dark counts.

5.3.5 Conclusion.

We have proposed and experimentally realized a hybrid quantum receiver for the discrimination of QPSK coherent signals. We showed experimentally, that our novel receiver can outperform the standard scheme - heterodyne detection - for any signal amplitude.

Chapter 6

Conclusions

Here we briefly summarize the main conclusions of the thesis. We presented 3 main results:

1. We have presented a probabilistic noiseless amplifier, capable of reducing the phase variance of coherent states without the need for nonclassical resources or strong parametric interactions, requiring only Gaussian noise addition and photon counting. **Area:** quantum communication and quantum metrology.

2. We proposed and experimentally tested a hybrid quantum receiver for the discrimination of QPSK coherent signals. We showed experimentally, that our novel receiver can outperform the standard scheme - heterodyne detection - for any signal amplitude. **Area:** quantum communication.

3. We started the study of adaptive feedback in quantum optics and showed experimentally the basic components of the most complicated version of phase estimation: adaptive single shot ab initio phase estimation. We obtained very promising results that open interesting perspectives on this field. The theory presented as well as the experimental elements at disposition, can account for most (if not all) of the phase estimation protocols: single shot/repeated measurements, adaptive/nonadaptive, ab initio/phase sensing and other combinations. **Area:** quantum communication and quantum metrology.

We expect the first two results to have an immediate impact in the field of quantum information, while the third opens a new field of study in our labs, adaptive measurement, whose impact will be seen in the near future.

Bibliography

[1] Louisell, W.H. et al. Quantum Fluctuations and Noise in Parametric Processes. I. *Phys. Rev.* **124**, 1646 (1961).

[2] Holevo, A. S. *Springer Lecture Notes Math.* **1055**, 153 (1984).

[3] Haus, H.A. and Mullen, J.A. Quantum noise in linear amplifiers. *Phys. Rev.* **128**, 5 (1962).

[4] Caves, C.M. Quantum limits on the noise in linear amplifiers. *Phys. Rev. D* **26**, 8 (1982).

[5] Ou, Z. Y., Pereira, S. F. and Kimble, H. J. Quantum noise reduction in optical amplification. *Phys. Rev. Lett.* **70**, 3239 (1993).

[6] Josse, V., Sabuncu, M., Cerf, N., Leuchs, G. and Andersen U. L. Universal optical amplification without nonlinearity. *Phys. Rev. Lett.* **96** , 163602 (2006). .

[7] Ralph, T.C. and Lund, A.B. Nondeterministic noiseless linear amplification of quantum systems. *Quantum Communication Measurement and Computing Proceedings of 9th International Conference.* Ed. Lvovsky, A, 155–160, (AIP, New York 2009). *arXiv:* **0809.0326**[quant-ph], (2008).

[8] Xiang, G. Y., Ralph, T. C., Lund, A. P., Walk, N. and Pryde, G. J. Heralded noiseless linear amplification and distillation of entanglement. *Nature Photonics.* **4**, 316–319 (2010).

[9] Ferreyrol, F. et al. Implementation of a Nondeterministic Optical Noiseless Amplifier. *Physical Review Letters.* **104**, 26–29 (2010).

[10] Marek, P. and Filip, R. Coherent-state phase concentration by quantum probabilistic amplification. *Phys. Rev. A* **81**, 022302 (2010).

[11] Dirac, P. A. M. *The Quantum Theory of the Emission* and Absorption of Radiation. *Proc. R. Soc. Lond.* **A114**, 243 (1927).

[12] Shapiro, J.H., Shepard, S.R. and Wong, N.C. Ultimate quantum limits on phase measurement. *Phys. Rev. Lett.* **62**, 2377–2380 (1989).

[13] Fiurášek, J. Engineering quantum operations on traveling light beams by multiple photon addition and subtraction. *Phys. Rev. A* **80**, 053822 (2009).

[14] Menzies, D. and Croke, S. Noiseless linear amplification via weak measurements. *arXiv:* **0903.4181v1** [quant-ph], (2009).

[15] Ourjoumtsev, A. , Tualle-Brouri, R., Laurat, J., and Grangier, P. Generating Optical Schrdinger Kittens for Quantum Information Processing *Science* **312**, 83–86 (2006).

[16] Neergaard-Nielsen, J. S., Melholt Nielsen, B., Hettich, C., Mølmer, K., and Polzik, E. S. Generation of a Superposition of Odd Photon Number States for Quantum Information Networks *Phys. Rev. Lett.* , (2006).

[17] Takahashi, H., Wakui, K., Suzuki, S., Takeoka, M., Hayasaka, K., Furusawa, A., and Sasaki, M. Generation of Large-Amplitude Coherent-State Superposition via Ancilla-Assisted Photon Subtraction *Phys. Rev. Lett.* **101**, 233605 (2008).

[18] Wiseman, H. and Kilip, R.B. Adaptive single-shot phase measurements: The full quantum theory *Phys. Rev. A* **57**, 2169 (1998).

[19] Wiseman, H. M., & Killip, R. B. Adaptive single-shot phase measurements: A semiclassical approach. *Physical Review A.* **56(1)**, 944–957 (1997).

[20] Armen, M.A. et al. Adaptive Homodyne Measurement of Optical Phase. *Phys. Rev. Lett.* **89**, 133602 (2002).

[21] Lvovsky, A.I. Iterative maximum-likelihood reconstruction in quantum homodyne tomography. *J. Opt. B: Quantum Semiclass. Opt.* **6**, 556559 (2004).

[22] Hradil, Z. Quantum-state estimation. *Phys. Rev. A* **6**, R1561-R1564 (1997).

[23] Wittmann, C. et al. Demonstration of near-optimal discrimination of optical coherent states. *Phys. Rev. Lett.* **101**, 210501 (2008).

[24] Banaszek, K. et al. Direct measurement of the Wigner function by photon counting. *Phys. Rev. A* **60**, 674-677 (1999).

[25] Wittmann, C., Andersen, U.L., Takeoka, M., Sych, D. & Leuchs, G. Demonstration of coherent-state discrimination using a displacement-controlled photon-number-resolving detector. *Phys. Rev. Lett.* **104**, 100505 (2010).

[26] C Wittmann, U L Andersen, M Takeoka, D Sych and G Leuchs, Discrimination of binary coherent states using a homodyne detector and a photon number resolving detector Phys. Rev. A, 2010 **81**, 062338

[27] Holevo, A. S. Covariant measurements and imprimitivity systems. *Lect. Notes in Math.* **1055**, 153-172 (1982).

[28] Zavatta, A., Fiurášek, J., & Bellini, M. A high-fidelity noiseless amplifier for quantum light states. *Nature Photonics.* **5**, 52-60 (2010). doi:10.1038/nphoton.2010.260

[29] Pegg, D.T., Phillips, L.S. & Barnett, S.M. Optical State Truncation by Projection Synthesis. *Physical Review Letters.* **81**, 1604-1606 (1998).

[30] Babichev, S.A., Ries, J. & Lvovsky, A.I. Quantum scissors: teleportation of single-mode optical states by means of a nonlocal single photon. *Europhysics Letters.* **64**, 1–7 (2002).

[31] Helstrom, C.W. Quantum detection and estimation theory. *(Academic Press, New York, 1967)*

[32] Wootters, W.K. & Zurek, W.H. A single quantum cannot be cloned. *Nature.* **299**, 802–803 (1982).

[33] Parigi, V., Zavatta, A., Kim, M.S., & Bellini, M. Probing quantum commutation rules by addition and subtraction of single photons to/from a light field. *Science* **317** , 1890–1893 (2007). doi:10.1126/science.1146204

[34] Edited by Rosenfeld, L.; Nielsen, J. Rud, eds., Niels Bohr, Collected Works, Volume 3, The Correspondence Principle (1918-1923), *(North-Holland, Amsterdam, 1976)* ISBN 0444107843

[35] J. Von Neumann, *Mathematical Foundations of Quantum Mechanics* (Princeton U. Press, 1983).

[36] A. Peres, Quantum Theory: Concepts and Methods (Kluwer, 1993).

[37] Andersen, U.L., Josse, V. & Leuchs, G. Unconditional quantum cloning of coherent states with linear optics. Physical Review Letters **94**, 1-4 (2005).

[38] S.J. Dolinar. Quarterly progress report. Technical Report 111, Research Laboratory of Electronics, MIT, 1973.

[39] Robert L. Cook, Paul J. Martin, and JM Geremia. Optical coherent state discrimination using a closed-loop quantum measurement. Nature, 446:774, April 2007.

[40] JM Geremia. Optimal discrimination of optical coherent states with imperfect detection. Phys. Rev. A, **70**, 062303, 2004.

[41] C. W. Gardiner and P. Zoller, Quantum Noise, 2nd ed. New York: Springer, 2000.

[42] C. W. Gardiner, Handbook of Stochastic Methods, 2nd ed. Springer, 2002.

[43] J. J. Sakurai. Modern Quantum Mechanics. Addison-Wesley, 1994.

[44] M. A. Nielsen and I. L. Chuang. Quantum computation and quantum information. Cambridge University Press (2000).

[45] R. J. Glauber, Coherent and incoherent states of the radiation field, Phys. Rev. **133**, 2766 (1963).

[46] R. J. Glauber, The quantum theory of optical coherence, Phys. Rev. **130**, 2529 (1963).

[47] U. Leonhardt, Measuring the quantum state of light (Cambridge university press, 1997).

[48] R. Loudon, The Quantum Theory of Light (Oxford Science Publication, 2000).

[49] M. A. Usuga, C. R. Mueller, C. Wittmann, P. Marek, R. Filip, C. Marquardt, G. Leuchs and U. L. Andersen. Noise-Powered Probabilistic Concentration of Phase Information. Nature Physics **6**, 767–771 (2010).

[50] C. H. Bennett and G. Brassard, in *Proceedings of IEEE Conference, Bangalore, India* (IEEE, New York, 1984), p. 175.

[51] Gisin, N. & Thew, R. Quantum Communication. Nature Photonics **1**, 165–171 (2007).

[52] Kennedy, Research Laboratory of Electronics, MIT Technical Report No. 110, 1972.

[53] C H Bennett, Quantum cryptography using any two nonorthogonal states Phys. Rev. Lett. **68**, 3121–3124,(1992)

[54] S Lorenz, N Korolkova and G Leuchs, Continuous-variable quantum key distribution using polarization encoding and post selection Appl. Phys. B, 2004 **79** (3), 273–277

[55] M Takeoka and M Sasaki, Discrimination of the binary coherent signal: Gaussian-operation limit and simple non-Gaussian near-optimal receivers Phys. Rev. A, 2008 **78**, 022320 (2008)

[56] H. Cramer, Mathematical methods of statistics, Princeton University Press (1946).

[57] S. Olivares and M.G.A. Paris. Bayesian estimation in homodyne interferometry. J. Phys. B 42, 055506 (2009)

[58] H. A. Bachor and T. C. Ralph, A Guide to Experiments in Quantum Optics (New York: WileyVCH Verlag GmbH & Co. KgaA, 2004).

[59] W. Schleich, Quantum optics in phase space (Wiley-VCH New York, 2001).

[60] R. E. Slusher, L. W. Hollberg, B. Yurke, J. C. Mertz, and J. F. Valley, Observation of squeezed states generated by four-wave mixing in an optical cavity, Physical Review Letters **55**, 2409 (1985).

[61] L. A. Wu, H. J. Kimble, J. L. Hall, and H. Wu, Generation of squeezed states by parametric down conversion, Physical Review Letters **57**, 2520 (1986).

[62] D. Stoler, Equivalence classes of minimum uncertainty packets Physical Review D **1**, 3217 (1970).

[63] H. P. Yuen, Two-photon coherent states of the radiation field, Physical Review A **13**, 2226 (1976).

[64] R. Boyd. Radiometry and the Detection of Optical Radiation. John Wiley and Sons, New York, 1983.

[65] R. Jozsa, Fidelity for mixed quantum states. J. Mod. Opt. **41**, 2315–2323, 1994

[66] S. M. Barnett and D. T. Pegg, J. Phys. A, **19** (1986), 3849.

[67] L. Susskind and J. Glogower, Physics **1** (1964) 49.

[68] L. Mandel and E. Wolf. *Optical coherence and quantum optics*. Cambridge University Press, Cambridge, 1995.

[69] J. D. Jackson. *Classical Electrodynamics*. John Wiley & Sons Inc. 3 edition 1998.

[70] Fox, M. *Quantum Optics, an Introduction*. Oxford University Press, 2006

[71] K. E. Cahill and R. J. Glauber. Density operators and quasiprobability distributions, Phys. Rev. **177** 1882 (1969).

[72] Wigner, E. On the Quantum Correction For Thermodynamic Equilibrium. Physical Review 40, 749-759 (1932).

[73] M. O. Scully and M. S. Zubairy. Quantum Optics. Cambridge University Press, 1997.

[74] D. Walls and G. Milburn. Quantum Optics. Spinger, 1995.

[75] S. Barnett and P. Radmore. Methods in Theoretical Quantum Optics. Oxford science publications, 2002.

[76] Hai-Woong Lee, *Theory and Application of the Quantum Phase-Space Distribution Functions*, Physics Reports **259**, 147 (1995) (doi: 10.1016/0370-1573(95)00007-4)

[77] Dorf, R.C. & Bishop, R.H. *Modern Control Systems*. (Prentice Hall: 2008).

[78] K Tsujino, D Fukuda, G Fujii, S Inoue, M Fujiwara, M Takeoka, and M Sasaki Sub-shot-noise-limit discrimination of on-off keyed coherent signals via a quantum receiver with a superconducting transition edge sensor, Opt. Express, 2010, **18**, 8107

[79] K Tsujino, D Fukuda, G Fujii, S Inoue, M Fujiwara, M Takeoka, and M Sasaki, Quantum receiver beyond the standard quantum limit of coherent optical communication Phys. Rev. Lett. , 2011 **106**, 250503

[80] H Holma and A Toskala, WCDMA for UMTS: HSPA Evolution and LTE John Wiley & Sons, 2007

[81] D Sych and G Leuchs, Coherent state quantum key distribution with multi letter phase-shift keying New. J. Phys., 2010 **12**, 053019

[82] A Leverrier and P Grangier, Unconditional Security Proof of Long-Distance Continuous-Variable Quantum Key Distribution with Discrete Modulation Phys. Rev. Lett., 2009 102, 180504

[83] R S Bondurant, Discrimination of the binary coherent signal: Gaussian-operation limit and simple non-Gaussian near-optimal receivers Opt. Lett., 1993 **18**, 22, 1896-1898

[84] M Takeoka and M Sasaki, Discrimination of the binary coherent signal: Gaussian-operation limit and simple non-Gaussian near-optimal receivers Phys. Rev. A, 2008 **78**, 022320

[85] Wiseman, H. Adaptive phase measurements of optical modes: Going beyond the marginal Q distribution. Physical review letters **75**, 4587-4590 (1995).

[86] R.C. Cofer and B. F. Harding, Rapid System Prototyping with FPGAs: Accelerating the design process (Embedded Technology). New York: Elsevier, 2006.

[87] Xilinx Virtex-5 FPGA Configuration User Guide. 2011.

Appendix 1: FPGA

- **FPGA board technical details:**

Xilinx FPGA XC5VSX95T-FF1136
SRIO(Serial Rapid I/O)
PICMIG AMC(Advanced Mezzanine Card) standard card edge (1 group)
PCI Express : x1 PCI Express cable interface
SMA Connector : High speed interface of 4-pare of each input/output
XGI Connector : XILINX ML402 VIODC (Video IO Daughter Card)
Use SAMTEC connector
DDR2 SDRAM : 2-group Micron DDR2 SDRAM (1group data 32bit, 128MB)
SRAM/Flash Memory : GSI technology SRAM and Intel Flash Memory
EIA-232C : Debug interface
GPIO : 2x 7-segment, 3x LED, 1x 8-pole DIP, 4x PUSH switch
Analog board:
Sub-board has 2 channel ADC/DAC
ADC : 14bit @max 155MSPS (National Semiconductor ADC14155)
DAC : 14bit @max 135MSPS (National Semiconductor DAC14135)

- FPGA specifications

Virtex-5 FPGA

Device	Configurable Logic Blocks (CLBs)			DSP48E Slices	Block RAM Blocks			CMTs	PowerPC Processor Blocks	Endpoint Blocks for PCI Express	Ethernet MACs	Max RocketIO Transceivers		Total I/O Banks	Max User I/O
	Array (Row x Col)	Virtex-5 Slices	Max Distributed RAM (Kb)		18 Kb	36 Kb	Max (Kb)					GTP	GTX		
XC5VSX95T	160 x 46	14,720	1,520	640	488	244	8,784	6	N/A	1	4	16	N/A	19	640

Figure 1: FPGAspecs.

- FPGA analog filter

Here is the transfer function of the analog card in the Paltek FPGA board. It was measured by using a signal generator and an oscilloscope that recorded both input and output signals. The FPGA here, does not perform any calculation apart from formatting the binary, and it was internally programmed to send the input directly to the output. The Amplitude shown is a relative amplitude normalized with respect to the input. It is clear that the phase in the plot has a contribution from the latency of the board that we have estimated to be around 100ns.

This spectrum has clearly the behavior of a High pass filter, which became obvious when I checked the analog board and discovered a capacitor in series with the input and connected to a transformer. The cutoff frequency (3dB attenuation) is about 70KHz.

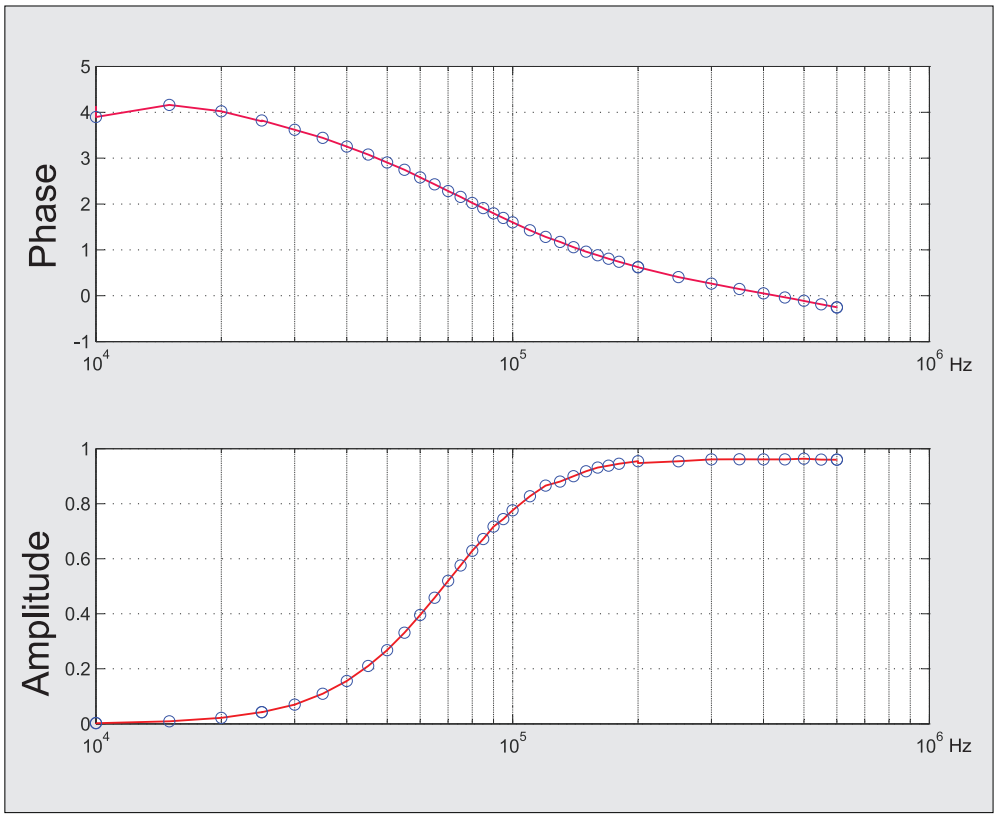

Figure 2: FPGAfilter. High pass filter in the input and output of FPGA

- Digital board

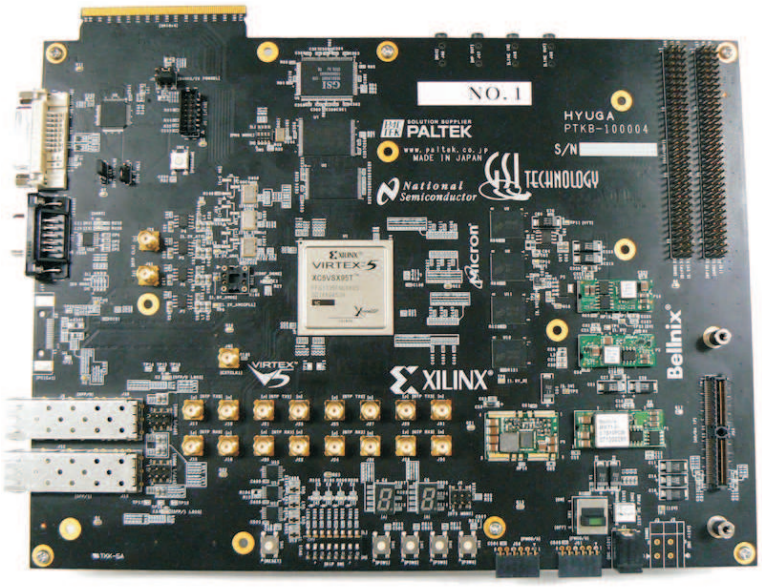

Figure 3: Digitalboard.

- Analog board

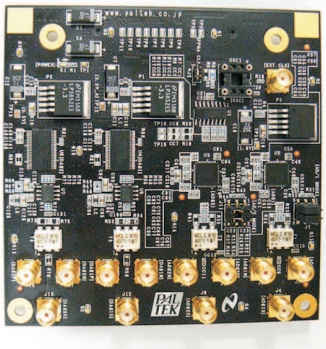

Figure 4: Analogboard.

- User Constraints File (UCF) for the Virtex 5 XC5VSX95T FPGA

```
##-----------------------------------------------
## Design Name    : AD_DA_95T_2012
## File Name      : AD_DA_95T_2012.ucf
## Author         : Mario A. Usuga
##-----------------------------------------------

NET "CLOCK" TNM_NET = CLOCK ;
TIMESPEC TS_CLOCK = PERIOD "CLOCK" 20 ns HIGH 50% ;
NET "CLOCK"  LOC = AG21  | IOSTANDARD = LVTTL ;  ##Sysclk



##  some outputs
NET "rst1"      LOC = AA8  | IOSTANDARD = LVTTL;  ## SW6
NET "rst2"      LOC = AB8  | IOSTANDARD = LVTTL;  ## SW7
NET "clk0"      LOC = D22;  ##| IOSTANDARD = LVCMOS25 OR LVTTL33;
NET "locked1"   LOC = G12  | IOSTANDARD = LVTTL;   ##E6
NET "locked2"   LOC = AD4  | IOSTANDARD = LVTTL;   ##E7


##  DAC_CH1_CLK

NET "DAC_CLK1_p" LOC = "H19" |IOSTANDARD = LVDS_25 ;
NET "DAC_CLK1_n" LOC = "H20" |IOSTANDARD = LVDS_25 ;

##  DAC_CH1

NET "data_out1<0>"  LOC = AK28 | IOSTANDARD = LVTTL;
NET "data_out1<1>"  LOC = AF24 | IOSTANDARD = LVTTL;
NET "data_out1<2>"  LOC = AK27 | IOSTANDARD = LVTTL;
NET "data_out1<3>"  LOC = AB26 | IOSTANDARD = LVTTL;
NET "data_out1<4>"  LOC = AK26 | IOSTANDARD = LVTTL;
NET "data_out1<5>"  LOC = AA28 | IOSTANDARD = LVTTL;
NET "data_out1<6>"  LOC = AJ26 | IOSTANDARD = LVTTL;
NET "data_out1<7>"  LOC = AH28 | IOSTANDARD = LVTTL;
NET "data_out1<8>"  LOC = AF25 | IOSTANDARD = LVTTL;
NET "data_out1<9>"  LOC = AG28 | IOSTANDARD = LVTTL;
NET "data_out1<10>" LOC = AG27 | IOSTANDARD = LVTTL;
NET "data_out1<11>" LOC = AE27 | IOSTANDARD = LVTTL;
NET "data_out1<12>" LOC = AH27 | IOSTANDARD = LVTTL;
NET "data_out1<13>" LOC = AB28 | IOSTANDARD = LVTTL;

##  DAC_CH2_CLK

NET "DAC_CLK2_p" LOC = "L19" |IOSTANDARD = LVDS_25 ;
NET "DAC_CLK2_n" LOC = "K19" |IOSTANDARD = LVDS_25 ;

##  DAC_CH2

NET "data_out2<0>"  LOC = AC25 | IOSTANDARD = LVTTL;
NET "data_out2<1>"  LOC = AC28 | IOSTANDARD = LVTTL;
NET "data_out2<2>"  LOC = AC24 | IOSTANDARD = LVTTL;
NET "data_out2<3>"  LOC = AC27 | IOSTANDARD = LVTTL;
NET "data_out2<4>"  LOC = AD25 | IOSTANDARD = LVTTL;
NET "data_out2<5>"  LOC = AE28 | IOSTANDARD = LVTTL;
NET "data_out2<6>"  LOC = AE24 | IOSTANDARD = LVTTL;
NET "data_out2<7>"  LOC = AF28 | IOSTANDARD = LVTTL;
NET "data_out2<8>"  LOC = AD24 | IOSTANDARD = LVTTL;
NET "data_out2<9>"  LOC = AD27 | IOSTANDARD = LVTTL;
NET "data_out2<10>" LOC = AG26 | IOSTANDARD = LVTTL;
NET "data_out2<11>" LOC = AD26 | IOSTANDARD = LVTTL;
```

```
62        NET "data_out2<12>" LOC = AB25 | IOSTANDARD = LVTTL;
63        NET "data_out2<13>" LOC = AE26 | IOSTANDARD = LVTTL;
64
65        ##  ADC_CH1
66        NET "AD_clkn"   LOC = "J21"  | IOSTANDARD = LVDS_25 ;
67        NET "AD_clkp"   LOC = "J20"  | IOSTANDARD = LVDS_25 ;
68        NET "sub_clk"   LOC = "AK29" | IOSTANDARD = LVTTL ;
69
70        NET "data_in1<0>"   LOC = "K27" | IOSTANDARD = LVCMOS18;
71        NET "data_in1<1>"   LOC = "H25" | IOSTANDARD = LVCMOS18;
72        NET "data_in1<2>"   LOC = "K28" | IOSTANDARD = LVCMOS18;
73        NET "data_in1<3>"   LOC = "H27" | IOSTANDARD = LVCMOS18;
74        NET "data_in1<4>"   LOC = "L28" | IOSTANDARD = LVCMOS18;
75        NET "data_in1<5>"   LOC = "G25" | IOSTANDARD = LVCMOS18;
76        NET "data_in1<6>"   LOC = "J27" | IOSTANDARD = LVCMOS18;
77        NET "data_in1<7>"   LOC = "J25" | IOSTANDARD = LVCMOS18;
78        NET "data_in1<8>"   LOC = "M28" | IOSTANDARD = LVCMOS18;
79        NET "data_in1<9>"   LOC = "G26" | IOSTANDARD = LVCMOS18;
80        NET "data_in1<10>"  LOC = "N28" | IOSTANDARD = LVCMOS18;
81        NET "data_in1<11>"  LOC = "F25" | IOSTANDARD = LVCMOS18;
82        NET "data_in1<12>"  LOC = "M26" | IOSTANDARD = LVCMOS18;
83        NET "data_in1<13>"  LOC = "F26" | IOSTANDARD = LVCMOS18;
84
85        ##  ADC_CH1 16 29
86
87        NET "data_in2<0>"   LOC = P27 | IOSTANDARD = LVCMOS18;
88        NET "data_in2<1>"   LOC = E27 | IOSTANDARD = LVCMOS18;
89        NET "data_in2<2>"   LOC = P26 | IOSTANDARD = LVCMOS18;
90        NET "data_in2<3>"   LOC = E28 | IOSTANDARD = LVCMOS18;
91        NET "data_in2<4>"   LOC = P25 | IOSTANDARD = LVCMOS18;
92        NET "data_in2<5>"   LOC = G27 | IOSTANDARD = LVCMOS18;
93        NET "data_in2<6>"   LOC = H28 | IOSTANDARD = LVCMOS18;
94        NET "data_in2<7>"   LOC = J26 | IOSTANDARD = LVCMOS18;
95        NET "data_in2<8>"   LOC = K26 | IOSTANDARD = LVCMOS18;
96        NET "data_in2<9>"   LOC = F28 | IOSTANDARD = LVCMOS18;
97        NET "data_in2<10>"  LOC = P24 | IOSTANDARD = LVCMOS18;
98        NET "data_in2<11>"  LOC = G28 | IOSTANDARD = LVCMOS18;
99        NET "data_in2<12>"  LOC = N24 | IOSTANDARD = LVCMOS18;
100       NET "data_in2<13>"  LOC = L25 | IOSTANDARD = LVCMOS18;
101
102       ## Timing
103
104       NET "Bgate"     LOC = "AG7" | IOSTANDARD = LVTTL;
105       NET "Sgate"     LOC = "AJ7" | IOSTANDARD = LVTTL;
```

Appendix 2: Wave guide modulator (WGM)

Table 1: WGM characteristics

Phase modulator PM1060	
Central wavelength:	1060 nm
Opt. bandwidth:	+/-60nm
Half wave voltage (@1 kHz):	app. 10 V
Insertion loss:	app. 4 dB
Modulation frequency:	up to 1 GHz (sinus)
Rise time 10/90:	app. 200 ps
Maximum optical input power:	200 mW cw
Fibers:	1 m PM-fiber at input and output
Fiber Connector	FC/APC-connectors
Polarization (output fiber):	$>$ 18 dB
Polarization (chip):	$>$ 30 dB
Electrical connection:	SMA(f) - connector

Appendix 3: Electronic schematics

Here are some of the electronic circuits specially built for this thesis.

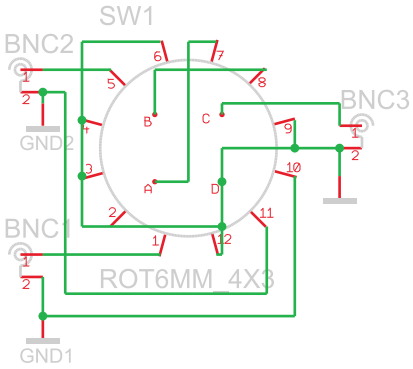

Figure 5: Isolation switch.

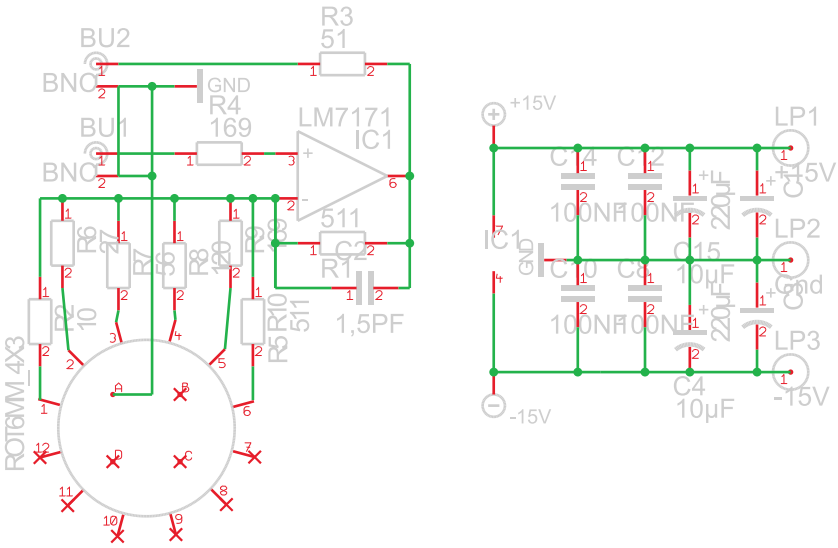

Figure 6: Variable gain fast amplifier.

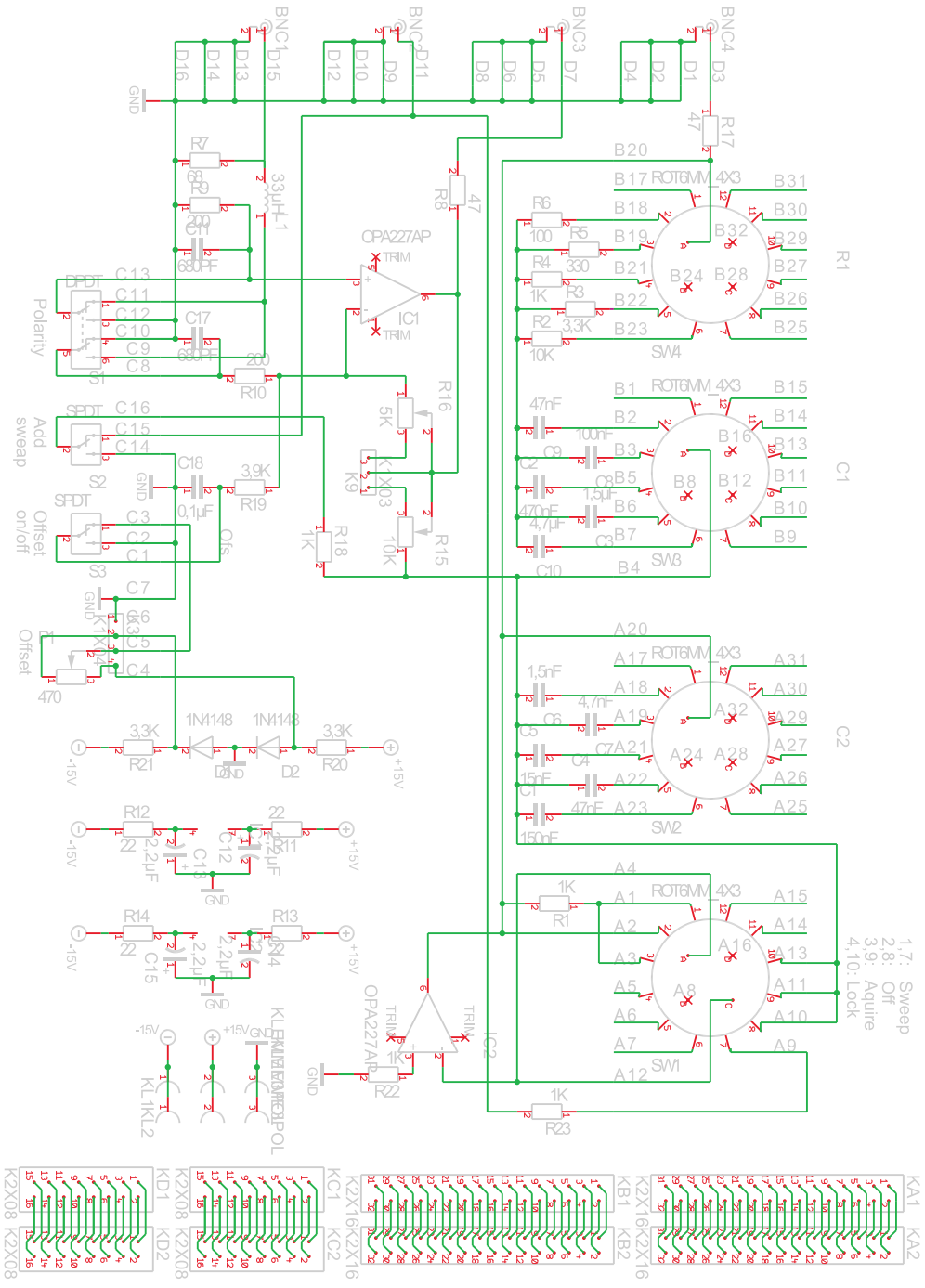

Figure 7: PID Controller.